Stony Brook University

DC Slice Ion Imaging Study of Atomic Orbital Orientation and Alignment in Photodissociation

A Dissertation Presented

by

Suk Kyoung Lee

to

The Graduate School

in Partial Fulfillment of the

Requirements

for the Degree of

Doctor of Philosophy

in

Chemistry

(Chemical Physics)

Stony Brook University

May 2007

Stony Brook University

The Graduate School

Suk Kyoung Lee

We, the dissertation committee for the above candidate for the

Doctor of Philosophy degree,

hereby recommend acceptance of this dissertation.

Arthur G. Suits - Disseration Advisor
Professor, Department of Chemistry

Philip M. Johnson - Chairperson of Defense
Professor, Department of Chemistry

Michelle Millar - Co-advisor and Third member
Professor, Department of Chemistry

James Muckerman - Outside member
Senior Scientist, Brookhaven National Laboratory

This dissertation is accepted by the Graduate School

Lawrence Martin
Dean of the Graduate School

Abstract of the Dissertation

DC Slice Ion Imaging Study of Atomic Orbital Orientation and Alignment in Photodissociation

by

Suk Kyoung Lee

Doctor of Philosophy

in

Chemistry

(Chemical Physics)

Stony Brook University

2007

Advisor: Arthur G. Suits

A complete study of atomic photofragment polarization has been achieved by using DC slice imaging, a recently developed approach directly providing the central slice of the full 3D product distribution without any mathematical transformation. In this dissertation, the quantum mechanical treatment adapted for the sliced images has been derived to extract the angular momentum polarization anisotropy parameters for any recoil speeds. The important photodissociation dynamics of small polyatomic molecules has been presented based on the thorough interpretation of the observed orientation and alignment.

The first demonstration of DC slice imaging of orbital polarization was a study of the 193 nm photodissociation of ethylene sulfide, followed by detailed investigation in ozone and OCS. In ozone, the speed-dependent orientation was measured for O($^1D_2$) atom produced from photodissociation in the $248 - 285$ nm region. The results show negligible orbital orientation following dissociation by circularly polarized light but strong recoil speed-dependent orientation following photolysis by linearly polarized light at all wavelengths studied. The origin of this polarization is ascribed to nonadiabatic transitions at avoided crossings and at long range.

The atomic orbital alignment and orientation, including the higher order moments ($K = 3, 4$), has been carried out for the photodissociation of OCS at 193 nm. The observed speed-dependent β and polarization parameters of S($^1D_2$) atom support the interpretation that there are two main dissociation processes: a simultaneous two-surface excitation and the initial single-surface excitation followed by the nonadiabatic crossing to the ground state. The angle- and speed-dependent density matrix can be constructed containing the higher order contributions for circularly-polarized dissociation light. It was shown in one case that the higher order contributions should not be overlooked for an accurate picture of the dissociation dynamics in this system.

In addition, photofragment angular anisotropy is reported for the photodissociation of acetaldehyde cations in the wavelength range $354 - 363$ nm. Three product channels were observed: HCO^+, CH_3CO^+ and CH_4^+. The distinct angular distribution of the CH_3CO^+ fragments shows a large value of the higher order Legendre polynomial term, providing evidence that acetaldehyde cations are spatially aligned during the ionization process.

For my beloved parents

Chang Soo Lee

and

Sook Ja Cho

Table of Contents

List of Figures

List of Tables

Acknowledgements

Finishing this dissertation, memories of experiences I have had over the past six years flashed across the mind. Without a great deal of kind help and wise advice provided by many people around me, I could not have achieved anything at all.

For training me to be who I am as a scientist, I want to give my foremost thanks to my advisor, Professor Arthur G. Suits. His passion for research has kept me inspired, and his confidence in my abilities has encouraged me not to give up whenever I have met any difficulty. I am especially grateful for his allowing me to have enough time to study the theory of angular momentum even though it took longer than predicted. I am also thankful that he was so patient with my weak English in the beginning. I'd certainly say that it has been great working with him, and I'm lucky to have had an advisor like Arthur.

The first meeting with Professor Oleg S. Vasyutinskii left a deep impression on me due to his profound theoretical understanding of angular momentum polarization. I have learned much from discussions with Oleg, who has directed my knowledge on the orbital polarization of photofragments to rise to a higher level.

I'd like to thank Professors Philip M. Johnson and Michelle Millar who have been giving a valuable guidance to me as the members of my committee. Phil's perceptive questions at every meeting always enlightened me about what a chemical physicist basically thinks and examines, and Michelle gave me comfort and confidence to do my best work.

Wen Li and Myung Hwa Kim were my closest fellow graduate students at Stony brook, and we moved together to Detroit following Arthur. Without them, life in Detroit might have been too boring and lonely. Wen is a kind of person showing his enthusiastic activities in the lab at every second. I will never forget our discussions about experimental results or even any trivial idea, which always rejuvenated the pure passion for science in my heart. Kim was one of the devoted graduate students in our group and, personally, was like a big brother to me during my graduate work. I deeply appreciate his kind concern about all matters and will miss our daily coffee breaks.

There are several talented post-docs whom I want to thank. The basic experimental skills I have are mostly learned from Dr. David Townsend at Stony Brook. With Dave's training and help, I could start my first ethylene sulfide experiment and finish the ozone project. I'd like to mention the initial help on the ethylene sulfide project of Michael P. Minitti, who was a graduate student and later moved to Brown University. While setting up the new lab in Detroit, Dr. Brian Leskiw taught me some practical skills to manage my machine by myself, and Dr. Steve Chambreau was willing to teach me the necessary mechanical techniques. For the last year of my graduate work, I shared lasers or chamber with Dr. Cunshun Huang, especially the 308 nm excimer laser which was always our common problem. Whenever I borrowed his laser, he helped me greatly to align it and make the long-distance beam pathway.

Half of my graduate work was accomplished at Wayne State University in Detroit. I have worked with Ruchira Silva to do these experiments, and specifically, he deserves credit for my acetaldehye work. Sridhar A. Lahankar and Lei Shen were colleagues who made my life at Wayne State University more enjoyable as skilled ping-pong partners playing with me every Friday. In addition, I'd like to thank all of my other group members for helping me whenever I needed their strength.

Diane Godden and Katherine Hughes, the capable staff members in chemistry department, deserve thanks for doing everything for me with kindness. Diane always suggested the fastest and most accurate way to fix any problems, and Katherine always thoughtfully considered my situation in Detroit, doing the ancillary but important tasks on my behalf. I'm also thankful to Sara Tipton, the instructor in the writing class I took last year, for diligent proofreading of this dissertation.

In the first year of graduate school at Stony Brook, I spent a great deal of time with my classmates, Young Chun and Jae-chul Lee. Sometimes, we, including Kim, studied overnight and helped each other with our course work. I still remember the wonderful taste of Dunkin Donuts' coffee we had to get rid of sleepiness around midnight. Besides friends in the chemistry department, there are many other Koreans who came to the U.S.A the same year and supported each other to overcome the tough life in a new place. Because of them, I enjoyed the life at Stony Brook and overcame homesickness which hit me like a wave from time to time. In particular, I want to give my thanks to Eugene Lee, who is studying in neuroscience. A long-lasting friendship with her is like the spring that can give me fresh spirit and strength.

Finally, I want to dedicate this dissertation to my parents, the most important people in my life. Their love and endless support always make me strong and optimistic. I am also grateful to my little brother and sister-in-law for taking care of my parents instead of me, which has enabled me to focus on what I want to do.

This thesis is based on the following publications:

- D. Townsend, S. K. Lee and A. G. Suits, "Orbital polarization from DC slice imaging: S($^1D_2$) alignment in the photodissociation of ethylene sulfide," *Chem. Phys.* **301**, 197 (2004)
- S. K. Lee, D. Townsend, O. S. Vasyutinskii and A. G. Suits,"O($^1D_2$) orbital orientation in the ultraviolet photodissociation of ozone," *Phys. Chem. Chem. Phys.* (Cover) **7**, 1650 (2005)
- S. K. Lee, R. Silva, S. Thamanna, O. S. Vasyutinskii and A. G. Suits, "S($^1D_2$) atomic orbital polarization in the photodissociation of OCS at 193 nm: construction of the complete density matrix," *J. Chem. Phys.*, **92**, 83002 (2006)
- S. K. Lee, R. Silva, M. H. Kim, L. Shen and A. G. Suits, " Photodissociation of spatially aligned acetaldehyde cations," *J. Phys. Chem. A*, (2007, *in press*)

Chapter 1

Introduction

Understanding elementary chemical reactions in as much detail as possible is the central goal of chemical dynamics. Many chemical processes which occur in nature are usually initiated by light, and, thus, photochemistry has great significance in such study, including a broad range of issues of fundamental importance in chemical physics: the theoretical description of chemical reactions, the quantum mechanical behavior of molecular systems, and the interaction of light with matter.[1] The key to elucidating photochemical processes is the characterization of the potential energy surface (PES) because the dynamic forces governing the breaking/forming of chemical bonds are closely related with PESs. The detailed information concerning the PESs can be provided by the study of the directions and anisotropies for vectors of interest, referred to as *dynamical stereochemistry.*[2]

Photodissociation is the central process in photochemistry. It has long been established that photofragments produced by dissociation with polarized light can themselves be polarized.[3] This polarization is also affected by the PESs on which dissociation evolves and is extensively explored by examining the correlation among vector quantities. Therefore, the study of photofragment polarization has been a valuable means of providing deep insight into the underlying dissociation dynamics. Investigations of vector properties in molecular photodissociation processes have been performed experimentally and theoretically during the past 40 years. Considerable effort has been devoted to elucidating the polarization of photofragments by introducing new experimental techniques with concomitant developments in theoretical treatments.

First, the general overview of vector correlations and relevant experimental methodologies will be addressed for the better understanding of the achievements discussed in this research. Specific vectors of interest are 1) $\boldsymbol{\mu}$, the transition dipole moment of a parent molecule, 2) $\mathbf{E}$, the polarization of the dissociation light, 3) $\mathbf{v}$, the photofragment recoil velocity, and 4) $\mathbf{J}$, the angular momentum of the photofragment. When light interacts with an isotropic gas sample, linearly polarized photolysis light will preferentially excite parent molecules with their transition dipole moment, $\boldsymbol{\mu}$, parallel to the polarization of the photolysis light, $\mathbf{E}$. This alignment between $\boldsymbol{\mu}$ and $\mathbf{E}$ is determined by the excitation probability, $|\boldsymbol{\mu}\cdot\mathbf{E}|^2$, in the electric dipole approximation. The laser polarization vector $\mathbf{E}$ is usually chosen as the laboratory-fixed Z axis. Consequently, $\boldsymbol{\mu}$ is aligned by the dissociation light defined in the laboratory frame, and subsequently, $\mathbf{v}$ and $\mathbf{J}$ can be also defined in the laboratory frame. The correlations between these vectors will be described in detail in the following sections.

1.1 E-μ-v Correlation: Recoil Velocity Anisotropy

Since Herschhach and Zare mentioned an anisotropic angular distribution of photofragments,[4] the most familiar vector correlation has been recoil velocity anisotropy ($\boldsymbol{\mu}$-**v** correlation), which can provide information on the symmetry and lifetime of the excited states involved in dissociation. The first experimental observation of photofragment velocity anisotropy was performed by Solomon,[5] and the theoretical description of this correlation was first provided by Zare.[6] The well-known expression is given as a function of the recoil angle,

$$I(\theta) = \frac{1}{4\pi}[1 + \beta\, P_2(\cos\theta)] \tag{1.1}$$

where θ is the angle between the photolysis polarization and the recoil direction, and $P_2(\cos\theta)$ is the second order Legendre polynomial.

The anisotropy parameter β can be presented as:

$$\beta = 2P_2(\cos\chi) \tag{1.2}$$

where χ is the angle between the transition dipole moment $\boldsymbol{\mu}$ and the asymptotic recoil direction $\mathbf{v}$. β ranges from -1 to 2 for linearly polarized light along the Z-axis and from 0.5 to -1 for circularly polarized light propagating the Z-axis.[7] For diatomic dissociation *via* the linearly polarized light, β values of -1 and 2 indicate that the photofragments recoil perpendicular or parallel to the transition moment, respectively. It should be noted that this theoretical treatment was constructed on the assumption that the characteristic dissociation time is significantly smaller than the molecular rotation period; this approximation is called the axial recoil limit. That is, the degree of $\boldsymbol{\mu}$-$\mathbf{v}$ correlation will be diminished during the dissociation process depending on the excited state lifetime. This breakdown of the axial recoil dynamics causes intermediate values of β. The recoil anisotropy of photofragments from rotating parent molecules has been both experimentally and theoretically investigated for diatomic and triatomic systems,[8–12] and recently, a quantum mechanical study of the non-axial recoil problem was explicitly reported for a diatomic-like system by Kuznetsov and Vasyutinskii.[13] Intermediate values also arise due to the bond breaking that is not strictly parallel or perpendicular to $\boldsymbol{\mu}$, such as in polyatomic systems.

1.2 E-$\boldsymbol{\mu}$-J Correlation: Angular Momentum Polarization

As in the case of velocity anisotropy, the $\boldsymbol{\mu}$-$\mathbf{J}$ correlation persists in the laboratory frame unless the alignment of $\boldsymbol{\mu}$ is lost owing to parent rotation prior to dissociation. After Van Brunt and Zare first discussed polarized fluorescence of photofragments in an electronically excited state,[3] studies of **E**-**J** correlation were mostly concerned with the rotational alignment of the photofragments.

The angular momentum distribution represents the expectation value of the angular momentum vector **J** along a given recoil direction, which is conveniently expanded in a series of multipole moments ρ_{KQ} of rank K and component Q. The zeroth order multipole moment corresponds to the population, while higher order odd moments (dipole octupole, *etc*) describe the angular momentum *orientation*, and

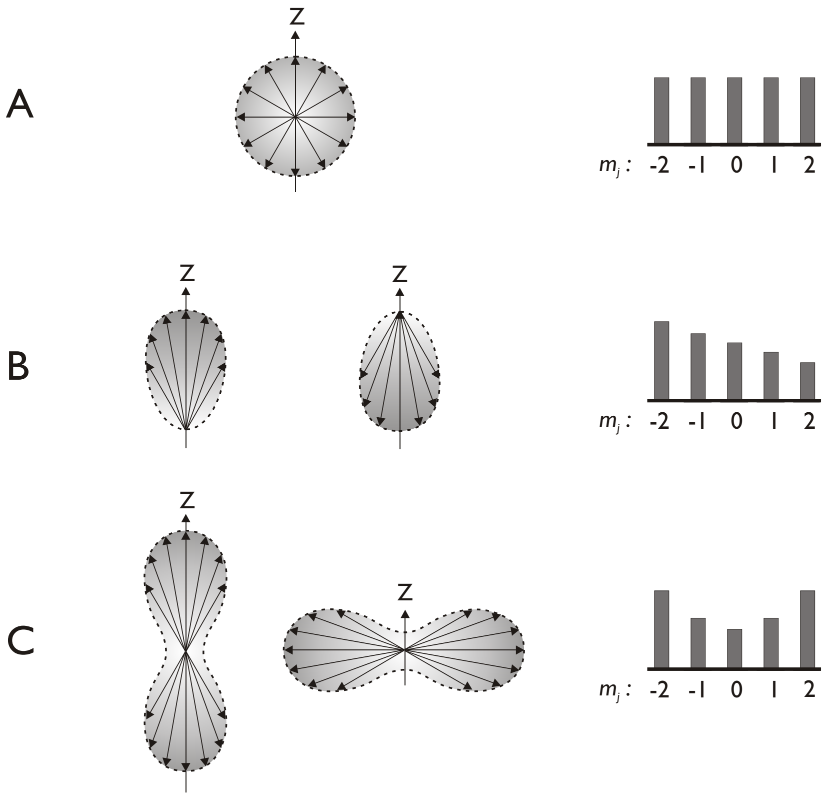

Figure 1.1: Schematic illustrations of (A) isotropic, (B) oriented, (C) aligned distributions of angular momentum vectors adapted from ref.[2] and corresponding the population of each magnetic sublevel, m_J.

even moments (quadrapole, hexadecapole, *etc*) describe the *alignment*. As shown in Fig. 1.1, orientation represents the unidirectional distribution (e.g, **J** preferentially points in one direction, e.g. up or down), and alignment is regarded as the bidirectional distribution (i.e., **J** preferentially points along a vertical axis rather than a horizontal axis or vice versa). These polarizations are directly reflected in nonequilibrium populations of the magnetic sublevels m_J, which are the projection of the total angular momentum **J** onto the recoil axis. Orientation, which may be probed only with circularly polarized light, is reflected in unequal populations changing with m_J, while alignment, probed with linearly or circularly polarized light, corresponds to unequal populations proportional to different $|m_J|$ levels. The diagonal elements (population) of the photofragment density matrix corresponding to each polarization effect are also schematically illustrated in Fig. 1.1.

In most early studies, the total alignment or orientation in the laboratory frame (**E**-**J** correlation) was mainly measured, which is the average polarization obtained by integrating over all recoil directions. However, these net measurements cannot give enough deep insight into the underlying dynamics, such as coherent effects and nonadiabatic processes. Such information can be provided by exploring the more detailed **v**-**J** correlation.

1.3 v-J Correlation

In contrast with velocity anisotropy and the net angular momentum polarization, the vector properties between **v** and **J** are completely independent of the laboratory frame and, thus, survive polarization scrambling due to a longer dissociation lifetime relative to rotation. As mentioned above, the recoil angle dependence of angular momentum polarization, the so-called "**v-J** vector correlation", can afford valuable insight into the dissociation event by revealing the dynamics in the molecular frame.[14] In other words, studies of this phenomenon tell us about the implications for the symmetries and potential surface shapes of the states involved and the role of coherence, nonadiabatic effects, and long-range interactions (see Fig. 1.2).[15–21]

The simplest way to understand this correlation is to consider two limiting cases, $\mathbf{v}\perp\mathbf{J}$ and $\mathbf{v}\|\mathbf{J}$. In the case of **v** perpendicular to **J**, the photofragments exhibit a

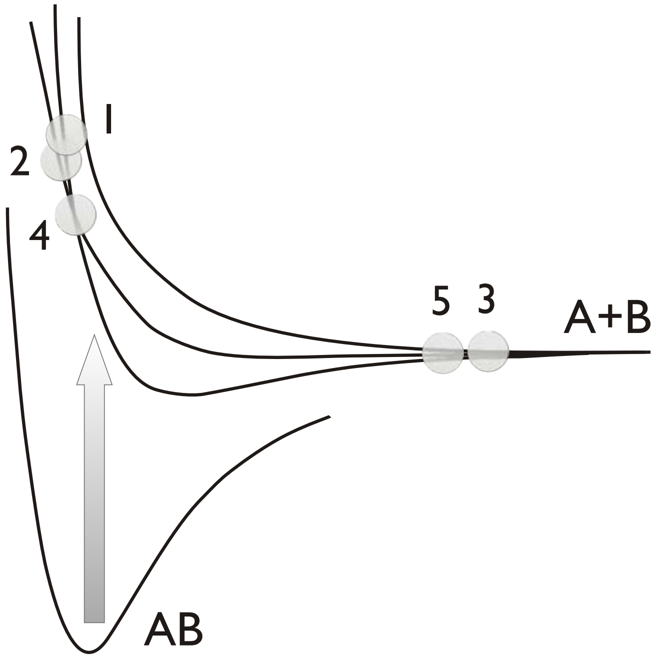

Figure 1.2: The factors which affect atomic angular momentum polarization: (1) Symmetry of excited electronic state, (2) Coherent excitation of multiple electronic states, (3) Coulomb interaction at large internuclear separation, (4) Nonadiabatic transitions at avoided crossings, and (5) Nonadiabatic transitions at large internuclear separation (adapted from ref.[22]).

"cart-wheel"-like motion (e.g., bent triatomic molecules). For the case of **v** parallel to **J**, the fragments execute a "propeller"-like motion (e.g., H_2O_2).[2] These limiting cases can be easily described by classical mechanics. However, **v** and **J** are not so strongly correlated in most chemical systems.

The development of the theory has been achieved to interpret the **v**-**J** correlation. The semiclassical approach by Dixon is based on the expansion of the angular distribution in terms of the expectation values of bipolar harmonics.[23] Although semiclassical models perfectly describe high-**J** rotational polarization, a quantum mechanical approach is best suited for treating the atomic angular momentum produced in dissociations with low **J**. Hall *et al.*[24] presented a density matrix approach. Siebbeles *et al.*[7] provided a fully quantum mechanical theoretical treatment, where the recoil angle dependence of angular momentum polarization is expressed in terms of scattering matrix elements. An important challenge is to make the explicit connection between theoretically defined parameters and practically observable measurements. Bracker *et al.*[17] presented a detailed quantum mechanical machinery in terms of anisotropy parameters introduced by Vasyutinskii and co-workers,[25] which is applicable to ion imaging experiments.

1.4 Experimental Approaches

The studies of vector correlation have employed a number of different experimental approaches. Velocity anisotropy is commonly measured by translational spectroscopy, in which the fragments are separated in space and then detected as a function of position and time. Another widely used method is the Doppler profile of photofragments noted by Zare and Herschbach.[4] In Doppler spectroscopy using a narrow-bandwidth laser, the width and shape of the Doppler profile provide information about the magnitude and anisotropy of velocity, respectively. For measuring the angular momentum polarization as well as velocity anisotropy, Doppler,[20,21,25,26] ion time-of-flight,[18,19,27] and ion imaging methods[15–17,28–46] have been used. In particular, the ion imaging technique has emerged as a premier means of investigating these phenomena owing to their ability to probe the nature of the angular momentum polarization as a function of the photofragment recoil angle. Therefore, this approach now dominates over alternative probe methods as the most convenient means of studying these phenomena. A significant recent advance in imaging probes of orbital polarization has been the development of slice imaging methods[47–49] that allow the angular momentum polarization to be measured directly over a large spread of photofragment recoil velocities, without needing to apply any form of forward convolution or inversion to the experimental data. The DC slice imaging technique is emerging as a very powerful tool for exploring atomic orbital polarization.

Atomic orbital polarization in photodissociation has been the subject of considerable interest since the late 1990s. Most studies to date have focused on rank $K = 2$ alignment (Cl_2,[17,40] NO_2,[31] N_2O,[32,34,39] BrCl,[37] O_3,[50] OCS,[51] HBr,[35,41] SO_2[42]) and rank $K = 1$ orientation(ICl,[27,52] Cl_2,[17] HCl,[38] O_3,[44] OCS,[33,45,51,53] BrCl[37]), ignoring the higher order moment contributions. However, the importance of the higher order $K = 3, 4$ terms is clear in some systems, such as O_3, even though a quantitative analysis has not yet been performed.[50,54] The theory has recently been extended to include the rank $K = 4$ case for photofragment alignment and applied to the experimental case of $O(^1D_2)$ atoms from N_2O photodissociation[55] and the rank $K = 3$ case for photofragment orientation applied to the experimental case of $Cl(^2P_{3/2})$ atoms from BrCl photodissociation.[46]

Although many recent studies have been performed to elucidate quantum dynamics especially for diatomic and triatomic photodissociation events, there still remain some phenomena not yet fully understood, and there has been little research on larger molecular systems. The DC slice imaging method, used as an experimental method in this research, could begin to accomplish such necessary tasks. Hence, it is essential to fully develop the theoretical machinery for DC slice imaging and demonstrate the application of this approach to the investigation of larger polyatomic dissociation dynamics (e.g., ethylene sulfide). The rigorous quantum mechanical treatment to deal with that system was developed based on the previous work of Siebbeles, Vanyutinskii and co-workers,[7,17,25] which will be described fully in Chapter 3. One of the strong points in the DC slice imaging approach, as mentioned before briefly, is the easy analysis of experimental data which enables one to obtain the recoil speed dependence of orbital polarization effects quite readily. Strong recoil speed-dependent alignment/orientation is closely associated with dynamics; For example, the ultraviolet photodissociation of ozone, the main topic of this research, showed an interesting correlation of the orientation effect with respect to the recoil speed which suggests the critical role of nonadiabatic transitions in the dissociation mechanism. In general, contributions of higher state multipoles are often neglected in most previous polarization studies, even though multipoles up to rank $K = 2J$ exist. Recently, a few groups have begun to emphasize the higher order contribution to photofragment polarization that enable one to completely exploit the physical properties happening in dissociation,[46,55] and the last part of this work will address this subject. This research also reports for the first time the full photofragment density matrix constructed by the complete polarization measurement including the higher order terms. The results presented in the following chapters open the possibility for the complete and comprehensive understanding of important chemical dynamics and achieve the extension of vector correlation study to complicated polyatomic systems.

This dissertation is organized as follows: Chapter 2 presents the background of the DC slice imaging experimental setup. Chapter 3 details the theoretical approach to extracting quantitative alignment and orientation data from slice imaging measurements. Chapter 4 shows the experimental ion images and measured polarization anisotropy parameters for ethylene sulfide, ozone and carbonyl sulfide photodissociation. Furthermore, the interpretation and discussion of experimental results are provided. Finally, the study of photofragment angular distribution is extended to a cation system in the Chapter 5, and the recoil angular anisotropy for acetaldehyde cation photodissociation has been investigated.

Chapter 2

Experimental Approach

2.1 Overview

Ion imaging has been a powerful and standard tool for studying photodissociation or reactive scattering since Chandler and Houston[56] first reported this technique in their paper on the photodissociation of methyl iodide. In comparison with the Doppler profile technique, it is a more straightforward method to measure product translational energy and angular distributions. The most substantial improvement of the ion imaging technique was achieved by Eppink and Parker[57] introducing the high resolution, velocity map imaging technique (VELMI). The energy resolution was improved by almost an order of magnitude higher than that which is obtainable with original ion imaging, typically 10 $\sim$ 20 %. In this technique, they removed the grids of the Wiley-McLaren setup and used inhomogeneous extraction field, by which the blurring of the image arising from the spatial distribution of the initial ion packet and the trajectory distortion induced by the grid are eliminated.

A general ion imaging setup is composed of a time-of-flight mass spectrometer combined with a two-dimensional (2D) position-sensitive detector, a microchannel plate (MCP) coupled to a fast phosphor screen and a charge coupled device (CCD) camera. A photofragment ion cloud flies toward the detector and is crushed into it, resulting in a raw 2D ion image. This 2D projection can be transformed using mathematical methods, such as the inverse Abel transformation, to reconstruct the full 3D photofragment distribution; then, the central section of interest is obtained. However, this inversion approach is always associated with artificial noise, especially along the cylindrical symmetry axis. Furthermore, the presence of the cylindrical symmetry axis parallel to the imaging plane is the prerequisite for adapting this method.[48] It causes a limitation on laser polarization geometries in two-color experiments. In particular, photolysis and probe beams with different polarizations are needed for the study of photofragment orientation and alignment. The specific experimental way to measure angular momentum polarization will be discussed in the next section, and its theoretical background will be addressed in Chapter 3 in detail.

A probe light source is usually utilized for the ionization of the neutral photofragments. A general one-photon ionization using tunable radiation may be achieved by synchrotron sources or vacuum ultraviolet (VUV) lasers. In this case, it is unlikely to detect the state-selected products since several quantum states are involved in this ionization, determined mostly by the Franck-Condon factors.[58] Multiphoton ionization, from a practical point of view, is more easily accessible by using frequency doubling/tripling of visible dye laser light. In addition, resonant multiphoton ionization provides a state-selective probe so that the advent of resonance enhanced multiphoton ionization (REMPI) has spurred the study of photodissociation dynamics. In N+M REMPI, N represents the number of photons required to reach the resonant excited intermediate state, and M describes the number of photons needed for ionization. Depending on a REMPI scheme, the image resolution can be impaired due to the recoil electron energy, when the excess energy above the ionization continuum is relatively large.

2.2 Measurement of Angular Momentum Polarization

Typically, the **v-J** correlation of photofragments is sensitive to spectroscopic probing such as REMPI, so that such polarization can induce additional angular modulations to the total signals. In effect, the angular momentum polarization information encoded in these modulations is extracted in terms of anisotropy parameters representing the distinct dissociation mechanisms. However, the contribution from the orbital polarization anisotropy to the total angular distribution is small relative to one from the population signal. Hence, it is better if the angular modulation attributed to the **v-J** correlation can be clearly isolated from the signal given by the population. The way to isolate these measurements is to perform a set of experiments with different geometries of photolysis and probe lasers. For instance, image data obtained with both vertically and horizontally polarized probe lasers should be collected in order to extract alignment effects. This usually results in a situation where the experimental image does not possess an axis of cylindrical symmetry, as mentioned previously.

According to the original methodology of Bracker *et al.*,[17] a series of basis images embodying the contribution from each of the possible dynamics were used to fit the experimental ‘orientation/alignment image’ that is the difference image between two images for different probe polarizations. The resulting fitted parameter for each basis function gives the relative contribution of each different excitation mechanism to the observed photofragment polarization, which can directly reveal the physical origins of the orbital polarization. In this so-called “forward-convolution” approach employing the basis functions, the symmetry requirement for the reconstruction process was no longer relevant. There have been successful applications of this approach to the photodissociation of several molecular systems for measuring both alignment and orientation.[14, 31, 32, 59] However, it is still not a perfect strategy for getting information on angular momentum polarization because this method is only suitable for situations where the photofragment kinetic energy distribution is monoenergetic in nature.

2.3 DC Slice Imaging

As one way to eliminate the cumbersome reconstruction, a slicing technique has been explored that may directly detect the central ‘slice’ of the 3D fragment distribution. The earliest idea for it was introduced by Tonokura and Suzuki,[60] in which they employed “laser sheet” ionization with a cylindrical focal lens to probe any slice of a neutral fragment sphere. A more recent development was reported by Kisopoulos and co-workers.[47] Applying a pulsed electric field to the expanded fragment ion following a short period of field free expansion results in a stretched ion clouds. The central section of the ion packet may be sampled exclusively with a narrow time gate at the imaging detector. A key advantage of slice imaging is that it allows the measurement of orbital polarization effects in a more direct way without the necessity for additional inversion methods, such as the inverse Abel transformation or complex forward convolution. In addition, it is adaptable to systems of interest which have a broad range of photofragment kinetic energy. Vector correlation studies in the photodissociation of Cl_2, Br_2, HCl, and HBr have been demonstrated with this method.[35,36]

This slice technique using delayed pulsed extraction, however, has a shortcoming associated with the grid that is used for creating the field-free region and the coupling into the recoil region. This leads to image blurring; therefore, the high resolution that is attainable with VELMI is compromised. This problem is circumvented by operating multilens velocity mapping ion optics at a low voltage, without a mesh grid (i.e., no pulsed field) .[48] In this *direct current* (DC) slice imaging developed by our group, the spread of an ion cloud is achieved by a low repeller voltage, and the momentum focusing is performed by regulating the voltage applied to extractor lenses. That is, the velocity resolution critically depends on the ratio of the applied voltage, given that other variables of the imaging apparatus are specific. Simulations for the expansion of a nascent isotropic distribution along the time-of-flight axis are presented in Fig. 2.1. A conventional velocity mapping condition is illustrated in Fig 2.1 A, where the entire ion cloud arrives at the detector within a short temporal spread (40 ns) and is detected. As mentioned above, the decrease of a repeller voltage gives rise to the expansion of the ion cloud, as presented in Fig 2.1 B. The extent of reducing V_R is limited by the loss of velocity focusing, which can be overcome by the use of additional electrodes. Fig 2.1 C represents such a case that two focusing lenses

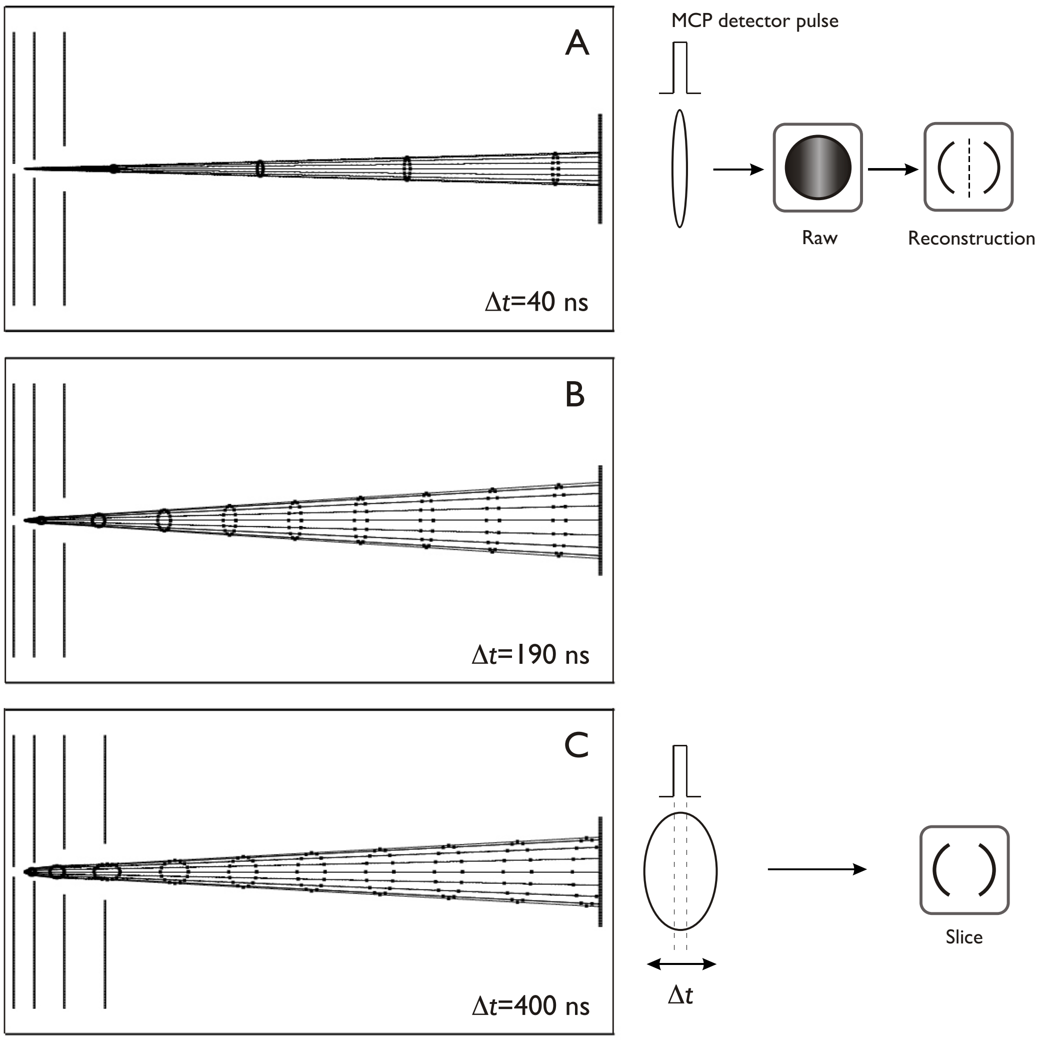

Figure 2.1: Simulations showing the expansion of the photofragment ion cloud at 1.5 μs intervals for ^{35}Cl with 1 eV kinetic energy (adapted from ref.[48]). In each simulation, the leftmost electrode is the repeller (V_R), and the rightmost lens is grounded (L_G). (A) Single focusing lens with V_R = +2500 V, which is a potential setting for conventional velocity mapping imaging. The entire distribution is sampled, and thus, reconstruction is needed to obtain the central section. (B) Single focusing lens with V_R = +500 V. (C) Two focusing lenses with V_R = +500 V, which correspond to a DC slice imaging arrangement. The ion cloud stretches enough to enable direct sampling of the central section.

are employed to sufficiently spread the ion sphere, leading to the increase of arrival time width. Thus, this condition makes the central slice more readily measurable by a narrow gating at the detector and was used for experiments in this research. It should be noted that the “3D” imaging method, nearly equivalent to our slice technique, was developed independently by K. Liu *et al.*.[49]

The key components of the experimental apparatus are shown schematically in Fig. 2.2. A supersonic molecular beam seeded in either Ar or He is expanded into the source chamber *via* a pulsed nozzle operating at 10/30 Hz (depending on a laser system) with a backing pressure of $\sim$ 25 psig. After passing through a skimmer (1.0 mm), the collimated beam enters in a velocity mapping electrode assembly optimized for DC slice imaging and is intersected at 90 ° by two counter-propagating lasers. The photolysis and probe light may be polarized, for which polarization vectors are specified by a coordinate system depicted in Fig. 2.2. The detailed description of it will be examined in Chapter 3. Following ionization by the probe laser, the ion sphere elongated along the flight tube is compressed onto a dual microchannel plate (MCP) array of 75/120 mm diameter, which is coupled to a P-47 phosphor screen. Application of a narrow ($\sim$40 ns) time gate at the detector was then used to sample the central section of the distribution. The resulting signal was recorded using a CCD camera and a photomultiplier tube (PMT), in conjunction with the IMACQ Megapixel acquisition program.[61] This interface software was recently developed in our group, enabling high-resolution real time ion counting.

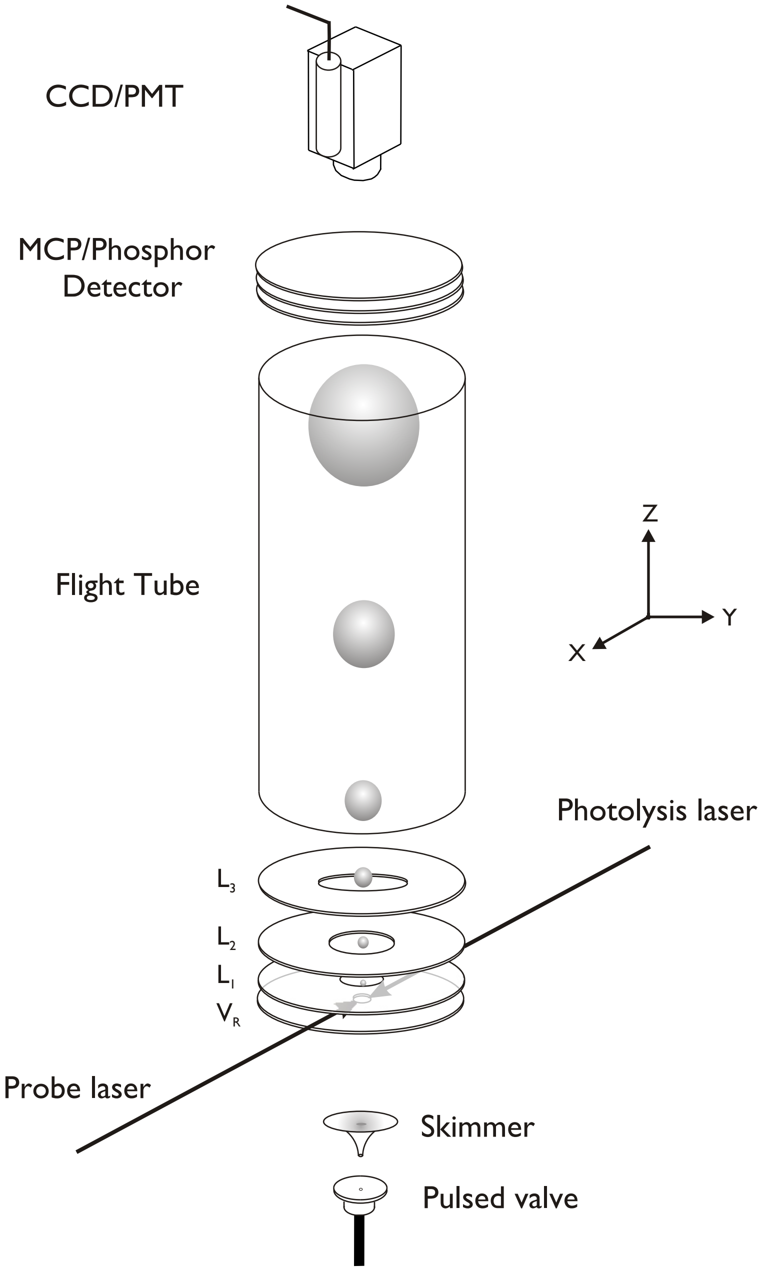

Figure 2.2: Schematic of experimental apparatus for DC slice imaging

2.3.1 Speed and angular distributions for sliced images

The procedure for yielding the speed and angular distributions from sliced images was discussed by previous works, in which conclusions were drawn that the analysis of sliced image is nearly identical to that of conventional ion imaging.[47,48] For thin slices, the resulting sliced image can be considered to be equivalent to the inverse Able transformed image. Application of the standard $\rho \sin\theta$ weighting to the raw sliced data, therefore, is effective to extract the speed distribution, where ρ and θ is the magnitude of the recoil speed and the recoil angle with respect to the axis of cylindrical symmetry, respectively (note that θ here is different from that which is one defined in Fig. 3.1). Recently, Komissarov and co-workers carefully examined the treatment for the data with finite slice widths, usually occurring in the detection of slow fragments.[62] Although incomplete slicing may be achieved for slow fragments, they reported that the $\rho \sin\theta$ weighting can successfully operate to obtain the speed distribution.

The angular distribution from a slice image can be attained in the same way as the traditional one for the reconstructed image, as previously discussed. It should be emphasized again that the angular distribution obtained by the sliced data can be free from artifacts near the cylindrical symmetry axis and can totally reveal the angular anisotropy for any recoil speeds. However, it is still questionable as to the validation of using the same analysis for slow components. Further work will be required to rigorously test the capability of the analysis in the case of the finite slicing. The data for slow fragments presented in this report were carefully examined with the basis images/functions for the unsliced case to confirm their credibility.

Chapter 3

Theory and Data Analysis

3.1 Photofragment Polarization Angular Distribution

In a photodissociation event producing fragments A and B with angular momenta $\mathbf{j_A}$ and $\mathbf{j_B}$ ($\mathbf{j} = \mathbf{j_A} + \mathbf{j_B}$), respectively, the differential excitation cross section matrix elements $\sigma^{(j)}_{m',m}$ for one-photon fragmentation of an AB molecule which has an isotropic angular momentum distribution can be written as[63]

$$\sigma^{(j)}_{m',m}(\theta,\phi) \quad = \quad \frac{4\pi^2\omega}{c(2J_i+1)} \sum_{M_i,M_i'} \langle\Psi_{jm';\mathbf{k}}|\,\mathbf{d}\cdot\mathbf{e}|\Psi_{J_iM_i}\rangle\langle\Psi_{jm;\mathbf{k}}|\,\mathbf{d}\cdot\mathbf{e}|\Psi_{J_iM_i}\rangle^* \qquad (3.1)$$

where ω is the frequency of the incident light, $\mathbf{e}$ is a light polarization vector, and $\mathbf{d}$ is a dipole operator. $\Psi_{J_iM_i}$ is the wave function of the initial molecular state, and $\Psi_{jm;\mathbf{k}}$ is the dissociative wave function describing two photofragments flying apart with momentum $\hbar\mathbf{k}$ and direction specified by the unit vector $\mathbf{k}$ with polar angles θ and ϕ , as shown in Fig. 3.1.

Since the differential cross section is experimentally measured by detecting one of two fragments, the corresponding cross section ($\sigma^{j_A}_{m_A',m_A}$) involves averaging over the

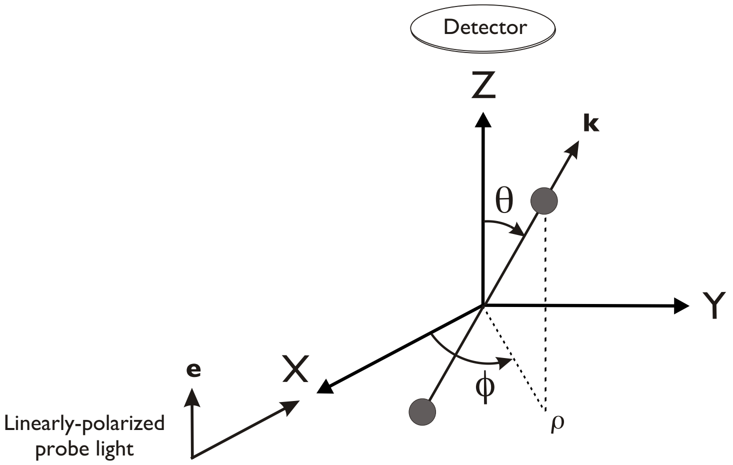

Figure 3.1: Laboratory frame co-ordinate system

quantum numbers of nondetected fragments.[64] The differential cross section matrix elements can be generally expressed in terms of the series of the state multipoles ρ_{KQ} with ranks $K = 0 \ldots 2j_A$ and projections $Q = -K \ldots K$:[63,65]

$$\begin{aligned}\sigma^{j_A}_{m'_A,m_A}(\theta,\phi) &= (2j_A+1)^{1/2}\sigma_0 \sum_{K,Q}(-1)^{j_A-m_A}(2K+1)^{1/2} \\ &\times \begin{pmatrix} j_A & j_A & K \\ m_A & -m'_A & -Q \end{pmatrix} \rho_{KQ}(\theta,\phi) \end{aligned} \tag{3.2}$$

where $\sigma_0 = (2j_A+1)^{-1/2}\langle \mathrm{Tr}[\sigma^{j_A}_{m'_A,m_A}(\theta,\phi)]\rangle$ is the total zeroth-order fragmentation cross section, and the factor in the brackets (:::) in Eq. (3.2) is a Wigner $3-j$ symbol. The recoil-angle-dependent state multipoles describing the angular momentum polarization of photofragments has been derived by Siebbeles *et al.*[7] and extended by Bracker *et al.*[17] in the axial recoil approximation, which are given by

$$\begin{aligned}\rho_{KQ}(\theta,\phi) &= \frac{3}{4\pi}\left(\frac{2K+1}{2j_A+1}\right)^{1/2}\sum_{K_d,q_d,Q'}\sum_{q,q'}(-1)^{K+q'}E_{K_d,q_d}(\mathbf{e})\frac{f_K(q,q')}{f_0(0,0)+2f_0(1,1)}\\ &\times \sqrt{2K_d+1}\begin{pmatrix}1 & 1 & K_d\\ q' & -q & -Q'\end{pmatrix}D^{K*}_{Q,Q'}(\theta,\phi,0)D^{K_d}_{q_d,Q'}(\theta,\phi,0) \qquad (3.3)\end{aligned}$$

where $D^K_{Q,Q'}(\theta,\phi)$ are Wigner rotation matrix elements, and $E_{K_d,q_d}(\mathbf{e})$ is the polarization tensor of the dissociation light. The quantities $f_K(q,q')$ are called the *dynamical functions* because they contain all information on the transition dipole moment and the relevant dissociation dynamics. The indices q, q' ($\Delta\Omega$) are the spherical harmonic components of the molecular electric dipole moment and have the values 0 or ± 1, corresponding to parallel or perpendicular transitions, respectively.[17,64] The dynamical function with $q = q'$ (diagonal terms) represents incoherent excitation, while the off-diagonal terms with $q \neq q'$ represent the simultaneous coherent excitation of different molecular continua.

It is convenient to express the state multipoles in terms of anisotropy polarization parameters, which are composed of normalized combinations of the dynamical functions $f_K(q,q')$. They are associated with different dynamical mechanisms taking place during the dissociation processes, and each of them has a characteristic angular distribution that is governed by the corresponding $3-j$ coefficient and rotation matrix element, as seen in Eq. (3.3). The detailed description of orientation and alignment parameters will be addressed later. The general representations of rank $K = 0, 1, 2$ state multipoles for specific experimental conditions were presented explicitly in the previous studies (see ref.[17] and ref.[14]).

As mentioned above, the state multipole ranges from $K = 0$ to $K = 2j_A$ reflecting the property of the $3 - j$ symbol in Eq. (3.2).[65] The zeroth-rank state multipole ρ_{00} is proportional to the total population of the photofragment magnetic sublevels, and the multipoles with rank $K > 0$ describe the anisotropy of the photofragment angular momenta. For example, the complete description of the $^1D_2$ oxygen atomic photofragments contains up to rank $K = 4$ state multipoles (i.e., $K = 0$ (population), $K = 1$, 3 (orientation), $K = 2$, 4 (alignment)). Although most studies to date have considered rank $K = 1$ orientation and $K = 2$ alignment as the leading contributions to the angular momentum polarization, it is being revealed that the contribution of the higher order $K = 3, 4$ terms is important in some systems, such as O_3.[50, 54] A fully quantum mechanical treatment has been recently extended to include the rank $K = 3, 4$ cases for photofragment orientation[46] and alignment,[55] respectively.

Since all experiments reported here were performed by DC slice imaging, I will only focus on the theoretical treatment and analysis approach to slice imaging. In particular, the contributions of the higher order ($K = 3, 4$) state multipoles to photofragment angular momentum polarization will be considered in detail. As discussed in Chapter 2, the slice imaging technique allows one to exclusively monitor the narrow central section of a given photofragment distribution *for any desired photolysis-probe laser geometry*, which, in the coordinate scheme in Fig. 3.1, corresponds to fixing θ to a value of $\pi/2$.[43] The following expressions are suitable for the 2D central slice case.

3.1.1 Orientation

For two different experimental geometries, the expression of photofragment orientation can be written as the following:

Geometry I. Photolysis light (right circularly polarized) propagates along the X-axis:

$$\begin{aligned}
\rho_{11}(\pi/2,\phi) &= -\frac{3\sqrt{6}}{8\pi\sqrt{2j_A+1}}\,e^{i\phi}\left[\alpha_1\,\cos\phi-\frac{i}{2}\,\gamma_1\,\sin\phi\right]\\
\rho_{31}(\pi/2,\phi) &= \frac{3\sqrt{7}\,V_3(j)}{16\pi\sqrt{2j_A+1}}\,e^{i\phi}\left[\sqrt{3}\,\alpha_3\,\cos\phi-\frac{i}{2\sqrt{2}}\,\gamma_3\,\sin\phi\right]\\
\rho_{33}(\pi/2,\phi) &= -\frac{3\sqrt{35}\,V_3(j)}{16\pi\sqrt{2j_A+1}}\,e^{i3\phi}\left[\alpha_3\,\cos\phi\,-\,i\,\frac{\sqrt{6}}{4}\,\gamma_3\,\sin\phi\right] \qquad (3.4)
\end{aligned}$$

Geometry II. Photolysis light (linearly polarized at 45° to the detector plane) propagates along the X-axis:

$$\begin{aligned}
\rho_{11}(\pi/2,\phi) &= \frac{3\sqrt{6}}{16\pi\sqrt{2j_A+1}}\,i\,e^{i\phi}\,\gamma_1'\,\sin\phi\\
\rho_{31}(\pi/2,\phi) &= \frac{3\sqrt{14}\,V_3(j)}{16\pi\sqrt{2j_A+1}}\,e^{i\phi}\left[\eta_3\,\cos\phi-\frac{i}{4}\,\gamma_3'\,\sin\phi\right]\\
\rho_{33}(\pi/2,\phi) &= \frac{3\sqrt{7}\sqrt{30}\,V_3(j)}{16\pi\sqrt{2j_A+1}}\,e^{i3\phi}\left[\frac{\eta_3}{5}\,\cos\phi\,+\,i\,\frac{\gamma_3'}{4}\,\sin\phi\right] \qquad (3.5)
\end{aligned}$$

where

$$
\begin{aligned}
\alpha_K &= V_K(j_A)^{-1}\,\frac{f_K(1,-1)}{f_0(0,0)+2f_0(1,1)} \\
\gamma_K &= V_K(j_A)^{-1}\,\frac{2\mathrm{Re}[f_K(1,0)]}{f_0(0,0)+2f_0(1,1)} \\
\gamma'_K &= V_K(j_A)^{-1}\,\frac{2\mathrm{Im}[f_K(1,0)]}{f_0(0,0)+2f_0(1,1)} \\
\eta_3 &= -\frac{i\sqrt{5}}{2}V_3(j_A)^{-1}\,\frac{Im[f_3(1,-1)]}{f_0(0,0)+2f_0(1,1)} \qquad (3.6)
\end{aligned}
$$

and $V_1(j_A) = 1$, $V_3(j_A) = j_A(j_A+1)\,/\,[(j_A-1)(j_A+2)(2j_A-1)(2j_A+3)]^{1/2}$

Although there are other state multipoles (e.g., ρ_{10}, ρ_{30}, and ρ_{32}) for both geometries in Eqs. (3.4) and (3.5), ρ_{11}, ρ_{31}, and ρ_{33} were presented here because those are only detected experimentally for the geometry in which the photolysis and probe light are counterpropargating along X-axis, as shown in Eq. (3.14) in the following section. Photofragment orbital orientation can also be produced with linearly polarized dissociation light in cases where the photolysis beam is linearly polarized along either the Y or Z-axis (as would be common in a typical imaging experiment). For this case, the angular distribution of the expectation value of angular momentum arising from rank 1 orientation is proportional to $\sin\theta\cos\theta\sin\phi$ (for the slice imaging case, NO observable value) and is displayed in Fig. 3.2. Therefore, even though the conventional imaging technique is used, the corresponding angular momentum

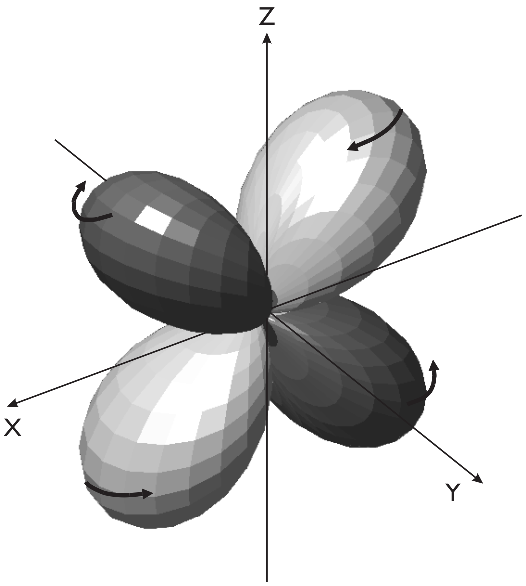

Figure 3.2: Angular dependence of the rank 1 orientation component (ρ_{11}) of the photofragment angular momentum $\mathbf{j}$ for linearly polarized photolysis light along the Y-axis. Black and grey correspond to positive and negative sign, repectively, and the arrow represents the direction of $\mathbf{j}$

distribution is antisymmetric with respect to the reflection in the plane of the detector, and this results in a zero observable orientation effect. However, when the linear polarization is rotated out of the YZ plane, any non-zero γ'_K and η_3 orientation effects that are present become observable and will, in fact, show a maximum value when the polarization is set at an angle of 45° with respect to both the Y and Z-axes.[14]

The rank $K = 1, 3$ orientation anisotropy parameters, α_K, γ_K, γ'_K, and η_3, each characterize the extent to which a distinct physical mechanism plays a role in the overall dissociation dynamics. The parameters α_K and γ_K describe contributions to the fragment orientation from incoherent perpendicular excitation and a coherent superposition of a parallel/perpendicular excitation, respectively. Both parameters result from the photon helicity of dissociation light. Therefore, the helicity must be preserved during dissociation and transfer to photofragments in order to observe these orientations. The parameter γ'_K relates to a coherent superposition of parallel and perpendicular excitations that results from the transition dipole moment aligned to the photolysis light polarization vector **e**. In classical terms, γ'_K is the helicity representing the elliptical motion of the electron charge cloud that is developed by the interference effects *via* a mixed transition.[27] Finally, the η_3 parameter describes orientation from a coherent superposition of two perpendicular transitions.

3.1.2 Alignment

The state mulipoles that are responsible for experimentally observed alignment produced by linearly polarized dissociation light (see Eq. (3.12) and (3.13)) are given by the following:

Geometry III. Photolysis light is linearly polarized along the Z-axis:

$$\rho_{20}(\pi/2,\phi) = -\frac{\sqrt{5}\,V_2(j_A)}{8\pi\sqrt{2j_A+1}}\left[s_2+\alpha_2+\frac{3}{2}\,\eta_2\right]$$

$$\mathrm{Re}[\rho_{22}(\pi/2,\phi)] = \frac{\sqrt{15}\,V_2(j_A)}{8\sqrt{2}\pi\sqrt{2j_A+1}}\left[s_2+\alpha_2-\frac{1}{2}\,\eta_2\right]\cos 2\phi$$

$$\rho_{40}(\pi/2,\phi) = \frac{3\,V_4(j_A)}{32\pi\sqrt{2j_A+1}}\left[3\,(s_4+\alpha_4)+\frac{\sqrt{60}}{2}\,\eta_4\right]$$

$$\mathrm{Re}[\rho_{42}(\pi/2,\phi)] = -\frac{3\,V_4(j_A)}{32\pi\sqrt{2j_A+1}}\left[\sqrt{10}\,(s_4+\alpha_4)+\sqrt{6}\,\eta_4\right]\cos 2\phi$$

$$\mathrm{Re}[\rho_{44}(\pi/2,\phi)] = \frac{3\sqrt{14}\,V_4(j_A)}{64\pi\sqrt{2j_A+1}}\left[\sqrt{5}\,(s_4+\alpha_4)-\sqrt{3}\,\eta_4\right]\cos 4\phi \tag{3.7}$$

Geometry IV. Photolysis light is linearly polarized along the Y-axis:

$$\rho_{20}(\pi/2,\phi) = -\frac{\sqrt{5}\,V_2(j_A)}{8\pi\sqrt{2j_A+1}}\left[s_2+\frac{\alpha_2}{2}\,(3\cos 2\phi-1)-\frac{3}{4}\,\eta_2\,(1+\cos 2\phi)\right]$$

$$\begin{aligned}\mathrm{Re}[\rho_{22}(\pi/2,\phi)] &= \frac{\sqrt{15}\,V_2(j_A)}{8\sqrt{2}\pi\sqrt{2j_A+1}}\left[\left\{s_2+\frac{\alpha_2}{2}\,(3\cos 2\phi-1)\right\}\cos 2\phi\right.\\ &\left.+\gamma_2\,\sin^2 2\phi+\frac{\eta_2}{4}\,(\cos 2\phi+1)\,\cos 2\phi\right]\end{aligned}$$

$$\rho_{40}(\pi/2,\phi) = \frac{9\,V_4(j_A)}{32\pi\sqrt{2j_A+1}}\left[s_4+\frac{\alpha_4}{2}\,(3\cos 2\phi-1)-\frac{\sqrt{15}}{6}\,\eta_4\,(1+\cos 2\phi)\right]$$

$$\begin{aligned}\mathrm{Re}[\rho_{42}(\pi/2,\phi)] &= -\frac{3\sqrt{2}\,V_4(j_A)}{32\pi\sqrt{2j_A+1}}\left[\sqrt{5}\left\{s_4+\frac{\alpha_4}{2}\,(3\cos 2\phi-1)\right\}\cos 2\phi\right.\\ &\left.+\frac{\sqrt{6}}{2}\,\gamma_4\,\sin^2 2\phi-\frac{\sqrt{3}}{2}\,\eta_4\,(\cos 2\phi+1)\,\cos 2\phi\right]\end{aligned}$$

$$\begin{aligned}\mathrm{Re}[\rho_{44}(\pi/2,\phi)] &= \frac{3\sqrt{7}\,V_4(j_A)}{32\pi\sqrt{2j_A+1}}\left[\frac{\sqrt{10}}{2}\left\{s_4+\frac{\alpha_4}{2}\,(3\cos 2\phi-1)\right\}\cos 4\phi\right.\\ &\left.+\sqrt{3}\,\gamma_4\,\sin 2\phi\,\sin 4\phi+\frac{\sqrt{6}}{4}\eta_4\,(\cos 2\phi+1)\,\cos 4\phi\right]\end{aligned} \tag{3.8}$$

where

$$s_K = V_K(j_A)^{-1}\frac{f_K(0,0)+2f_K(1,1)}{f_0(0,0)+2f_0(1,1)}$$

$$\begin{aligned}
\alpha_K &= V_K(j_A)^{-1}\frac{f_K(1,1) - f_K(0,0)}{f_0(0,0) + 2f_0(1,1)} \\
\gamma_K &= 2\sqrt{3}V_K(j_A)^{-1}\frac{\mathrm{Re}[f_K(1,0)]}{f_0(0,0) + 2f_0(1,1)} \\
\gamma'_K &= 2\sqrt{3}V_K(j_A)^{-1}\frac{\mathrm{Im}[f_K(1,0)]}{f_0(0,0) + 2f_0(1,1)} \\
\eta_K &= \sqrt{6}V_K(j_A)^{-1}\frac{f_K(1,-1)]}{f_0(0,0) + 2f_0(1,1)} \qquad (3.9)
\end{aligned}$$

and $V_2(j) = 5\,\{j(j+1)\,/\,[(2j+3)(2j-1)]\}^{1/2}$,

$V_4(j) = 9\,\{(j(j+1))^3\,/\,[(j-1)(j+2)(2j-3)(2j-1)(2j+3)(2j+5)]\}^{1/2}$

The alignment parameters in Eq. (3.9), s_K, α_K, γ_K, and η_K with $K = 2, 4$, describe contributions to the total alignment from incoherent and coherent excitations: s_K and α_K define incoherent excitation via both parallel and perpendicular transitions, with the limiting cases $s_K = 2\alpha_K$ and $\alpha_K = -s_K$ representing pure perpendicular and pure parallel processes, respectively. The γ_K parameters correspond to alignment from a coherent superposition of perpendicular and parallel excitation, while η_K parameters arise from a coherent superposition of two perpendicular transitions. Although it is not presented in the expressions above, the contribution from a coherent superposition of parallel and perpendicular excitation is characterized by γ'_K in the case of circularly-polarized photolysis light.(see Ref.[7]) In this research, it is excluded due to the experimental difficulties of extracting this parameter.

3.1.3 Molecular frame state multipoles

The description of the angular momentum polarization in the molecular frame provides a useful connection to theory. The molecular frame state multipoles normalized by the zeroth-rank state multipole can be easily obtained from those in the laboratory frame using a rotation matrix. In the case of circularly-polarized photolysis light, the molecular frame state multipoles can be expressed as:[66]

Rank 1,3

$$
\begin{aligned}
\rho^{mol}_{K0}(\Theta) &= \sigma\,\frac{3\sqrt{2K+1}\,\alpha_K\,V_K(j)\,\cos\Theta}{\sqrt{2j_i+1}[1-\frac{1}{2}\beta P_2(\cos\Theta)]} \\
\rho^{mol}_{K1}(\Theta) &= \sigma\,\frac{3\sqrt{2K+1}\,\gamma_K\,V_K(j)\,\sin\Theta}{2\sqrt{2}\,\sqrt{2j_i+1}[1-\frac{1}{2}\beta P_2(\cos\Theta)]} \\
&+ \frac{3i\,\sqrt{2K+1}\,\gamma'_K\,V_K(j)\,\sin\Theta\cos\Theta}{2\sqrt{2}\,\sqrt{2j_i+1}[1-\frac{1}{2}\beta P_2(\cos\Theta)]} \\
\rho^{mol}_{32}(\Theta) &= \frac{3}{\sqrt{5}}\frac{\sqrt{2K+1}\,\eta_K\,V_K(j)\,\sin^2\Theta}{\sqrt{2j_i+1}[1-\frac{1}{2}\beta P_2(\Theta)]} \qquad (3.10)
\end{aligned}
$$

Rank 2,4

$$
\rho^{mol}_{K0}(\Theta) = \frac{\sqrt{2K+1}\,V_K(j)\,[s_K+\alpha_K\,P_2(\cos\Theta)]}{\sqrt{2j_i+1}[1-\frac{1}{2}\beta P_2(\Theta)]}
$$

$$
\begin{aligned}
\rho^{mol}_{K1}(\Theta) &= \frac{\sqrt{6}}{4}\frac{\sqrt{2K+1}\,V_K(j)\,\gamma_K\,\sin\Theta\cos\Theta}{\sqrt{2j_i+1}[1-\frac{1}{2}\beta P_2(\cos\Theta)]} \\
&+ \sigma\,\frac{\sqrt{6}\,i}{4}\frac{\sqrt{2K+1}\,V_K(j)\,\gamma'_K\,\sin\Theta}{\sqrt{2j_i+1}[1-\frac{1}{2}\beta P_2(\cos\Theta)]} \\
\rho^{mol}_{K2}(\Theta) &= \frac{\sqrt{6}}{8}\frac{\sqrt{2K+1}\,V_K(j)\,\eta_K\,\sin^2\Theta}{\sqrt{2j_i+1}[1-\frac{1}{2}\beta P_2(\Theta)]} \qquad (3.11)
\end{aligned}
$$

where Θ is the angle between the direction of light propagation and the recoil axis and the values of the index $\sigma = +1$ and $\sigma = -1$ correspond to the right and left light circular polarization, respectively. It is clear from Eq. (3.10) that the parameters α_K are responsible for the photofragment electronic angular momentum which is parallel to the recoil direction **v**, while the parameters γ_K are responsible for the angular momentum which is perpendicular to the recoil direction and lies in the plane defined by the recoil vector **v** and the propagation direction of the photolysis laser beam (see Fig. 3.3). The parameter γ'_1 is attributed to angular momentum perpendicular both to the recoil vector **v** and to the photolysis light polarization vector **e**. All molecular frame state multipoles can be used to produce the electron charge cloud distribution[39, 65] and the full density matrix of the atomic fragment[65] that is dependent on recoil direction, giving information on the molecular frame dynamics. The electron charge cloud and photofragment density matrix will be discussed more in the final section of this chapter.

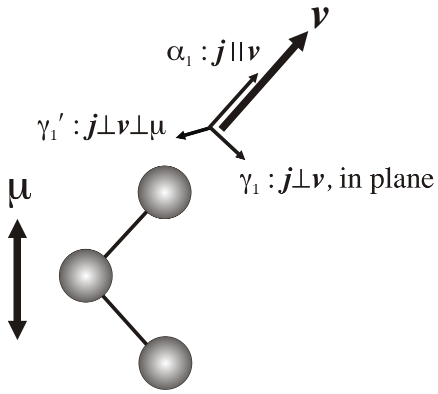

Figure 3.3: Cartoon showing orientation of angular momentum vectors corresponding to each orientation anisotropy parameter relative to transition dipole moment $\boldsymbol{\mu}$ and recoil direction $\mathbf{v}$.

3.2 Two-photon Excitation Probability of Photofragments

As shown by Kummel and coworkers,[67,68] the general expression describing the absorption intensity of polarized light by photofragments via a two-photon transition can be expressed in terms of the state multipoles ρ_{KQ}. For different experimental geometries, the expressions for the 2+1 Resonance-Enhanced Multiphoton Ionization (REMPI) probing are

$$\mathrm{I}_Z = C\left[P_0\,\rho_{00} + P_2\,\rho_{20} + P_4\,\rho_{40}\right] \tag{3.12}$$

$$\begin{aligned}\mathrm{I}_{X,Y} = C\Big[&P_0\,\rho_{00} - \frac{P_2}{2}\Big\{\rho_{20} \mp \sqrt{6}\mathrm{Re}[\rho_{22}]\Big\}\\ &+\frac{P_4}{8}\Big\{3\rho_{40} \pm 2\sqrt{10}\mathrm{Re}[\rho_{42}] + \sqrt{70}\mathrm{Rd}[\rho_{44}]\Big\}\Big]\end{aligned} \tag{3.13}$$

$$
\begin{aligned}
\mathrm{I}^X_{R,L} \;=\; C \Bigg[& P^c_0\,\rho_{00} \;\pm\; \sqrt{2}\,P^c_1\,\mathrm{Re}[\rho_{11}] \;-\; \frac{1}{2}\,P^c_2\,\rho_{20} \\
& + \frac{\sqrt{6}}{2}\,P^c_2\,\mathrm{Re}[\rho_{22}] \;\mp\; \frac{\sqrt{3}}{2}\,P^c_3\,\mathrm{Re}[\rho_{31}] \;\pm\; \frac{\sqrt{5}}{2}\,P^c_3\,\mathrm{Re}[\rho_{33}] \\
& + \frac{3}{8}\,P^c_4\,\rho_{40} \;-\; \frac{\sqrt{10}}{4}\,P^c_4\,\mathrm{Re}[\rho_{42}] \;+\; \frac{\sqrt{70}}{8}\,P^c_4\,\mathrm{Re}[\rho_{44}] \Bigg]
\end{aligned}
\qquad (3.14)
$$

where I_X, I_Y, and I_Z are absorption intensities related to linearly polarized probe light with polarization vectors directed along the X, Y, and Z axes, respectively, and $\mathrm{I}^X_{R,L}$ corresponds to circularly polarized probe light propagating along the $-X$-axis. The $+$ and $-$ of $\mp$ in Eq. (3.13) correspond to the linear polarization along the X and Y-axis, respectively, while the $+$ and $-$ of $\pm$ in Eq. (3.14) correspond to the right and left circularly polarized light, respectively. The constant C depends on the intensity of the probe light, and P_K and P^c_K are linestrength factors for linearly and circularly polarized probe light, respectively.[14]

Usually, the spatial modulations in an ion image which result from photofragment orientation and alignment represent a relatively small fraction of the total signal, as mentioned earlier. For this reason, it is useful to isolate these contributions by taking linear combinations of the signal recorded under different experimental geometries of the photolysis and probe laser polarizations, in such a way that the population term ρ_{00} cancels. Specifically, for the case of probing photofragment orientation, the following combination of signals can be used to isolate the rank $K = 1, 3$ state multipoles from the rank $K = 0, 2$, and 4 ones:

$$
\frac{\mathrm{I}^X_R \;-\; \mathrm{I}^X_L}{\langle \mathrm{I}_Z \rangle \;+\; \langle \mathrm{I}_Y \rangle \;-\; \frac{1}{3}\left[\langle \mathrm{I}^X_R \rangle \;+\; \langle \mathrm{I}^X_L \rangle\right]} \;=
$$

$$2\sqrt{2j_A+1}\left[\sqrt{2}\,\frac{P_1^c}{P_0}\,\mathrm{Re}[\rho_{11}] \;-\; \frac{P_3^c}{2\,P_0}\left\{\sqrt{3}\,\mathrm{Re}[\rho_{31}] - \sqrt{5}\,\mathrm{Re}[\rho_{33}]\right\}\right] \qquad (3.15)$$

In the case of probing alignment, the isolation of the rank $K = 2, 4$ state multipoles from the population and orientation terms can be achieved by the linear combination of ion images recorded with the probe light linearly polarized along the Z and Y-axis:

$$\frac{\mathrm{I}_Z \;-\; \mathrm{I}_Y}{\langle \mathrm{I}_X\rangle \;+\; \langle \mathrm{I}_Y\rangle \;+\; \langle \mathrm{I}_Z\rangle} \;=\; \frac{\sqrt{2j_A+1}}{2}\left[\frac{P_2}{P_0}\left\{\rho_{20} \;+\; \frac{\sqrt{6}}{3}\mathrm{Re}[\rho_{22}]\right\} + \frac{P_4}{12P_0}\left\{5\rho_{40} \;-\; 2\sqrt{10}\mathrm{Re}[\rho_{42}] - \sqrt{70}\mathrm{Re}[\rho_{44}]\right\}\right] \qquad (3.16)$$

Both denominators on the right hand side in Eqs. (3.15) and (3.16) are normalization factors proportional to the total population of all magnetic sublevels,[14] $\langle \rho_{00}(\theta, \phi)\rangle$, and the angular brackets denote an averaging of the corresponding absorption intensities over all recoil angles. The denominator in Eq. (3.15), however, has an experimental advantage over that used in Eqs. (3.16). Since the determination of fragment population for any fragment angular space distribution can be carried out by changing only the probe laser polarization without moving the laser beam direction,[14] this would be a more direct method for normalizing the measurements. The linestrength factors P_K^c in Eqs. (3.12)$-$(3.16) for a (2+1) REMPI probe scheme may be simply evaluated from the following expression given by Mo and Suzuki:[69]

$$\frac{P_K^c}{P_0} \;=\; 5\sqrt{2K+1}\,\sqrt{2j_i+1}\,(-1)^{j_f+j_i}\begin{pmatrix} 2 & 2 & K \\ 2s & -2s & 0 \end{pmatrix}\begin{Bmatrix} j_i & j_i & K \\ 2 & 2 & j_f \end{Bmatrix} \qquad (3.17)$$

Table 3.1: Linestrength factors of two different 2+1 REMPI transitions by circularly- and linearly-polarized light.

Cicular	$^1F_3$	$^1P_1$	*Linear*	$^1F_3$	$^1P_1$
$P_1^c\,/\,P_0$	0	-1.181	$P_2\,/\,P_0$	0.683	-0.598
$P_3^c\,/\,P_0$	-0.253	0	$P_4\,/\,P_0$	-0.115	-1.069

Here j_i and j_f are the initial and final total angular momenta of the detected atom, respectively, and s, the projection of the molecular electronic dipole moment onto the direction of the probe beam, takes a value of 0 for a linearly polarized probe, +1 for right hand circular polarization, and -1 for left hand circular polarization. For instance, the linestrength factors which are relevant to the $^1D_2 \rightarrow\rightarrow\ ^1F_3$ and $^1D_2 \rightarrow\rightarrow\ ^1P_1$ two-photon REMPI transitions in oxygen/sulfur atom are calculated substituting $j_i = 2$, $j_f = 1$, and $s = +1$ or 0 into Eq. (3.17), which are presented in Table 3.1. It is seen from Table 3.1 that the $^1D_2 \rightarrow\rightarrow\ ^1F_3$ transition is sensitive only to the $K = 3$ state multipole, while the $^1D_2 \rightarrow\rightarrow\ ^1P_1$ transition is sensitive only to the $K = 1$ state multipole. That is, the contribution of the $K = 1$ and $K = 3$ state multipoles to the experimental signal can be determined independently. It is more difficult to extract the rank 4 contribution because, although the sensitivity of the $^1P_1$ is about ten times higher than that of $^1F_3$, the linestrength factors are nonzero for each of the two transitions. The recent work of Smolin *et.al* has shown a way to isolate the rank 4 moments from all others experimentally.[55] However, in this particular instance, it is convenient to obtain the $K = 4$ moments by fitting to the experimental image obtained *via* the $^1P_1$ transition using the fixed values of the $K = 2$ moments measured *via* the $^1F_3$ transition. The signals detected through the

$^1F_3$ transition can be used to extract the $K = 2$ moments, neglecting the contribution of the $K = 4$ moments.

As mentioned previously, the signal measured by DC slice imaging, the central part of the total three-dimensional absorption signal, corresponds to a fixing θ to a value of $\pi/2$. Substituting the state multipoles for the case of sliced images into Eq. (3.15) and (3.16), the explicit expressions to obtain alignment and orientation are given by the following:

Orientation

Geometry I. Photolysis (right circularly polarized) and probe light (right or left circularly polarized) propagate along the X and $-X$-axis, respectively:

$$\begin{aligned}
&\frac{\mathrm{I}_R^X(\frac{\pi}{2},\phi)\;-\;\mathrm{I}_L^X(\frac{\pi}{2},\phi)}{\langle\mathrm{I}_Z(\frac{\pi}{2},\phi)\rangle\;+\;\langle\mathrm{I}_Y(\frac{\pi}{2},\phi)\rangle\;-\;\frac{1}{3}\Big[\langle\mathrm{I}_R^X(\frac{\pi}{2},\phi)\rangle\;+\;\langle\mathrm{I}_L^X(\frac{\pi}{2},\phi)\rangle\Big]} = \qquad (3.18)\\
&\quad -\frac{3\sqrt{3}}{(1-\beta/8)\pi}\left[\frac{P_1^c}{P_0}\left\{\alpha_1\,\cos^2\phi+\frac{\gamma_1}{2}\,\sin^2\phi\right\}+\frac{P_3^c}{P_0}\,\frac{\sqrt{7}\,V_3(j)}{2\sqrt{3}}\left\{\alpha_3\,\cos^2\phi\,(5\,\cos^2\phi-3)\right.\right.\\
&\quad \left.\left.+\,\gamma_3\,\frac{\sqrt{6}}{4}\,\sin^2\phi\,(5\,\cos^2\phi-1)\right\}\right]
\end{aligned}$$

Geometry II. Photolysis and probe light counterpropagate along the X-axis, with the photolysis light linearly polarized at 45° to the detector plane and the probe light circularly polarized:

$$\begin{aligned}
&\frac{\mathrm{I}_R^X(\frac{\pi}{2},\phi)\;-\;\mathrm{I}_L^X(\frac{\pi}{2},\phi)}{\langle\mathrm{I}_Z(\frac{\pi}{2},\phi)\rangle\;+\;\langle\mathrm{I}_Y(\frac{\pi}{2},\phi)\rangle\;-\;\frac{1}{3}\Big[\langle\mathrm{I}_R^X(\frac{\pi}{2},\phi)\rangle\;+\;\langle\mathrm{I}_L^X(\frac{\pi}{2},\phi)\rangle\Big]} = \qquad (3.19)\\
&\quad -\frac{3\sqrt{3}}{(1-\beta/8)\pi}\,\frac{\sin^2\phi}{2}\left[\frac{P_1^c}{P_0}\,\gamma_1'+\frac{P_3^c}{P_0}\,\sqrt{14}\,V_3(j)\left\{\frac{\gamma_3'}{4}\,(5\,\cos^2\phi-1)+\eta_3\,\cos^2\phi\right\}\right]
\end{aligned}$$

Alignment

Geometry III. Photolysis and probe light counterpropagate along the X-axis, with the photolysis light linearly polarized along the Z-axis:

$$\begin{aligned}
&\frac{\mathrm{I}_Z(\frac{\pi}{2},\,\phi) \;-\; \mathrm{I}_Y(\frac{\pi}{2},\,\phi)}{\langle \mathrm{I}_X(\frac{\pi}{2},\,\phi)\rangle \;+\; \langle \mathrm{I}_Y(\frac{\pi}{2},\,\phi)\rangle \;+\; \langle \mathrm{I}_Z(\frac{\pi}{2},\,\phi)\rangle} \;= \qquad (3.20)\\
&\quad \frac{1}{(1-\beta/2)}\left[\frac{C'\,P_2}{2\,P_0}\left\{(s_2+\alpha_2)\,(\cos 2\phi - 1) - \frac{1}{2}\,\eta_2\,(3+\cos 2\phi)\right\}\right.\\
&\quad \left. + \frac{C''\,P_4}{12\,P_0}\left\{5\,(s_4+\alpha_4)\,(3+4\,\cos 2\phi - 7\,\cos 4\phi) + \sqrt{15}\,\eta_4\,(5+4\,\cos 2\phi + 7\,\cos 4\phi)\right\}\right]
\end{aligned}$$

Geometry IV. Photolysis and probe light counterpropagate along the X-axis, with the photolysis light linearly polarized along the Y-axis:

$$\begin{aligned}
&\frac{\mathrm{I}_Z(\frac{\pi}{2},\,\phi) \;-\; \mathrm{I}_Y(\frac{\pi}{2},\,\phi)}{\langle \mathrm{I}_X(\frac{\pi}{2},\,\phi)\rangle \;+\; \langle \mathrm{I}_Y(\frac{\pi}{2},\,\phi)\rangle \;+\; \langle \mathrm{I}_Z(\frac{\pi}{2},\,\phi)\rangle} \;=\; \frac{1}{(1+\beta/4)}\left[\frac{C'\,P_2}{2\,P_0}\left\{s_2\,(\cos 2\phi - 1)\right.\right.\\
&\quad \left. + \frac{\alpha_2}{2}\,(3\,\cos^2 2\phi - 4\,\cos 2\phi + 1) \;+\; \gamma_2\,\sin^2 2\phi + \frac{\eta_2}{4}\,(\cos^2 2\phi + 4\,\cos 2\phi + 3)\right\}\\
&\quad + \frac{C''\,P_4}{12\,P_0}\left\{\frac{5}{2}\,(2\,s_4 + \alpha_4\,(3\,\cos 2\phi - 1))(3 + 4\,\cos 2\phi - 7\,\cos 4\phi)\right.\\
&\quad - 2\,\sqrt{30}\,\gamma_4\,(5 + 12\,\cos 2\phi + 7\,\cos 4\phi)\,\sin^2\phi\\
&\quad \left.\left. - \frac{\sqrt{15}}{4}\,\eta_4\,(14 + 25\,\cos 2\phi + 18\,\cos 4\phi + 7\,\cos 6\phi)\right\}\right] \qquad (3.21)
\end{aligned}$$

where $C' = \sqrt{5}\,V_2(j)/4\pi$, $C'' = 3\,V_4(j)/32\pi$

The sliced image can be normalized by the zeroth-rank fragment state multipole $\rho_{00}(\theta,\phi)$ integrated over the azimuthal angle ϕ at the fixed value of the polar angle $\theta = \pi/2$. In practice, the measurement of I_X may be impossible for the photolysis laser polarized along the Y-axis case (defined here as Geometry IV), which precludes proper normalization. However, when the polarization of the photolysis laser lies parallel to the Z-axis (Geometry III), this problem can be circumvented since the overall photofragment distribution will exhibit equal sensitivity to both X- and Y-axis probe light polarization. That is, the total signal intensity of I_X is the same as that of I_Y. Taking this fact into account, the alignment anisotropy parameters, such as η_2 and $s_2 + \alpha_2$, were measured for the geometry III (see Eq. (3.20)) and used to normalize the data for the geometry IV. The experimental results from the geometry III setup were not used exclusively because they do not give us γ_2 and independent s_2 and α_2 parameters. An alternative way to normalize the data for the geometry IV is to use the normalization factor shown as the denominator in Eqs. (3.18) and (3.19). In this case, the geometry III experiment would be unnecessary.

From the above Eqs. (3.18)−(3.19), it is apparent that each polarization parameter has a unique angular distribution. The angular dependence associated with each distinct dissociation mechanism is plotted in Fig. 3.4 and 3.5. These polarization anisotropy "basis" functions are the specific case of the alignment/orientation image basis functions for monoenergetic atomic fragments described by Vasyutinskii and co-workers.[17,46,55] The orientation and alignment parameters *for any given photofragment recoil velocity* can be extracted by fitting the experimental data with the basis set using a simple linear fitting algorithm, and then, a complete picture of the mechanism in the photodissociation event is directly revealed in the result. In particular, in the case of probing only rank 1 orientation following linear photolysis (e. g., $^1P_1$ REMPI transition of O atom), the orientation parameter can be directly obtained without any fitting process by integrating the numerator of Eq. (3.19) over

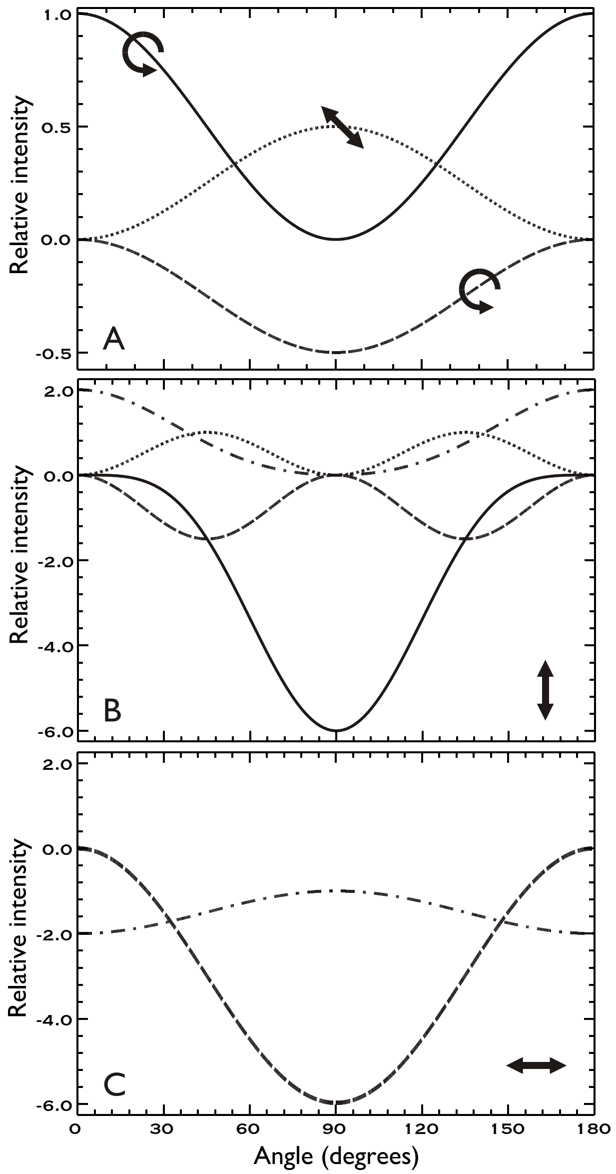

Figure 3.4: Slice imaging polarization anisotropy basis functions. (A) $K = 1$ orientation: incoherent perpendicular (α_1, solid line) and coherent perpendicular/parallel (γ_1, dashed line) resulting from circular photolysis, coherent perpendicular/parallel excitation (γ_1', dotted line) resulting from linear photolysis. (B), (C) $K = 2$ alignment: incoherent parallel ($s_2 = -\alpha_2$, solid line), incoherent perpendicular ($s_2 = 2\alpha_2$, dashed line), coherent perpendicular/parallel (γ_2, dotted line), and coherent perpendicular (η_2, dot-dashed line) resulting from linear photolysis. Note that an angle of 90° corresponds to vertical in the ion image.

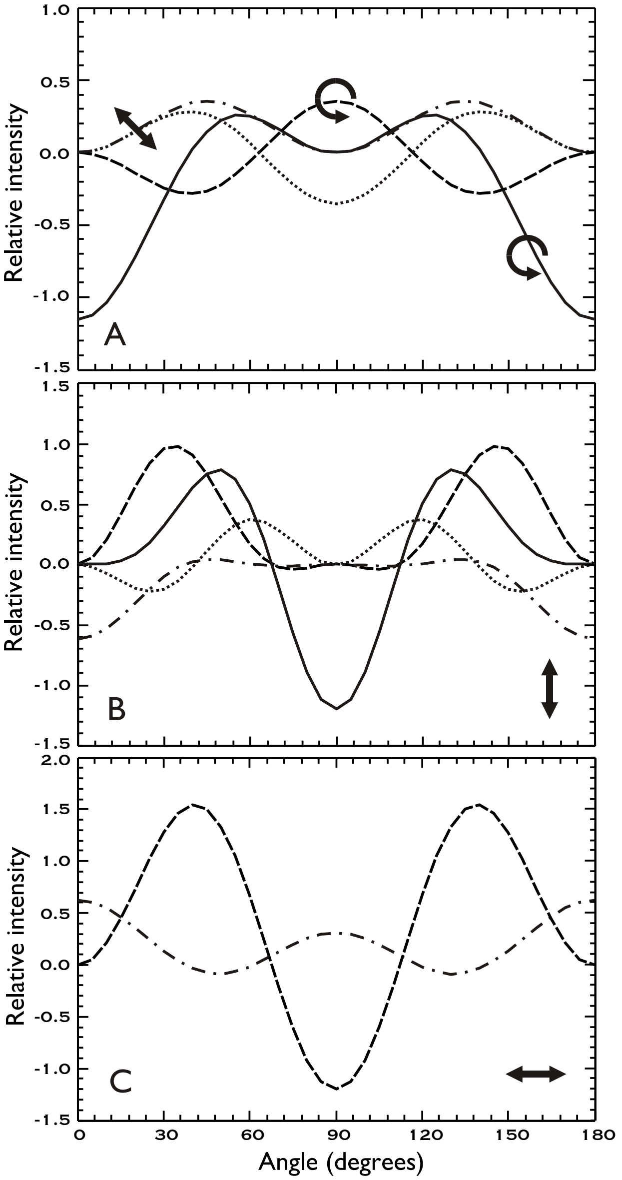

Figure 3.5: Slice imaging polarization anisotropy basis functions. (A) $K = 3$ orientation: incoherent perpendicular (α_3, solid line) and coherent perpendicular/parallel (γ_3, dashed line) resulting from circular photolysis, coherent perpendicular/parallel excitation (γ'_3, dotted line) and coherent perpendicular (η_3, dot-dashed line) resulting from linear photolysis. (B), (C) $K = 4$ alignment: incoherent parallel ($s_4 = -\alpha_4$, solid line), incoherent perpendicular ($s_4 = 2\alpha_4$, dashed line), coherent perpendicular/parallel (γ_4, dotted line), and coherent perpendicular (η_4, dot-dashed line) resulting from linear photolysis.

the azimuthal angle ϕ at any given recoil velocity. The resulting expression is written as:

$$\frac{\langle \mathrm{I}_R^X(\frac{\pi}{2},\phi)\rangle - \langle \mathrm{I}_L^X(\frac{\pi}{2},\phi)\rangle}{\langle \mathrm{I}_Z(\frac{\pi}{2},\phi)\rangle + \langle \mathrm{I}_Y(\frac{\pi}{2},\phi)\rangle - \frac{1}{3}\left[\langle \mathrm{I}_R^X(\frac{\pi}{2},\phi)\rangle + \langle \mathrm{I}_L^X(\frac{\pi}{2},\phi)\rangle\right]} = -\frac{3\sqrt{3}}{(1-\beta/8)}\frac{P_1^c}{P_0}\frac{\gamma_1'}{2} \tag{3.22}$$

It is important to note that in simplifying the expression of Bracker *et al.* (ref.[17]) from the case where the entire photofragment distribution is observed to one where only the central section is sampled, sensitivity to all distinct polarization mechanisms that are possible is retained. This represents a significant improvement over the original analyzing approach of Ref.[17] since slice imaging removes the need to manipulate the data with radial convolution functions in order to account for the fact that in conventional ion imaging experiments, the 3D photofragment distribution is compressed onto a 2D detector.

3.3 Photofragment Density Matrix

A thorough analysis of angular momentum polarization allows the construction of the full molecular frame atomic photofragment density matrix, explicitly including the relative population of each magnetic sublevel and the coherences embodied in the off-diagonal elements. The density matrix describing the atomic ensemble of interest can be expressed in terms of state multipoles, as given in Eq. (3.2). Hence, the molecular frame dynamics for any recoil angle can be examined by building up the photofragment density matrix with observable state multipoles that are transformed in the molecular frame using Eqs. (3.10) and (3.11). The diagonal elements of the matrix, representing the probability of finding the fragment in a specific magnetic sublevel, consist of the linear combination of the $Q = 0$ state multipoles, ρ_{K0}. In the case of $j = 2$, the contribution of each $Q = 0$ state multipole to the diagonal terms of a 5×5 density matrix is shown in Fig. 3.6.

If there is no orientation or alignment, the distribution of magnetic sublevel populations is isotropic, while if either orientation or alignment exists, the distribution is changed depending on the extent of the polarization and can manifest the correlation between recoil velocity ($\mathbf{v}$) and angular momemtum ($\mathbf{j}$) for a system. The non-zero off-diagonal elements point at the presence of the interference ("*coherent superposition*") in the system. Furthermore, it should be mentioned that the total cross section, associated with the total number of fragments, is obtained by summing up the populations of magnetic sublevels for all recoil angles and is proportional to $\langle\rho_{00}\rangle$. This result is to be expected since the summation of the coefficient for each non-zero rank multipole over magnetic sublevels becomes zero (see Fig. 3.6), leading to no contributions of polarization terms to the total population.

The physical significance of the photofragment density matrix is easily seen by considering the shape of the electron charge cloud, corresponding to the alignment of the total orbital angular momentum L. The charge distribution of atomic photofragments described by the density matrix can be transformed in terms of state multipoles. In particular, the expression of charge density for an atom with two unpaired electrons discussed by Vasyutinskii and co-workers[39] can be written as

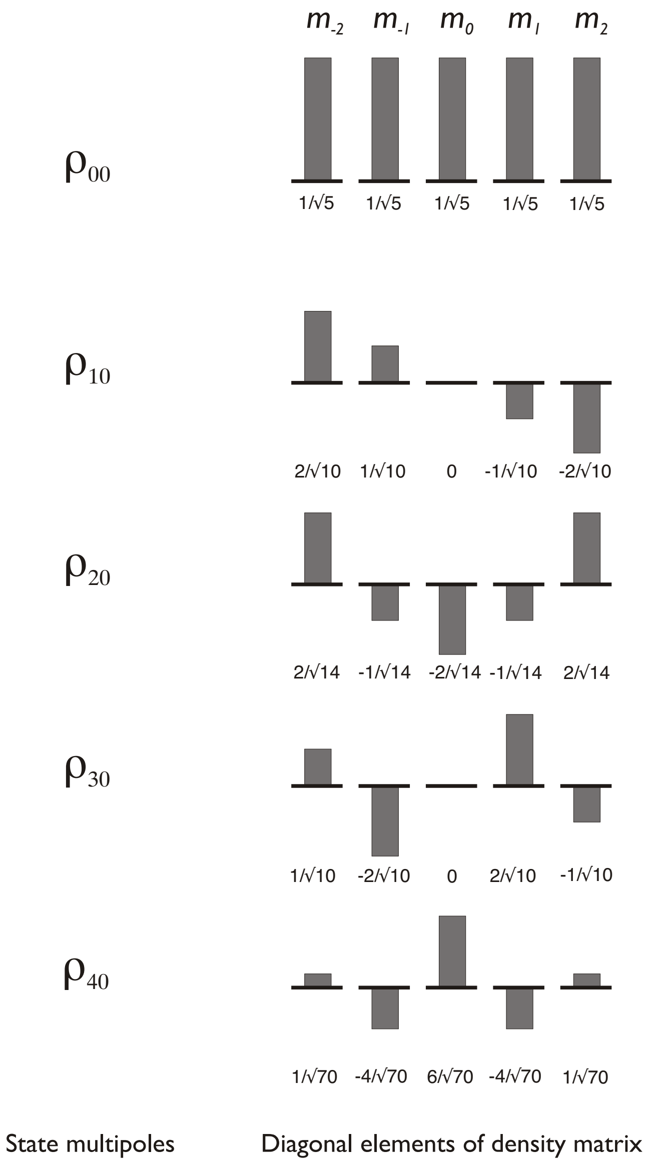

Figure 3.6: The contributions of the $Q = 0$ state multipoles, ρ_{K0}, to the diagonal elements of the density matrix for an atomic system with $j = 2$. The number below each magnetic sublevel corresponds to the coefficient of the state multipole.

$$N(\theta,\phi) = (-1)^{L+l}\,\frac{6(2L+1)}{\sqrt{4\pi}}\sum_{K,Q}\frac{C^{K0}_{l0l0}}{\sqrt{2K+1}}\left\{\begin{array}{ccc} L & L & K \\ l & l & l \end{array}\right\}\Psi_{KQ}(\theta,\phi)\,\rho_{KQ}(L) \tag{3.23}$$

where $\Psi_{KQ}(\theta,\phi)$ is a spherical harmonic. In the case of an $O(^1D_2)$ atom, $L = 2$ and $l = 1$ substitute in the $6-j$ symbols, so the final expression for the charge cloud is given by

$$\begin{aligned} N(\theta,\phi) \;&=\; \frac{\sqrt{5}}{2\pi}\left\{\rho_{00} - \frac{\sqrt{14}}{4\sqrt{5}}(3\cos^2\theta - 1)\,\rho_{20} + \sqrt{\frac{21}{5}}\cos\theta\sin\theta\cos\phi\,\mathrm{Re}[\rho_{21}]\right. \\ &\left. -\frac{\sqrt{21}}{2\sqrt{5}}\sin^2\theta\cos 2\phi\,\rho_{22}\right\} \end{aligned} \tag{3.24}$$

where the rank $K = 4$ multipoles and imaginary parts are omitted from consideration. The above Eqs. 3.23 and 3.24 show that the charge cloud consists of two contributions, isotropic (ρ_{00}) and anisotropic (ρ_{2Q}).[65] Each state multipole has a characteristic angular distribution, independent of the recoil direction: the charge distribution arising from the state multipoles with zero component (represented by incoherent transition) have cylindrical symmetry, while one arising from the state multipoles describing coherences has azimuthal asymmetry. The shape of the charge cloud, however, will vary with the recoil angle since the relative contribution of each angular distribution, determined by the value of the corresponding state multipole, is different depending on the recoil direction.[17] Therefore, the appearance of the electron charge cloud will directly reflect the measured alignment parameters, which in turn, will provide dynamical information on photodissociation of interest.

Chapter 4

Photodissociation of Polyatomic Molecules

4.1 Ethylene Sulfide

4.1.1 Introduction

The photofragmentation of ethylene sulfide has received considerable attention both experimentally and theoretically due to the production of important radicals. In particular, the 193 nm photolysis of ethylene sulfide has been studied using photofragment translational spectroscopy (PTS)[70] and Doppler-broadened laser-induced fluorescence (LIF) spectroscopy.[71] More recently, Qi and co-workers[72,73] reported a trimodal translational energy distribution of S($^1D_2$) fragments and the presence of a channel producing S(^3P) fragments by probing with VUV synchrotron radiation. For excitation at 193.3 nm, it is known that the S($^1D_2$) + C_2H_4 (^1A_g) channel is the dominant dissociation process, and the S(^3P):S($^1D_2$) branching ratio has been reported as 1.4:1.[73] Sulfur ($^1D_2$) atoms are believed to be yielded *via* three different potential energy surfaces following excitation from a non-bonding orbital localized on S-atom to a 4p$_x$ Rydberg state,[74] with a broad continuum of photofragment kinetic energies in the approximate range $0 - 2.6$ eV. Previous studies have proposed that the initial excitation occurs predominantly on a single electronic state that may dissociate directly to produce translationally hot sulfur atoms, while less energetic fragments arise from internal conversion prior to dissociation. The recoil-energy averaged value of velocity anisotropy (β) has been determined to be around 1.1,[70,71] indicating that a parallel transition is dominant in nature.

The alignment measurement of S($^1D_2$) photofragments could suggest explicitly more detailed dynamics of ethylene sulfide dissociation, especially clarifying the possible different mechanisms corresponding to three distinct regions in translational energy distribution. I present here the alignment anisotropy parameters of S($^1D_2$) atom for any recoil speeds measured from the experimental images obtained by using the DC slice imaging technique.

4.1.2 Experiment

The overall experimental set-up for DC slice imaging is essentially the same as that described in detail in Chapter 2; thus, only the key details specific to this study will be summarized here. Argon was bubbled through an ethylene sulfide sample (Sigma-Aldrich, 98%) in an ice bath. A gas sample, a 10 % mixture of c-C_2H_4S in Ar at a backing pressure of $\sim$ 1.5 bar, was expanded into the source chamber *via* a pulsed nozzle operating at 10 Hz. The photolysis laser was provided by an ArF excimer system (GAM EX10/600). In order to produce only the beam with a linear polarization parallel to the detector plane, the laser output was first allowed to propagate through a total of eight fused silica windows set at Brewster's angle (33° in this instance) before being focused into the interaction region using a 30 cm lens. The photolysis laser power was $\sim$ 0.5 mJ/pulse. The probe laser was generated by frequency doubling the output of a dye laser (Continuum Jaguar, R590/R610 dyes) pumped by a Nd:YAG system at 532 nm (Quanta Ray GCR-5). Control over the probe polarization was achieved using a Soleil-Babinet compensator (special optics), and then the probe beam was focused into the chamber using a second 30 cm lens. Typical output power for the doubled dye laser beam was $\sim$ 2 mJ/pulse, and accurate wavelength calibration was achieved using a wavemeter (Coherent WaveMaster). The $\mathrm{S}(^1D_2)$ atomic photofragments produced in the dissociation event were probed using the following (2+1) REMPI scheme:

$$\mathrm{S}\ 3p^4(^1D_2) \xrightarrow{2h\nu} \mathrm{S}\ 3p^3 4p(^1F_3) \xrightarrow{h\nu} \mathrm{S}^+ \qquad 288.179\,\mathrm{nm} \tag{4.1}$$

After ionization, the S-atom fragments were accelerated through the multi-lens velocity mapping assembly and impacted upon a position sensitive dual MCP/phosphor screen detector of 120 mm diameter. In this particular instance a repeller electrode held at +550 V was used in conjunction with three additional focusing lenses in the velocity-mapping scheme to stretch the photofragment ion cloud along the time-of-flight axis to around 340 ns. The overall flight path from the interaction region to the detector was 130 cm. The resulting image was recorded using a CCD camera (Mintron 2821e, 512 × 480 pixels) in conjunction with PC acquisition software (McLaren Research) that enabled real time event counting of the data.

4.1.3 Results

DC sliced images were acquired for S atomic fragments under the experimental condition (Geometry IV defined in Chapter 3) that the Y-polarized photolysis laser was used with both Z- and Y-polarized probe lasers, which are shown in Fig. 4.1. Three broad features are distinguished in the images and more clearly in the speed distribution plotted in Fig. 4.2 A, which is consistent with previous work.[72] Significant recoil anisotropy (characterized by β, here referred to as β_0) was observed and is largely parallel for the overall speed range, implying a predominant parallel excitation. However, the extent of the recoil anisotropy clearly exhibits a strong correlation to the S-atom recoil speed (Fig. 4.2 A): The anisotropy decreases from a maximum of $\beta_0 \sim 1.5$ for the fastest fragments to a minimum of $\beta_0 \sim 0.3$ at the lowest recoil speed. A recoil energy-averaged value is $\beta_0 = 1.22 \pm 0.15$, which is in reasonable agreement with previously reported values.[70,71]

The alignment image (difference image in Fig. 4.1 C) is obtained by subtracting Fig. 4.1 A from Fig. 4.1 B, as discussed in Chapter 3. From the distinct angular distribution in the alignment image, it is immediately noticeable that S($^1D_2$) atomic orbital alignment is strikingly dependent upon the recoil speed: There are three discrete regions, which correspond well the three dissociation pathways that may be seen in Fig. 4.2 A. For the fastest S-atom fragments (1950-2700 ms^{-1}), the angular distribution with four lobes is displayed, and the middle region (1350-1950 ms^{-1}) shows essentially zero alignment. In the case of the slowest fragments (0-1350 ms^{-1}), the distribution has a perpendicular anisotropy.

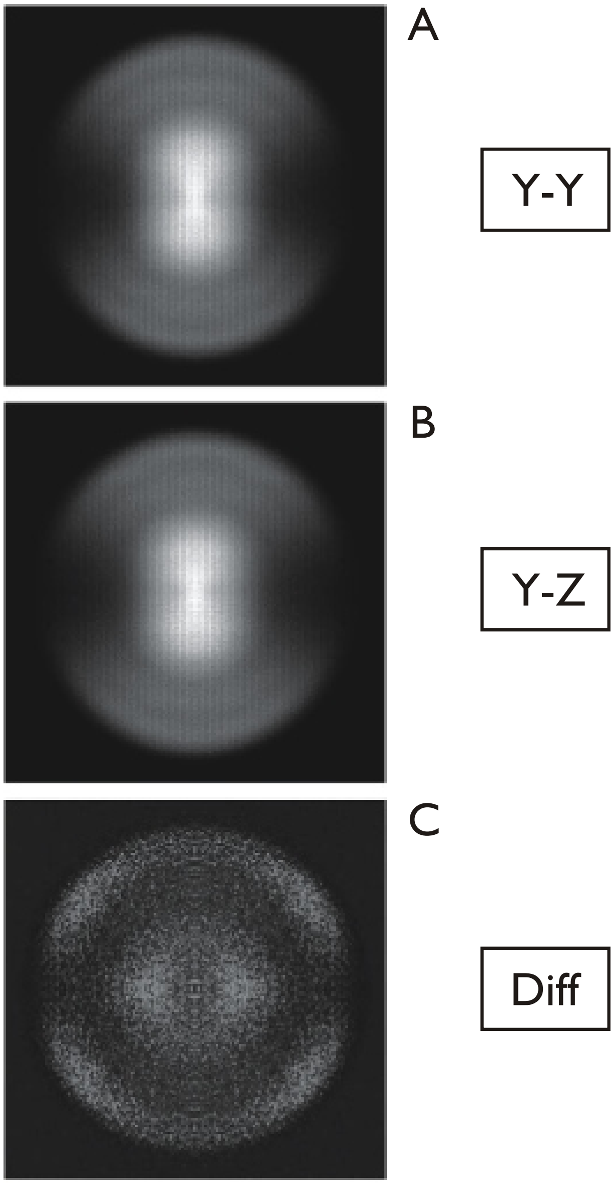

Figure 4.1: DC sliced images and difference image of S($^1D_2$) from 193.3 nm dissociation of ethylene sulfide for the indicated combination of photolysis-probe laser polarization directions. Note that the difference image C is not shown on the same intensity scale as images A and B.

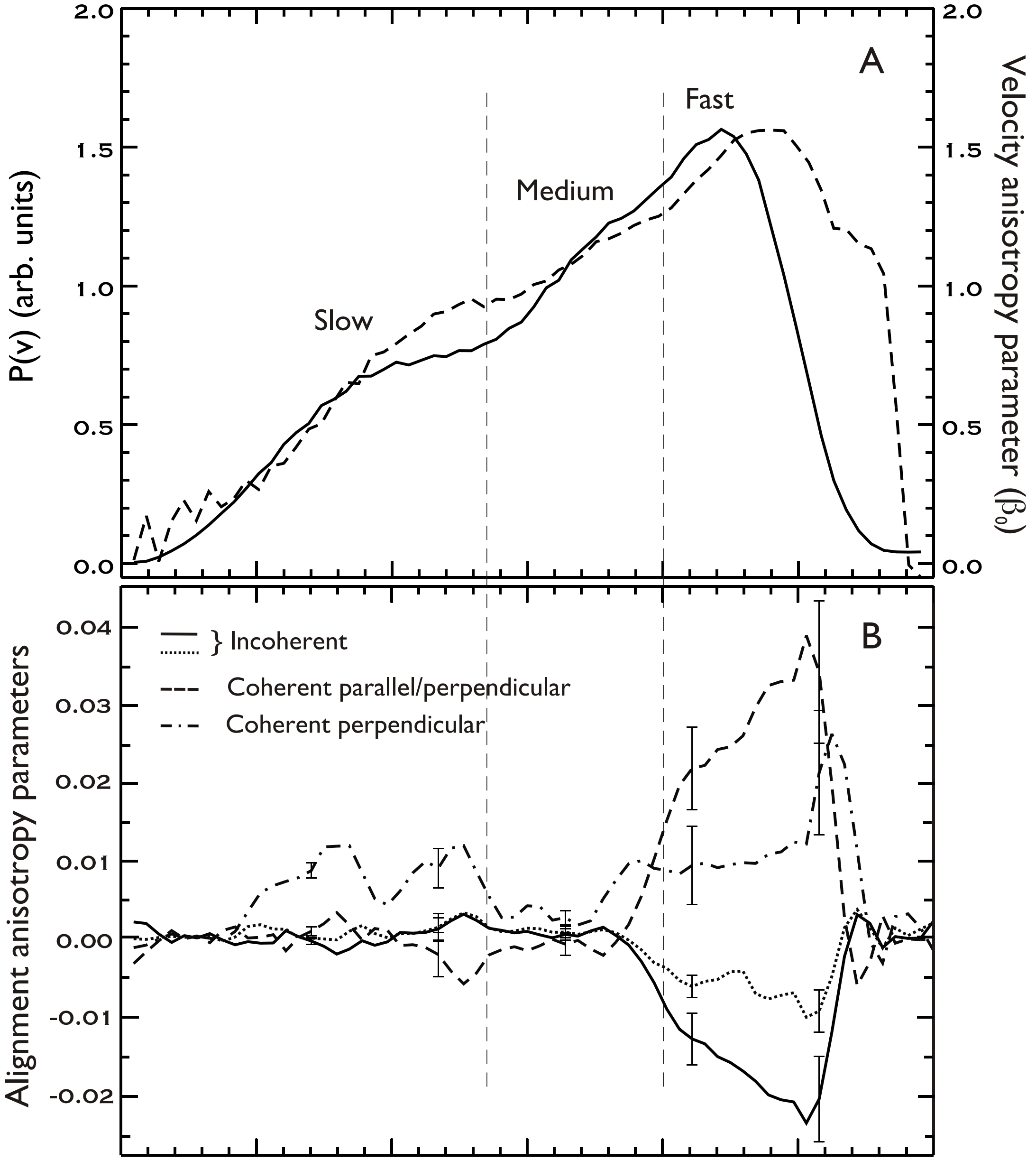

Figure 4.2: (A) S($^1D_2$) speed distribution (solid line) and recoil speed-dependent angular anisotropy parameter, β_0 (dashed line) for ethylene sulfide photodissociation at 193.3 nm. (B) Speed-dependent alignment contributions for S-atom arising from the following mechanisms: s_2 (solid line) and α_2 (dotted line) which together describe incoherent excitation, γ_2 (dashed line) which describes coherent parallel and perpendicular processes, and η_2 (dot-dashed line) which describes coherent perpendicular excitation.

A linear, singular value decomposition (SVD) fit[75] of Eq. 3.21 to the alignment image yields the recoil speed-dependent alignment anisotropy parameters corresponding to each different dissociation mechanism, which is plotted in Fig. 4.2 B. It is apparent that the alignment effects are clearly shown with distinct features in three speed regions correlating with the three dissociation channels shown in the speed distribution. For the slowest S($^1D_2$) fragments, the observed alignment results exclusively from a coherent perpendicular mechanism (η_2). The middle region, as would be expected from the image (Fig. 4.1 C), shows no alignment at all. For the fastest photofragments, the alignment is dominated by a coherent superposition of perpendicular and parallel processes (γ_2), concomitant with significant contributions from an incoherent perpendicular excitation (characterized by $s_2 \approx 2\alpha_2$) and from a coherent perpendicular mechanism (η_2).

The total alignment $\langle A_{20} \rangle$ can be determined by using the fitted alignment anisotropy parameters plotted in Fig. 4.2 B. In effect, $\langle A_{20} \rangle$ represents the total contribution of each alignment anisotropy parameter averaged over all recoil angles. Specifically, when the dissociation light is linearly polarized, the relevant relationship has been shown to be as follows:[17]

$$\langle A_{20} \rangle \;=\; -2\,(\alpha_2 \,+\, \gamma_2 \,+\, \eta_2) \tag{4.2}$$

It is found that $\langle A_{20} \rangle$ is around -0.02 for the slowest S-atom fragments, drops to zero for intermediate recoil speeds and then peaks at a value of -0.08 for the fastest fragments. The magnitude of the measured $\langle A_{20} \rangle$ and alignment anisotropy param-

Table 4.1: Limiting values for the alignment anisotropy parameters at three recoil speeds with corresponding values of β_0.

Parameter	Range		
	$\langle\beta_0\rangle = 0.7$	$\langle\beta_0\rangle = 1.1$	$\langle\beta_0\rangle = 1.4$
s_2	$-0.2 \cdots 0.2$	$-0.2 \cdots 0.2$	$-0.2 \cdots 0.2$
α_2	$-0.16 \cdots 0.16$	$-0.17 \cdots 0.17$	$-0.18 \cdots 0.18$
γ_2	$-0.21 \cdots 0.21$	$-0.19 \cdots 0.19$	$-0.17 \cdots 0.17$
η_2	$-0.13 \cdots 0.13$	$-0.09 \cdots 0.09$	$-0.06 \cdots 0.06$
$\langle A_{20}\rangle$	$-1.0 \cdots 1.0$	$-0.9 \cdots 0.9$	$-0.82 \cdots 0.82$

eters here must be in the range of the theoretical limiting values that are calculated assuming maximum orbital alignment of the atomic photofragments. These are presented for three recoil speed regions in Table 4.1. Comparing these limiting cases with the magnitude of the anisotropy parameters obtained from the experimental data, as shown in Fig. 4.2 B, it can be seen that the extent of the S-atom orbital alignment is less than only 10 % in this instance. Indeed, the size of the alignment effect is small, and thus, it can bring into question the reproducibility of data. However, repeated measurements of several data sets show the relative magnitude and spatial distribution of the intensity in the resulting difference images to be remarkably consistent. It indicates that the alignment presented here, although small, is a real and quantifiable effect and also demonstrates that the slice imaging approach can provide a highly sensitive probe of these small effects.

4.1.4 Discussion

The ethylene sulfide molecule in the ground state is highly symmetric (C_{2v} point group) and has a $(2b_1)^2(7a_1)^2(8a_1)^2(4b_2)^2(3b_1)^2$ electronic configuration, which is of

$^1A_1$ overall symmetry. The outermost 3b$_1$ orbital is almost completely non-bonding in character, and its main component is a 3p$_x$ orbital localized on the sulfur atom.[74] Note that the molecular frame $z-$axis taken to be the C_2 symmetry axis and the plane of the molecule is the yz plane. Carnell and Peyerimhoff observed a sharp peak in the absorption spectrum of ethylene sulfide at 192.2 nm and, based on MRCI calculations, assigned the peak to the promotion of an electron from this non-bonding orbital to a 4p$_x$ Rydberg orbital, making the transition to the excited state $^1A_1$ (in C_{2v} symmetry).[76] It is accepted that the photolysis at 193.3 nm arises predominantly through the same excitation, and that presumption was the basis of a previous discussion on the photochemistry of ethylene sulfide. That is, the observed trimodal translational energy distribution was interpreted as the result of subsequent internal conversion to two other nearby surfaces ($^1B_2$ and ground state) following the initial excitation to the $^1A_1$ state.[73] Fig. 4.3 displays the potential energy surfaces of ethylene sulfide in the C_{2v} symmetry calculated by Qi *et al.*.[73] It should be noted here that all three S($^1D_2$) exit channels in question produce the same electronic state of the C_2H_4 (^1A_g) co-fragment although there are large differences in the relative partitioning of the total available energy, $\langle E_{trans}\rangle/\langle E_{int}\rangle$, in each case.

It is important to point out significant features shown in Fig. 4.2. First, the recoil velocity anisotropy, β_0, exhibits a strongly increasing trend with increasing recoil speed and does not reach the value for the limiting parallel transition ($\beta_0 = 2.0$) at the highest speed. In the case of the fastest S-atom fragments ($\langle\beta_0\rangle \sim 1.4$), which arise from direct dissociation along the $^1A_1$ excited state, this deviation is probably a consequence of the rotation of the parent molecule through a small angle

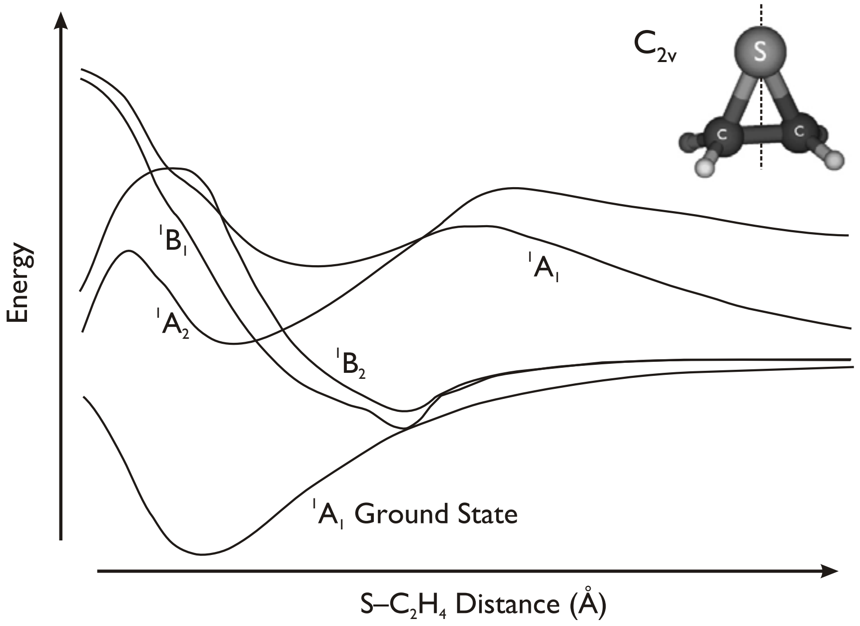

Figure 4.3: Schematic diagram of the singlet ethylene sulfide potential curves in the C_{2v} symmetry as a function of the S-C_2H_4 internulear distance, which is adapted from Ref.[73] and the structure of ethylene sulfide.

prior to the axial recoil along the C_2 axis *via* the simultaneous cleavage of the two C-S bonds.[70,71,73] The intermediate ($\langle\beta_0\rangle \sim 1.0$) and slow ($\langle\beta_0\rangle \sim 0.6$) fragments correlate with the dissociation on the $^1B_2$ and ground ($^1A_1$) states following internal conversion, respectively. The increased excitation of the internal degrees of freedom of ethylene sulfide as a consequence of relevant internal conversion could be a possible reason for the exaggerated deviation of β_0. As an alternative explanation for the observed β_0 trend, it can be speculated that the non-axial recoil arising from the sequential breaking of the C-S bonds also begins to play an increasingly important role. Although the coupling between the lower lying states and the excited $^1A_1$ state is considered not to be significant even in C_s symmetry,[73] it would also be plausible that the lower β_0 values, at least in part, are due to a distortion of the parent molecules arising from the coupling in the dissociation process.

Second, the alignment anisotropy parameters in Fig. 4.2 B show a clear S-atom recoil speed dependence, with notable contributions of coherent excitations. These effects indicate a small yet highly interesting contribution to the photolysis in ethylene sulfide. It suggests that the dissociation mechanism is considerably more complex than was previously thought since coherence effects imply the involvement of more than just a single potential surface in the initial excitation. A closer examination of the absorption spectrum of ethylene sulfide reported by Clark and Simpson[77] and also by Tokue *et al.*[74] reveals that, in addition to the strong Rydberg peak mentioned above, there are a series of additional peaks beginning at longer wavelengths. These have been assigned as vibrational progressions of the 4p$_z$ Rydberg orbital (B_1 overall transition symmetry) and, beginning at even longer wavelength, to a 4s Rydberg state (also B_1 symmetry overall).[76] Therefore, the transitions to those states are pure perpendicular, while the transition to the excited $^1A_1$ state considered as a dominant initial excitation is pure parallel (where here 'parallel' and 'perpendicular' refer to the direction of the transition dipole moment relative to the molecular symmetry axis). In particular, the 4p$_z$ B_1 state located in close vicinity of the $^1A_1$ state could be responsible for the alignment contribution arising from coherent parallel and perpendicular processes (i.e., simultaneous excitation of the 4p$_x$ and vibrationally excited 4p$_z$ states, as characterized by γ_2). Furthermore, the incoherent perpendicular contribution observed clearly for the faster S-atom fragments might be also attributed to the transition to the vibrationally excited 4p$_z$ state exclusively.

The η_2 alignment describing coherent perpendicular excitation is plainly shown, though weak, in the lower recoil speed region. This could be either a manifestation of degenerate states arising from the 4p$_z$ excitation or *via* interaction between the 4p$_z$ and even more highly vibrationally excited levels of the 4s Rydberg. Indeed, the fact that this slowest component is associated with the production of the most internally excited ethylene co-fragments would be consistent with this picture. In order to fully elucidate the importance of these proposed mechanisms for production of the coherent contributions, a detailed study of the wavelength dependence of the alignment would be required; at this point, the discussion is necessarily speculative in the absence of more investigation.

It is straightforward to reconstruct the S-atom electron charge clouds from the measured anisotropy parameters, as discussed in Chapter 3. The coherence contribution appears most clearly in the shape of the electron density at the recoil direction of 45°, showing the distribution with an azimuthal anisotropy. In this case, since the overall alignment is so small, I have chosen to plot only the *anisotropy* of the charge cloud in Fig. 4.4 rather than the total for highlighting the variation of the charge cloud with recoil angle and speed. Note that the electron charge cloud at the intermediate speeds was not displayed because of the negligible effects in that region, and the relative magnitude of the charge cloud anisotropy is not shown in this figure. As expected, the observed coherent effects give rise to a loss of cylindrical symmetry of the electron charge cloud at $\Theta = 45°$. The characteristic charge cloud anisotropy shows with varying recoil speed, which can be a dramatic effect revealing the large variation in the recoil-speed-dependent contribution to alignment.

One final issue to be considered is why the overall magnitude of the observed

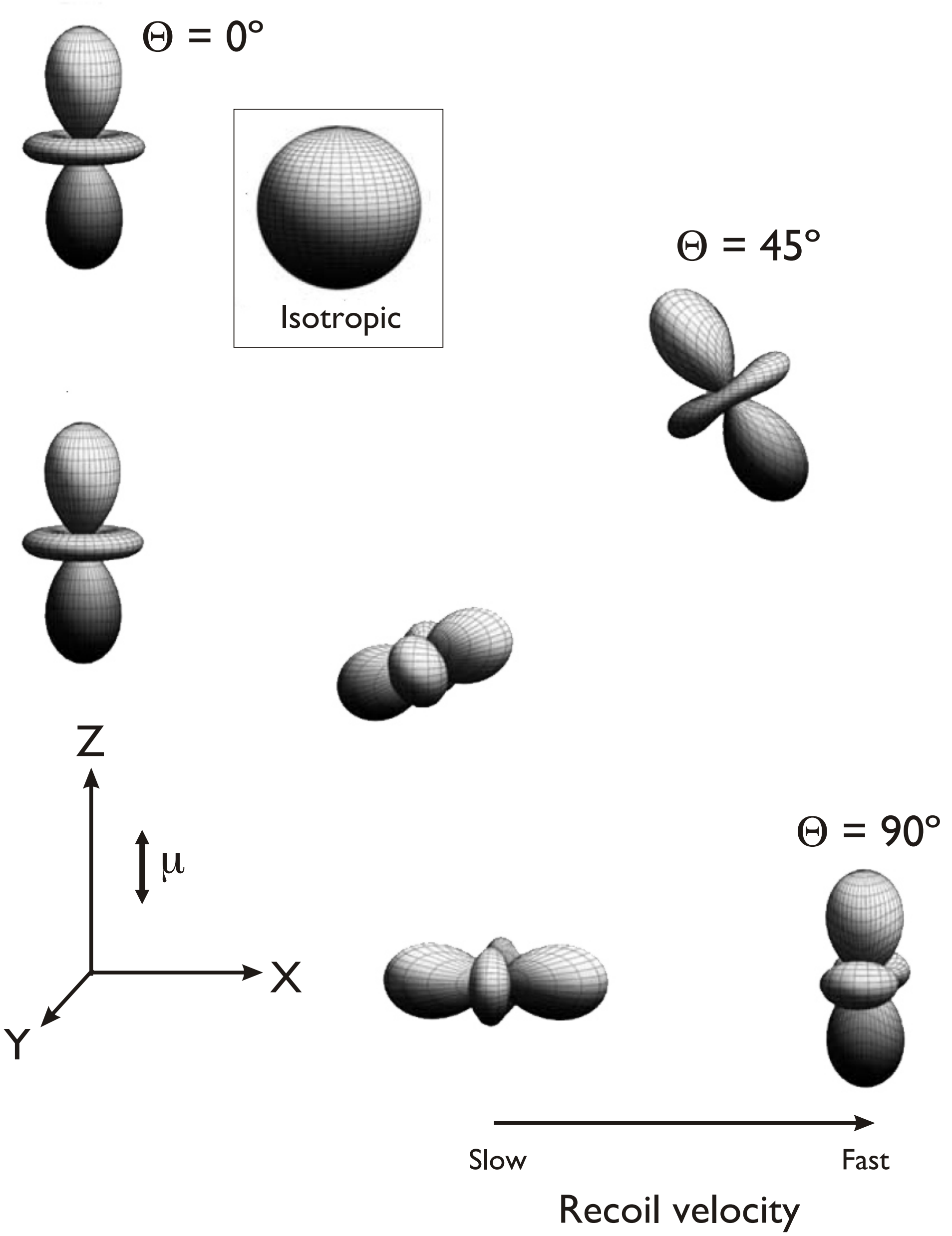

Figure 4.4: S($^1D_2$) charge cloud anisotropy obtained from the parameters extracted from the alignment image for two recoil speeds and three recoil directions. Note that the polarization of the photolysis light is directed along the Z-axis.

alignment is so small. Until a theoretical investigation is undertaken, this is a matter of pure conjecture; however, the highly constrained ring structure of the ethylene sulfide molecule raises some interesting questions. In a simple LCAO type description of the molecular orbitals in ethylene sulfide, the spatial geometry of the atomic orbitals localized on the sulfur atom within the three-membered C-S-C ring is very different from that in the free sulfur atom. The very rapid orbital relaxation might be expected to occur following photolysis, and that could possibly cause the depletion of any alignment that was initially present in the system. It will be illuminating to investigate this idea systematically by examining the orbital polarization that is observed for a series of related molecular species.

4.1.5 Conclusion

The analytical machinery that is developed to extract the absolute speed- and angle-dependent angular momentum polarization from the readily obtained DC sliced images has been applied to the vector correlation study of ethylene sulfide photodissociation at 193 nm. The speed-dependent recoil anisotropy and alignment anisotropy parameters were measured over a continuous range of photofragment recoil speeds. The apparent presence of coherent contributions to alignment suggests that the multi-surface excitation could be involved in the dissociation mechanism. Although the alignment effects are relatively small in this instance, DC slice imaging has been shown to provide a highly sensitive probe of such phenomena.

4.2 Ozone

4.2.1 Introduction

Despite its celebrated importance to life on earth, ozone photochemistry still remains a subject of surprising enigma. Although the dominant features of the photoabsorption in the ultraviolet spectral region and the ensuing chemistry have been long understood, there remain puzzles that elude definitive explanation: the mass independent heavy isotope enrichment in the stratosphere;[78,79] the vibrational structure seen in the Hartley and Huggins bands;[80,81] the varying bimodal vibrational distributions seen in the ground electronic state photolysis products;[82] and the variation in the vibrational distributions in the dominant excited state products throughout the UV.[83] Further investigations and alternative approaches are clearly needed. The use of ion imaging techniques to probe atomic orbital polarization in photodissociation[14,15,17,36–38,42] has recently emerged as one such alternative approach. These studies fundamentally deliver new insight into photochemical problems because they probe both the underlying features of the photoexcitation process as well as the subsequent dissociation dynamics across multiple electronic states. As such, these methods are ideally suited to studying ozone photochemistry, a system notorious for its electronic complexity. In this work, an application of DC slice imaging as a probe of atomic orbital orientation is presented for ozone dissociation at a series of wavelengths within the Hartley absorption band. The Hartley band extends from about 200 - 310 nm, and across most of this region photodissociation proceeds primarily via

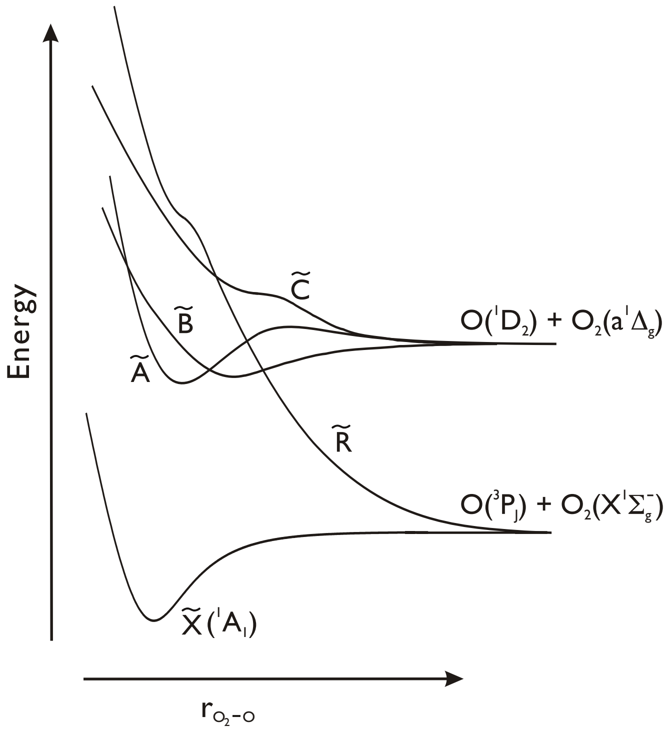

Figure 4.5: Schematic diagram of the O_3 potential curves relevant to the UV absorption region.

two pathways:

$$O_3(\tilde{X}\,^1A_1) \xrightarrow{h\nu} O_2(a\,^1\Delta_g) \;+\; O(^1D_2) \tag{4.3}$$

and

$$O_3(\tilde{X}\,^1A_1) \xrightarrow{h\nu} O_2(X\,^3\Sigma_g^-) \;+\; O(^3P_J) \tag{4.4}$$

The initial excitation is believed to take place directly to the $1\,^1B_2$ ($\tilde{\mathrm{B}}$)-state with about 90% of the population then dissociating on this surface to produce the $O(^1D_2)$ products.[83–86] Nonadiabatic crossing to the nearby $\tilde{\mathrm{R}}$-state results in roughly 10% yield of $O(^3P_J)$ atomic fragments.[87] This is illustrated schematically in Fig. 4.5.

Imaging studies of vector correlations in ozone photodissociation have a long history, largely in studies from the Houston group.[28,50,82,88,89] Dylewski *et al.* studied alignment effects in ozone across a significant portion of the Hartley band, applying both a "diagonal" treatment, in which coherences between different electronic states are neglected, and a fully quantum mechanical approach (only considering the rank $K = 2$ moment explicitly) where off-diagonal elements of the density matrix representing the photofragment alignment describe any coherent phenomena.[50] They concluded that at dissociation wavelengths of 255 and 298 nm, an incoherent parallel excitation mechanism dominates the alignment. This was consistent with previous assertions, based on theory, that the initial absorption and subsequent dissociation largely take place on the $1\,^1B_2$ surface. Their data also clearly revealed the contribution of a higher order $K = 4$ moment, however, suggesting additional contributions from other excitation or dissociation pathways. More recently, Hancock and co-workers[90,91] have reported significant alignment and orientation in the molecular $O_2(a\,^1\Delta_g)$ fragment produced in conjunction with $O(^1D_2)$ atoms, and this is seen to fluctuate with the product rotational state, perhaps a manifestation of the fascinating rotational-state dependent curve crossing reported by Valentini *et al.*[86] This observation of substantial rotational orientation is surprising and, to-date, lacking explanation.

4.2.2 Experiment

The key aspects of the experimental set-up employed in the DC slice imaging approach have been described in Chapter 2. Only the points specific to this particular study will be summarized here. Ozone was initially produced using a commercial generator (OREC) and retained in a silica gel trap held at −78°C in a dry ice/acetone bath. A molecular beam was then formed by raising the trap temperature to −40°C, flowing argon at about 730 Torr over the silica gel and expanding the resulting mixture through a 1 mm diameter pulsed nozzle. The photolysis laser light was generated using several different strategies: 266 nm was provided by the fourth harmonic of a Nd:YAG laser (Quanta Ray DCR-2A) operating at 10 Hz; 248 nm was produced by pumping a dye laser (Quanta Ray PDL 3, DCM dye) with the 532 nm output of the same YAG laser and then sum-frequency mixing with the residual 1064 nm fundamental; Longer wavelengths (275 nm) were simply generated directly from the doubled output of the 532 nm pumped dye laser (Rhodamine 560 dye). In all cases the power of the resulting beam was attenuated to approximately 1 mJ/pulse and then loosely focused into the interaction region using a 30 cm lens. Control over the polarization was achieved using either a fused silica Soleil-Babinet compensator (Special Optics) for cases where circular polarization was required or a double Fresnel rhomb in cases where linear polarization was required at 45°. The probe laser was provided by frequency tripling the output of a dye laser (Continuum Jaguar, Rhodamine 640 dye) pumped by the 532 nm harmonic of a second Nd:YAG laser (Quanta Ray GCR-5). A magnesium-fluoride Soleil-Babinet compensator (Karl Lambrecht) was used to produce the required circular polarization. The probe beam (~ 0.7 mJ/pulse) was then focused through a second 30 cm lens. The O($^1D_2$) atomic photofragments produced in the dissociation event were probed using the following (2+1) REMPI scheme:

$$\mathrm{O}\ 2p^4(^1D_2) \xrightarrow{2h\nu} \mathrm{O}\ 2p^3 3p(^1F_3) \xrightarrow{h\nu} \mathrm{O}^+ \qquad 203.7\,\mathrm{nm}$$

$$\xrightarrow{2h\nu} \mathrm{O}\ 2p^3 3p(^1P_1) \xrightarrow{h\nu} \mathrm{O}^+ \qquad 205.4\,\mathrm{nm} \tag{4.5}$$

Following ionization, the oxygen ions were accelerated through the multi-lens velocity mapping assembly and impacted upon a dual microchannel plate array of 120 mm diameter, which was coupled to a P-47 phosphor screen. In this particular instance a repeller electrode held at +700 V was used in conjunction with three additional focusing lenses in the velocity-mapping scheme to stretch the photofragment ion cloud along the time-of-flight axis to around 400 ns. The resulting image was recorded using a CCD camera (Mintron 2821e, 512 × 480 pixels) in conjunction with PC acquisition software (McLaren Research) that enabled real time event counting of the data.

4.2.3 Results

DC sliced images of ozone photodissociation at 266 nm were obtained using two different REMPI schemes (Fig. 4.6). In order to eliminate the population contribution and extract only alignment effects, two sliced images collected with different polarization geometries were used (see the details in Chapter 3). It is clearly seen that alignment images for different probe transitions each show quite different angular distribution from each other, implying that the angular modulations induced by the ionization process are distinctive. The four rings in each image correspond to $\nu = 0 \sim 3$ in the O_2 $(a^1\Delta_g)$ co-fragment. The difference image for the $^1D_2 \rightarrow\rightarrow {}^1F_3$ ionization scheme was analyzed to measure the alignment anisotropy parameters, containing dynamical information of photodissociation. In this instance, the rank

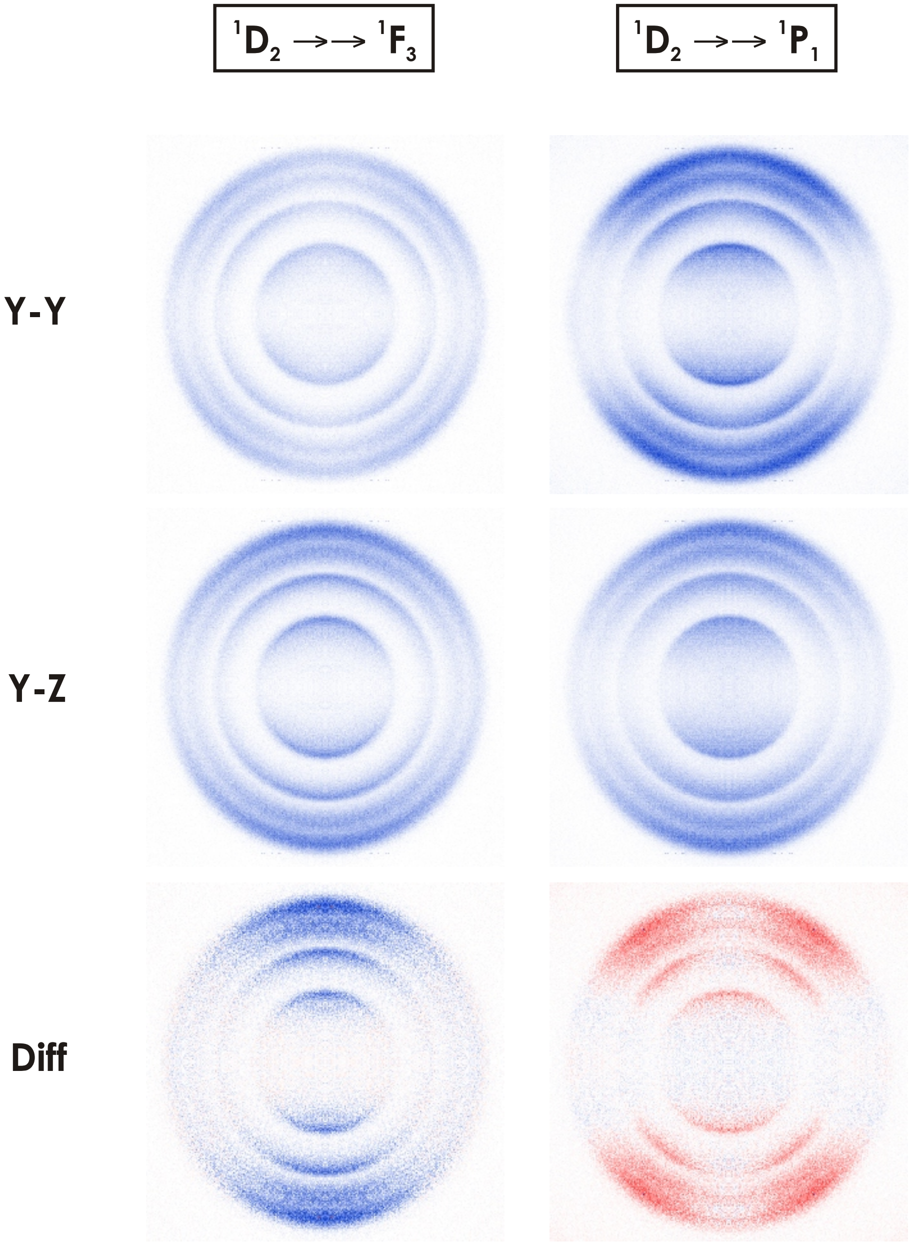

Figure 4.6: DC sliced and difference images of O($^1D_2$) from 266 nm dissociation of ozone for indicated combination of photolysis-probe laser polarization. The atoms were ionized *via* two REMPI transitions (203.7 and 205.4 nm). Red and blue correspond to positive and negative intensities, respectively.

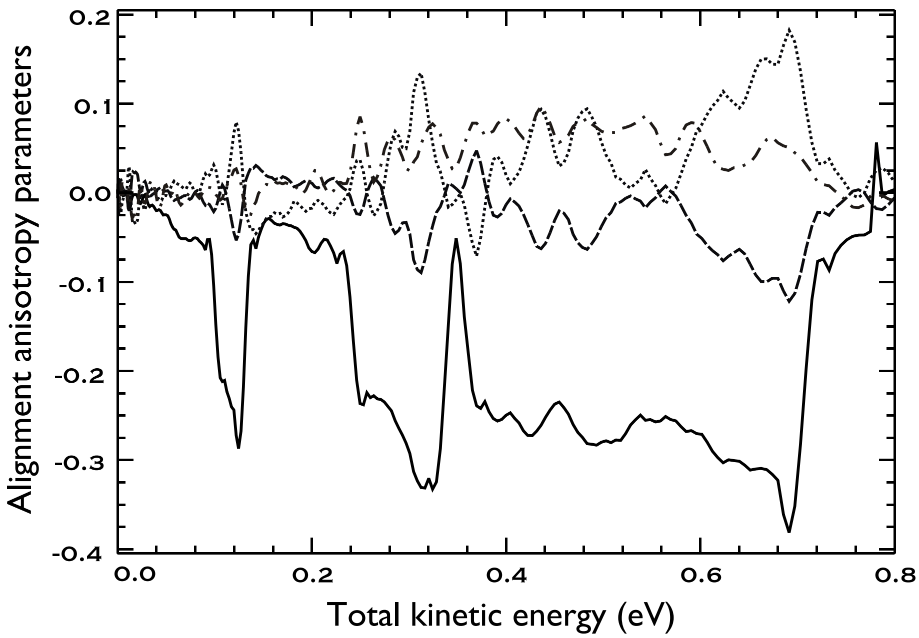

Figure 4.7: Speed-dependent Rank 2 alignment anisotropy parameters for O($^1D_2$) from ozone photodissociation at 266 nm. Incoherent parallel ($s_2 = -\alpha_2$, solid line), incoherent perpendicular ($s_2 = 2\alpha_2$, dashed line), coherent perpendicular/parallel (γ_2, dotted line), and coherent perpendicular (η_2, dot-dashed line).

$K = 2$ terms were included for an analyzing process, without the contributions of $K = 4$ terms. The fitted alignment anisotropy parameters are plotted as a function of the O atom recoil speed in Fig. 4.7. Significant alignment effects were observed and dominantly attributed to an incoherent parallel transition regardless of the recoil speed.

The orientation of oxygen atomic photofragments was determined by using a left and right circularly polarized probe light, and experimental images obtained at a photolysis wavelength of 266 nm are shown in Fig. 4.8. The dissociation laser was polarized either circularly or linearly at 45° with respect to the YZ plane, as indicated, in order to investigate the three possible atomic orientation effects, as described fully

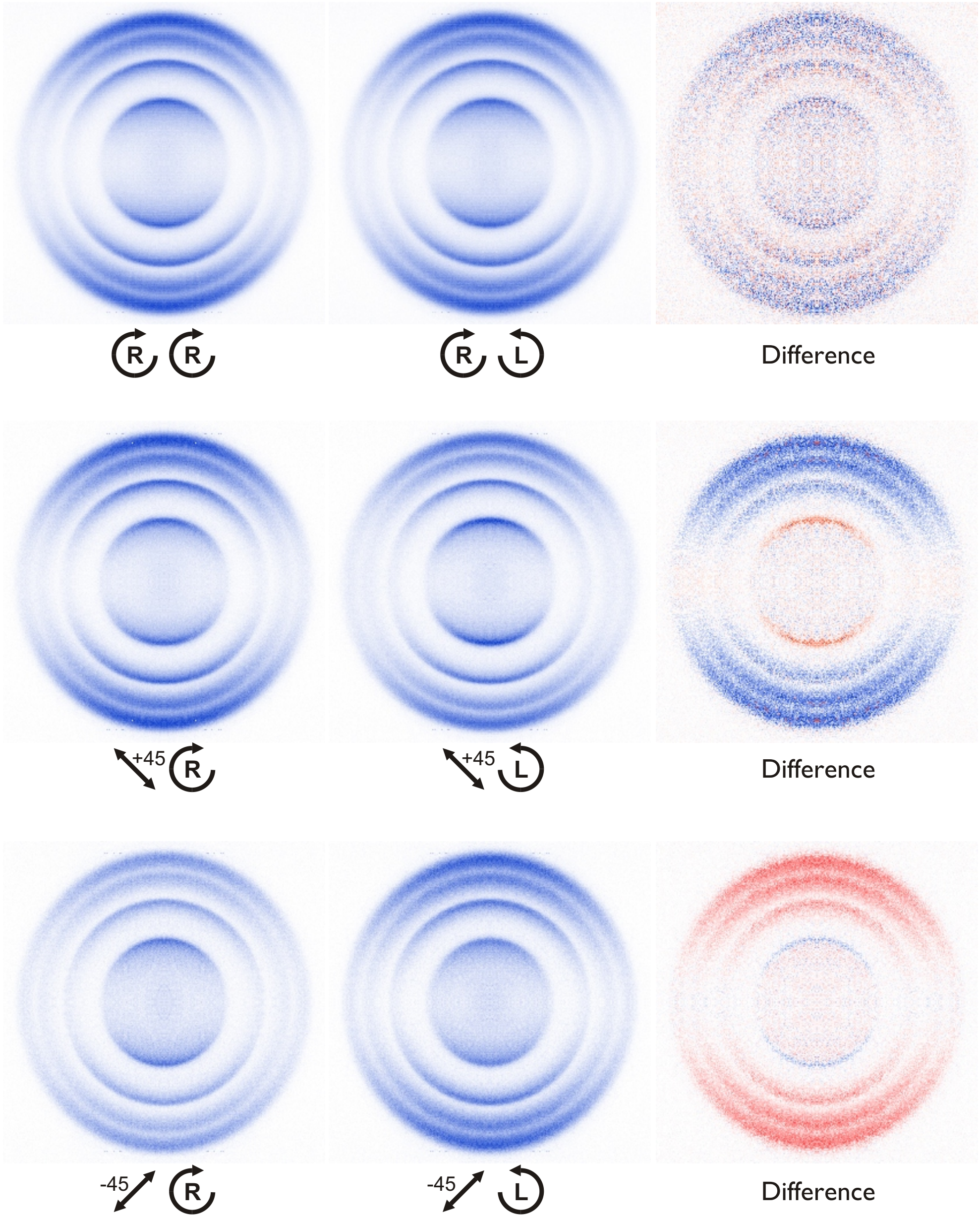

Figure 4.8: DC sliced and difference images of O($^1D_2$) from 266 nm dissociation of ozone for indicated combination of photolysis-probe laser polarization. Red and blue correspond to positive and negative intensities, respectively.

in Chapter 3. From the difference images and integration of the images (not shown), it is apparent that the values of the orientation anisotropy parameters (α_1, γ_1), obtained using circularly polarized photolysis light, are negligible within statistical error. For the case of 45° linearly polarized light, however, there is a significant orientation effect arising from a coherent parallel/perpendicular excitation (γ_1') that is strongly dependent upon the photofragment recoil speed. A particularly striking feature is the change in the sign of the innermost ring relative to the other three, which is confirmed by switching the direction of the photolysis polarization from $+45°$ to $-45°$, as shown.

In order to investigate the recoil speed dependence of γ_1' more closely, additional orientation measurements (using linear polarization at $+45°$) were carried out at various dissociation wavelengths ranging from 248 to 285 nm. The results are presented in Fig. 4.9. In general, a change of sign in the difference images for the slower fragments is consistently noted. This suggests that the sign and magnitude of γ_1' correlate most strongly with the O-atom recoil speed rather than the specific vibrational level of the O_2 co-fragment. In addition, some cases exhibit a change of sign of γ_1' within one ring (see Fig. 4.9, e.g., the $\nu = 0$ ring at 285 nm, the $\nu = 1$ ring at 280 nm and the innermost ring at 248 nm). This observation suggests that the correlation of γ_1' with co-fragment rotational levels may be an additional aspect of the dependence of the orientation effect on recoil speed.

The absolute $K = 1$ orientation anisotropy parameters can be obtained by fitting the difference images to the relevant Eq. (3.18) and Eq. (3.19), which include the correct normalization factor weighted by the recoil-dependent β for the sliced image. As described earlier, for the γ_1' case, it is also possible to directly measure the orienta-

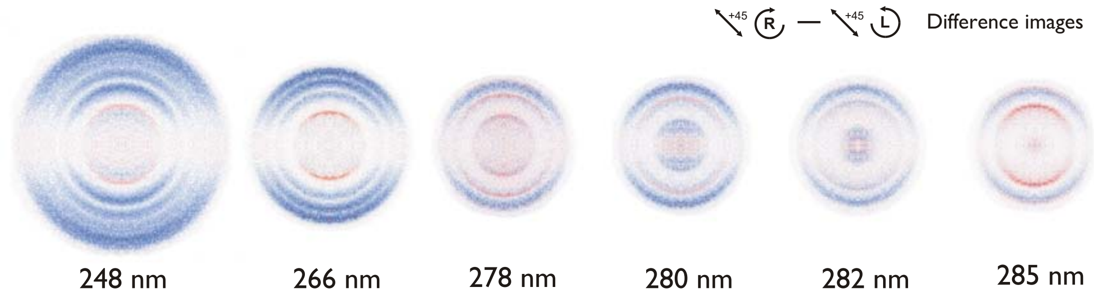

Figure 4.9: DC sliced difference images for the photodissociation of ozone at from 248 nm to 266 nm. Red and blue correspond to positive and negative intensities respectively.

tion parameter by just integrating the total intensity of the difference image at each recoil speed (Eq. (3.22)). With the latter approach, γ_1' may be determined directly from the experimental difference images and plotted as a function of O atom recoil speed, as shown in Fig. 4.10 for dissociation wavelengths of 248, 266, and 285 nm. Speed-dependent values for the recoil anisotropy parameter, β, were obtained by fitting the vertical-vertical (photolysis-probe polarization) image recorded using the O $(^1D_2) \rightarrow\rightarrow$ O $(^1F_3) \rightarrow$ O$^+$ REMPI probe transition at 203.7 nm, and neglecting the $K = 4$ contribution (which, as may be deduced from Eq. (3.17), is small in this instance). Peak γ_1' values for each vibrational level of the O_2 co-fragment are presented in Table 4.2 for all dissociation wavelengths studied.

From the speed-dependent orientation distributions plotted in Fig. 4.10, it can be seen that the peak of the orientation parameter does not generally occur at the peak of the population for each vibrational level. Instead, the maximum occurs at the slow side (corresponding to higher rotational states of the co-fragment) at each vibrational level except for the innermost ring. For the inner ring, where γ_1' changes

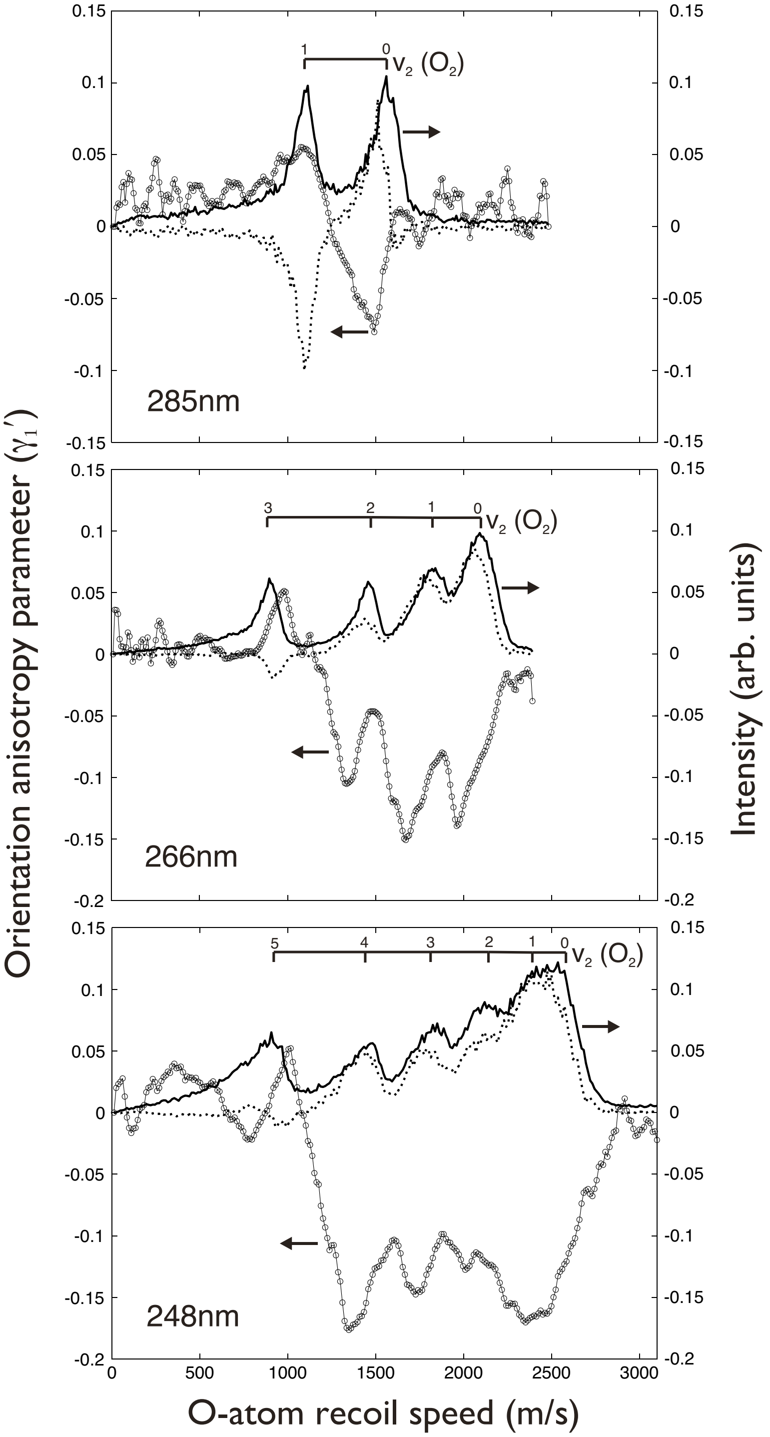

Figure 4.10: Orientation anisotropy parameter, γ_1', as a function of O-atom recoil speed following the photodissociation of ozone at 248, 266, and 285 nm. The solid line with the circle points denotes γ_1'. The solid and dotted lines correspond to the total population, $(\langle I_Z \rangle + \langle I_Y \rangle - \frac{1}{3}[\langle I_R^X \rangle + \langle I_L^X \rangle])$ and the difference signal, $(I_R^X - I_L^X)$, respectively. These values have been arbitrarily scaled.

Table 4.2: Variation in orientation anisotropy parameter, γ_1' with O_2 co-fragment vibrational level following the photodissociation of ozone in the region 248 nm ~ 266 nm.

Wavelength	$\nu = 0$	$\nu = 1$	$\nu = 2$	$\nu = 3$	$\nu = 4$	$\nu = 5$
248	-0.123	-0.167	-0.124	-0.148	-0.176	0.052
266	-0.139	-0.151	-0.105	0.051		
278	-0.090	0.006	0.015			
280	-0.137	-0.009	-0.029			
282	-0.102	-0.013				
285	-0.073	0.054				

sign, this dependence on the co-fragment rotational level is also inverted. That is, for the inner ring it is the lower rotational levels that have the largest magnitude of the orientation, and this occurs for rotational levels that are lower than the most probable levels for the given vibration. This behavior is consistently observed for other photolysis wavelengths even though it is not as clear at 248 nm, perhaps due to a complex overlapping in rotational structures.

4.2.4 Discussion

Results of ozone photodissociation at 266nm show a strong alignment caused by an incoherent parallel transition, consistent with earlier results from the Houston group.[50] Measured rank 2 alignment parameters can be employed to construct the electron charge cloud and photofragment density matrix for any recoil angles (see Fig. 15 in Ref.[66]). The charge cloud with cylindrical symmetry distribution along the breaking bond and the diagonal elements dominantly populated in $|m_J|$=0 indicate that the angular momentum vector is preferentially perpendicular to the recoil direction. However, as pointed out in the previous work,[50] the incompletion of the density matrix is suggested by the presence of negative elements, which may be due to neglecting the higher order terms ($K = 4$).

As already discussed in Chapter 3, the influence of the used probe step on the atomic alignment is substantial. Although the $K = 2$ moment has been considered as a most important contribution for alignment, higher moments may be required to characterize the underlying dynamics fully in some cases. The linestrength factors in Table 3.1 present that the sensitivity of the rank 4 terms for the ${}^1D_2 \rightarrow\rightarrow {}^1P_1$ transition is much higher than that for ${}^1D_2 \rightarrow\rightarrow {}^1F_3$. Therefore, the difference image produced using the 205.4 nm ionization scheme (Fig. 4.6) may reflect the angular variation caused by the contributions of the rank 4 moments, in contrast with the case of the 203.7 nm ionization. The peculiar difference image with four lobes for the 205.4 nm probe demonstrates that the contributions of the rank 4 moments could be important, and work is underway to extract the higher terms explicitly.

All three rank 1 orientation anisotropy parameters in the 266 nm photodissociation of ozone have been measured. The α_1 and γ_1 parameters, corresponding to incoherent perpendicular and coherent parallel/perpendicular excitation/dissociation mechanisms, respectively, are zero within the experimental uncertainties, while the dissociation mechanism represented by γ_1' shows a strong effect. Although γ_1' also reflects the coherent excitation of parallel and perpendicular transitions, it is quite different in origin from γ_1. The α_1 and γ_1 parameters arise, in effect, from propagation of the photon helicity into the product. The origin of γ_1', however, may simply reflect the simultaneous excitation of the different components of the transition dipole moment in the molecular frame. Therefore, it should not be surprising that the values of γ_1' and γ_1 are very different.

For the moment, we have no complete quantum mechanical theory of these phenomena and cannot give a full quantitative analysis; however, a qualitative explanation can be put forward based upon the following arguments. As already mentioned, the α_1 and γ_1 parameters directly reflect a mapping of the photon *helicity* $E_{10}(\mathbf{e})$[63] into the angular momentum distribution of the O-atom products. The components of the fragment angular momenta $j_{\parallel}$ and $j_{\perp}$ lie in the molecular plane parallel and perpendicular to the recoil axis, respectively (see Fig. 4.11). In fact, the condition for this orientation mechanism is *preservation* of the quantum number Ω (*helicity*) in the molecular excited state during dissociation. For a planar triatomic molecule this condition usually cannot be fulfilled. Let us consider the following expansion of the electronic molecular wavefunction over the basis set $|\Omega\,\rangle$:

$$\Psi_{mol} = \sum_{\Omega} A_{\Omega}\left(|\Omega\,\rangle \pm |-\Omega\,\rangle\right), \tag{4.6}$$

where Ω is the component of the total angular momentum projected onto the recoil axis.

The wavefunction Ψ_{mol} is either symmetric or antisymmetric under reflection of the electron coordinates in the molecular plane. The interaction between the basis states $|\Omega\,\rangle$ and $|-\Omega\,\rangle$ within the stationary wavefunction Ψ_{mol} in Eq. (4.6) results in the destruction of the *orientation* due to the population exchange between these states. Qualitatively, the rate of this interaction is proportional to the energy separation between the excited state and the nearest electronic states of the same

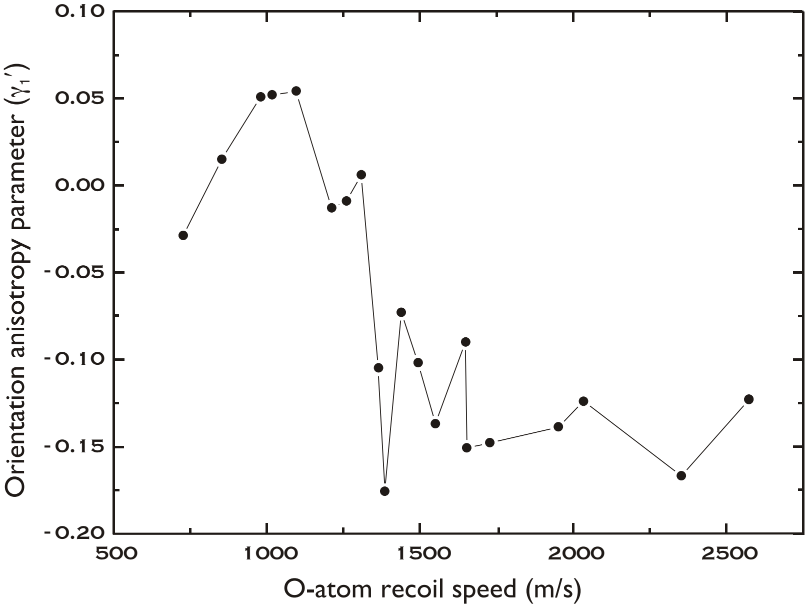

Figure 4.11: Recoil speed dependence of γ_1' for all O_2 co-fragment vibrational levels and all photolysis wavelengths.

symmetry, ΔE_e. Therefore, if ΔE_e is large compared with the inverse dissociation time τ_{diss}^{-1}, the quantum number Ω is not preserved and the orientation effect of the considered type (α_1 and γ_1), in general, cannot exist in planar molecules. An opposite case is met in diatomic molecules, where the interaction between $|\Omega\rangle$ and $|-\Omega\rangle$ basis states is usually caused by a rather weak Λ-doubling interaction. As a result, for fast dissociation $\Delta E_e \ll \tau_{diss}^{-1}$, and the fragment orientation due to the above mechanism is close to its maximum possible value, as reported elsewhere.[38, 64, 92]

The photofragment state multipole $\rho_{11}(\mathbf{k})$ described by the γ_1' parameter arises in a completely different way. As shown by Siebbeles and co-workers,[7] this state multipole arises as a direct tensor product of two alignments: $\rho_{11}(\mathbf{k}) \propto [Y_2(\mathbf{k}) \bigotimes E_2(\mathbf{e})]_{11}$, where $Y_{2q_1}(\mathbf{k})$ is the fragment recoil spherical harmonic and $E_{2q_2}(\mathbf{e})$ is the photolysis photon alignment. Note that the interaction between the basis states $|\Omega\rangle$ and $|-\Omega\rangle$, discussed above, does not affect the molecular *alignment.* The corresponding component of the fragment angular momenta $j'_\perp$ *is perpendicular to the molecular plane.* Therefore, the orientation characterized by the parameter γ'_1 should be expected for the polyatomic molecules in the absence of the Coriolis nonadiabatic interactions and in case the molecular planes possess alignment due to photodissociation.

The appearance of this coherent parallel/perpendicular contribution even in dissociation initiated on a single surface can be understood in light of related observations previously reported in NO_2.[31] In ozone excitation to the $\tilde{\mathrm{B}}$-state, the transition moment has B_2 symmetry within the C_{2v} point group and lies in the molecular plane at an angle $\theta = 31.6°$ with respect to the recoil axis. This gives rise to non-limiting β values even within the axial recoil approximation, and the transition moment possesses both parallel and perpendicular components in the recoil frame. This is a "static" coherence effect because the two pathways are degenerate and the initial phase difference between them is locked at a certain value during the initial excitation. In the previous study of NO_2, a similar coherent dissociation mechanism gave contributions to the alignment described by the γ_2 anisotropy parameter. In the case of orientation, the three anisotropy parameters described above should be considered in general. The parameter α_1 and γ_1 are proportional to $\cos\Delta\phi$, while the parameter γ'_1 is proportional to $\sin\Delta\phi$, where $\Delta\phi$ is the phase shift between the "parallel" and the "perpendicular" axes to the recoil direction.[27,64] In general, the phase shift contains a contribution from the nuclear movement which can be qualitatively associated with the elastic scattering phase shift and a "dynamical phase" (or Stokes phase, see[93]) contribution which is due to the optical electron excitation and the nonadiabatic interactions. The former contribution is known to give rise to the oscillation of the magnitudes of anisotropy parameters with photon wavelength;[27] it can likely be neglected in the "static" coherent case. However, the "dynamical" phase shift is nonzero, and in this experiment, results in the significant value of the γ_1' parameter.

Although this "static" coherence could account for the large γ_1', it cannot simply account for the profound speed dependence. This speed dependence is shown clearly in Fig. 4.11 in which the maximum magnitude of the γ_1' for each peak at all dissociation wavelengths has been plotted. Regardless of the photolysis wavelength or cofragment vibrational level, the value of γ_1' is generally small and positive for the slow fragments, and abruptly changes to large and negative for O atom recoil speeds of 1300 m/s or greater. Schinke has argued that photoexcitation in the Hartley-Huggins band system is exclusively to the $\tilde{\mathrm{B}}$-state but that curve crossings with the $\tilde{\mathrm{A}}$-state occur both at a very short range (not likely to be important in this case) and at a longer range (see Fig. 4.5).[87] Both the $\tilde{\mathrm{B}}$ and the $\tilde{\mathrm{A}}$-state encounter the $\tilde{\mathrm{R}}$-state subsequently, and there is additional opportunity for recrossing back. Furthermore, the $\tilde{\mathrm{A}}$ and $\tilde{\mathrm{B}}$-states correlate asymptotically to the same electronic states of the products, so coherences created in the initial excitation may well be preserved and give rise to interference following these curve crossings. More recently, Baloïtcha and Balint-Kurti calculated accurate potential energy surfaces of ozone with several avoided crossings.[94] They reported that there are three major curve crossings (i.e., $\tilde{\mathrm{B}}$-$\tilde{\mathrm{A}}$, $\tilde{\mathrm{A}}$-$\tilde{\mathrm{R}}$, and $\tilde{\mathrm{B}}$-$\tilde{\mathrm{R}}$) related to dissociation processes yielding asymptotic singlet products. Based on their diabatic and adiabatic potential energy surfaces, the probabilities of two possible pathways

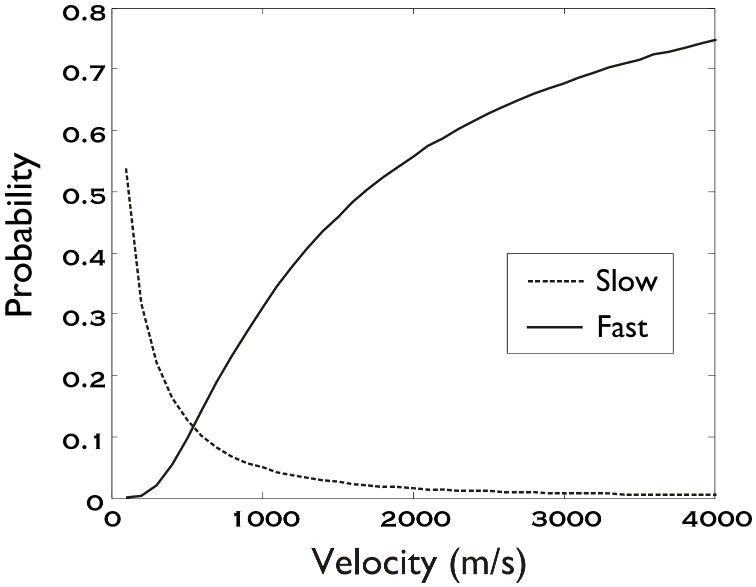

Figure 4.12: The probabilities of two possible pathways including three curve crossings, $\tilde{\mathrm{B}}$-$\tilde{\mathrm{A}}$, $\tilde{\mathrm{A}}$-$\tilde{\mathrm{R}}$, and $\tilde{\mathrm{B}}$-$\tilde{\mathrm{R}}$. One is the diabatic pathway, representing the dissociation along the $\tilde{\mathrm{B}}$ state exclusively (solid line); The other is the adiabatic pathway, in which the crossings to the $\tilde{\mathrm{A}}$ and $\tilde{\mathrm{R}}$ states, and subsequent crossing back to $\tilde{\mathrm{B}}$ state happen during dissociation (dashed line).

were evaluated as a function of velocity by using the Landau-Zener formula, which is displayed in Fig. 4.12. One pathway is the diabatic dissociation along the $\tilde{\mathrm{B}}$ state, and the other is the adiabatic dissociation crossing to the $\tilde{\mathrm{A}}$ and $\tilde{\mathrm{R}}$ states. The results show a substantial speed-dependence of the overall crossing probability consistent with the following interpretation: for the fast fragments, the diabatic pathway is dominant, while both adiabatic and diabatic pathways yield important contributions to the dissociation dynamics simultaneously for the slower fragments. Although this model could simplify the whole picture of the dynamics, it would provide a qualitative clue to explain the interesting speed-dependence of orientation. It is likely that smaller modulations are superimposed on these larger effects and associated with additional pathways and long-range nonadiabatic interactions. In fact, the abrupt change seen in Fig. 4.11 as a function of recoil speed is likely a consequence of "diabatic" dissociation on the $\tilde{\mathrm{B}}$-state giving rise to large magnitude orientation effects for higher recoil speeds, with "adiabatic" dissociation (i.e., crossing to the $\tilde{\mathrm{A}}$-state) quenching this effect at lower recoil speeds. Recently, studies of O($^1D_2$) orientation at the longer wavelengths ($\geq$ 298 nm) were reported by two groups in Oxford.[95,96] Orientation at 298 nm agreed well with that presented here at 285 nm. However, the negative values of γ_1' observed at the longer wavelength than 300 nm, even though those were speed averaged values, bring into question about the above simple model for the recoil speed dependence of orientation and imply that the other factors affecting orientation might be considered, as well as the contribution of curve crossings at the longer wavelength photolysis.

The change in sign of γ_1' for the slowest fragments and the related observation of the shift in the orientation peak from the population peak for each vibrational level provide further clues to the origin of the orientation. Since the latter observation persists in some form for all recoil speeds, to understand the effect we must look for a mechanism that would give a correlation between the co-fragment rotational level and atomic orientation. The static coherence mentioned above might exhibit this behavior since dissociation from more acute bond angles would be associated with greater perpendicular contributions, thus a larger parallel/perpendicular coherence, as well as with greater product rotational excitation. But if this were the principal mechanism, the coherence should closely track the β value since they both would find their origin in the deviation from the parallel limit. It does not. It should also be pointed out that, except for the innermost ring, the value of γ_1' is maximized for O-atoms formed in conjunction with O_2 in high rotational levels, and this general trend persists over all dissociation wavelengths studied. According to the analysis of the orientation parameter (Fig. 4.10), the orientation effect peaks in coincidence with much higher O_2 rotational levels than the most probable rotational state for a given vibrational level, and these already have a large J quantum number.[86] Assuming the simple impulsive model, one would expect that the smaller bond angle of ozone corresponds to the higher rotational excitation of O_2 fragments. An alternative explanation may be found by considering the dependence of the long-range potentials on the bond angle. Alignment measurements of $O(^1D_2)$ in N_2O photodissociation by Teule *et al.* showed that the atomic polarization is correlated with the rotational state of the N_2 co-fragment. They developed a semiclassical model taking into account the long-range quadrupole-quadrupole interaction that could account for this correlation.[34] A similar argument could account for the rotation correlation observed in ozone: i.e., it is a manifestation of the O-O-O bond angle mediating the long-range interactions. The recent study of ozone photodissociation at 193 nm showed that the orientation predicted by their model for the long range quadrupole-quadrupole interaction is quite consistent with the speed-averaged value of those reported here.[97]

In summary, the gross features of the speed-dependent orientation are a consequence of the static coherence persisting or being quenched at the avoided crossing between the $\tilde{\mathrm{B}}$ and $\tilde{\mathrm{A}}$- states. Superimposed upon these large effects are smaller modulations induced by the long-range interactions and by other nonadiabatic processes. Although dissociation start on a single potential surface and end in a single atomic state, the angular momentum polarization reveals that there would be the distinct paths during process. Additional theoretical investigation will be necessary to frame this interpretation in quantitative terms.

4.3 Carbonyl Sulfide

4.3.1 Introduction

Carbonyl sulfide (OCS) plays a key role in the atmospheric sulfur cycle,[98,99] and it has been an attractive target for studies of photodissociation dynamics, as well as other isoelectronic molecules CO_2, N_2O, and CS_2.[100–107] For photodissociation in the 220-250 nm region, it is well known that the excitation from ground state $(^1\Sigma^+)$ in the linear geometry is forbidden, while excitation of bent OCS is allowed for a transition to the excited states $1^1\Delta$ and $1\,^1\Sigma^1$. The former state becomes the $1\,^1A''$ state and the latter state splits into the $2\,^1A'$ and $2\,^1A''$ states in the bent geometry. These potential curves are illustrated schematically in Fig. 4.13. Suzuki and co-workers[100] reported that the excitations to the $2\,^1A'$ (parallel transition) and $^1A''$ (perpendicular transition) states are involved in the main dissociation processes via conical intersections with A', $A''(^1\Pi)$ states, ultimately leading to rotationally hot $\mathrm{CO}(X\ ^1\Sigma^+, \nu = 0, J) + \mathrm{S}(^1D_2)$ asymptotic products. They also attributed the slow S photofragments of a bimodal energy distribution to nonadiabatic crossing between the $2\,^1A'$ and the $1\,^1A'$ $(^1\Sigma^+)$ ground state. The photodissociation of OCS in the vacuum ultraviolet has also been examined, where more excited states are accessible, such as $(1\,^1\Pi \leftarrow\ ^1\Sigma^+)$ and $(2\,^1\Sigma^+ \leftarrow\ ^1\Sigma^+)$ transitions at ~ 166.7 nm and ~ 152.7 nm, respectively.[105,106] At 157nm, the dominant channel is $\mathrm{S}(^1S) + \mathrm{CO}(^1\Sigma^+)$, yielding vibrational resolved angular and energy distribution of CO fragments.[106]

Most previous studies of atomic orbital orientation and alignment have been carried out for OCS around 230 nm.[33,45,51,53] Recently, van den Brom *et al.* in-

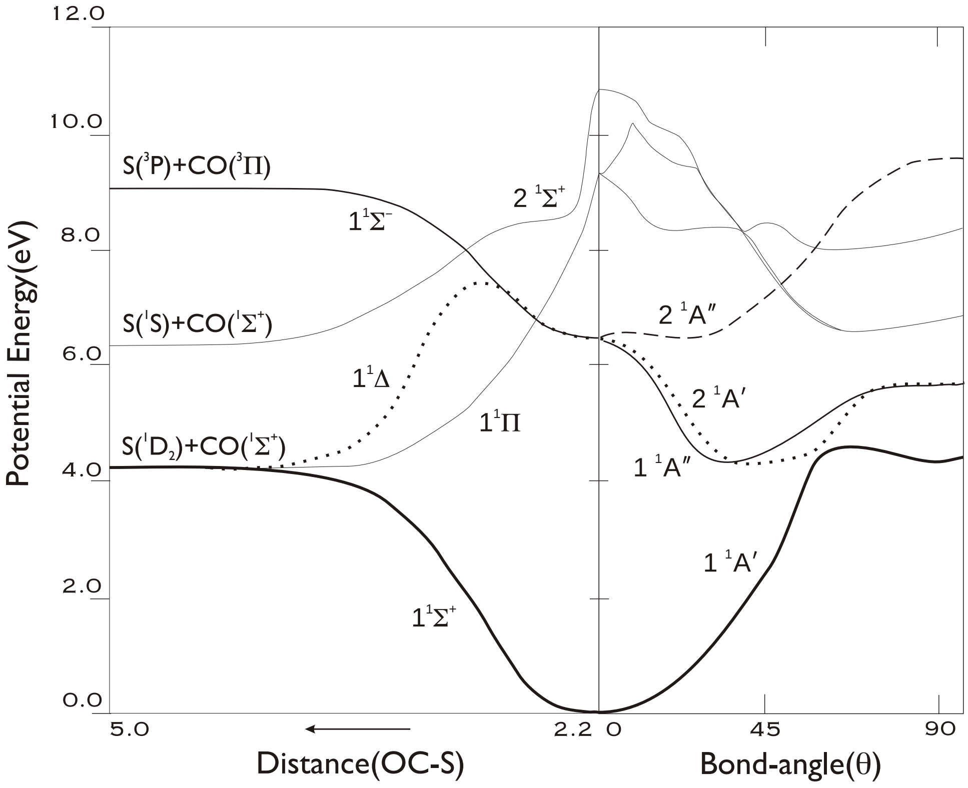

Figure 4.13: Schematic diagram of the OCS potential curves as a function of the OC-S bond angle and internulear distance adapted from Ref.[100]

vestigated orbital orientation of S($^1D_2$) photofragment produced from state-selected OCS ($\nu_2 = 0, 1|JlM$), observing the dependence of orientation on bending excitation at 230 nm.[45] They suggested that the contribution of the molecular frame polarization parameter Im[$a_1^{(1)}$] (defined as γ_1' in my formalism) mainly comes from the simultaneous excitation to two potential surfaces ($2\,^1A'$ and $1\,^1A''$), resulting in the phase shift between the scattering wave functions. Important recent developments in understanding OCS photochemistry have come from the Janssen group, who have used hexapole focusing to prepare laboratory-frame oriented, state-selected parent OCS molecules for photodissociation studies. Their work has provided insight into deviations from axial recoil, an issue examined in some detail below.

4.3.2 Experiment

The overall experimental set-up employed in the DC slice imaging approach has been described in Chapter 2 in detail, thus only the points specific to this particular study will be given here. A pulsed supersonic molecular beam of OCS seeded 10% in Ar is expanded into the source chamber and collimated by a skimmer. The photolysis laser light (193nm) was generated by an ArF excimer system running at 30Hz (GAM EX10/300). In order to produce the linearly polarized light, the laser output was first allowed to propagate through a total of eight fused silica window set at Brewster's angle before being focused into the interaction region using a 40 cm lens. Control over the polarization was achieved using a Berek's compensator (New Focus) for cases where circular polarization was required. The photolysis laser power was approximately 0.5 mJ/pulse. The probe laser was provided by frequency doubling the output of a dye laser (Rhodamine 610/590 dyes) pumped by the 532 nm harmonic of a second Nd:YAG laser (Quanta Ray PRO 290). A magnesium-fluoride Soleil-Babinet compensator (Karl Lambrecht) was used to produce the required circular polarization. The probe beam ($\sim$ 3 mJ/pulse) was then focused through a second 30 cm lens. The S($^1D_2$) atomic photofragments produced in the dissociation event were probed using the following two (2+1) REMPI schemes:

$$\begin{aligned} \mathrm{S}\ 3p^4(^1D_2) &\xrightarrow{2h\nu} \mathrm{S}\ 3p^3 4p(^1F_3) \xrightarrow{h\nu} \mathrm{S}^+ \qquad 288.18\,\mathrm{nm} \\ &\xrightarrow{2h\nu} \mathrm{S}\ 3p^3 4p(^1P_1) \xrightarrow{h\nu} \mathrm{S}^+ \qquad 291.47\,\mathrm{nm} \end{aligned} \tag{4.7}$$

Following ionization, the S-ions were accelerated through the multi-lens velocity mapping assembly and impacted upon a dual microchannel plate array of 75 mm diameter, which was coupled to a P-47 phosphor screen. In this particular instance a repeller electrode held at +700 V was used in conjunction with three additional focusing lenses in the velocity-mapping scheme to stretch the photofragment ion cloud along the time-of-flight axis to around 350 ns. The overall flight path from the laser interaction region to the detector was 100 cm. The resulting image was recorded using a CCD camera (Sony XC-ST50, 768 × 494 pixels) in conjunction with the IMACQ Megapixel acquisition program.[61]

4.3.3 Results

Experimental images obtained at a photolysis wavelength of 193 nm using two different REMPI transitions as a probing scheme are shown in Fig. 4.14. The Y-polarized dissociation laser was used with both Z- and Y-polarized probe, which corresponds to the Geometry IV case (defined in Chapter 3). For normalizing the data and improving measurement statistics, Geometry III measurements (Z-polarized photolysis) were also performed but the results are not shown here.

The resulting images show features not seen in previous studies around 230 nm, and some of this is owing to the higher resolution of the slicing approach, but more importantly owing to the different photolysis energy. In the faster fragments, there are three distinct rings which are likely associated with some specific groups of rotational states of the CO co-fragments, and these are labeled A-C. For the $^1D_2 \rightarrow\rightarrow {}^1F_3$

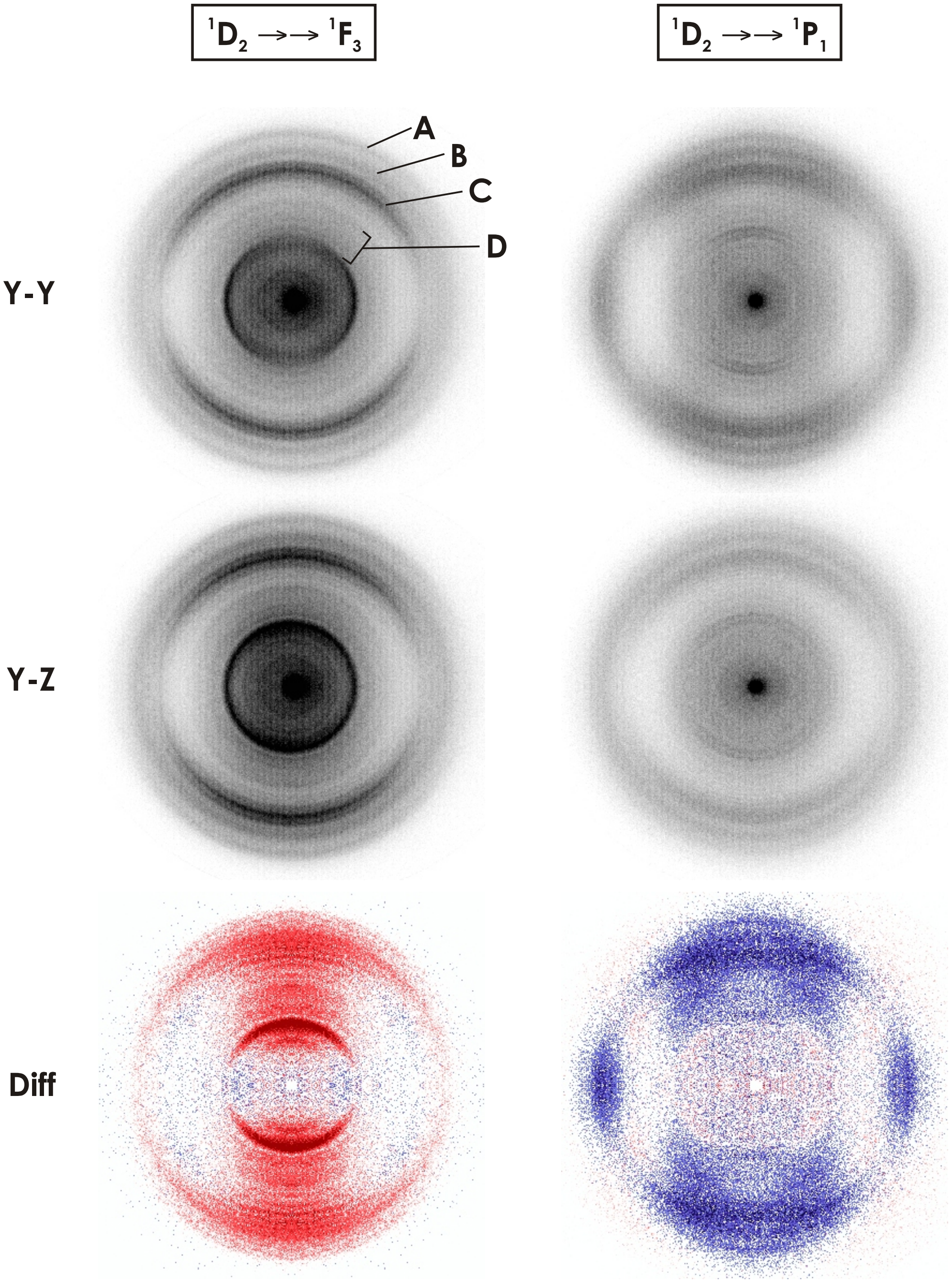

Figure 4.14: DC sliced and difference images of S($^1D_2$) in the photodissociation of OCS at 193 nm for indicated combination of photolysis-probe laser polarization. Red and blue correspond to positive and negative intensities, respectively.

REMPI probe transition, an intense inner ring comes from hot-band dissociation produced by the probe laser alone; this has been explicitly studied before.[107] Although a dilute sample was used to reduce this contribution, this signal from the $\nu_2 = 2$ bending state of the OCS parent molecule always exists but was omitted from our analysis. On the other hand, there is little one-laser signal in the $^1P_1$ REMPI transition owing to the difference in wavelength. A comparison of the angular distributions of the experimental images for the two geometry cases confirms that the relatively weak signals lying right beyond the one-laser signal (labeled the D region) are due to S fragments from 193 nm dissociation. The D region consists of several rings corresponding to resolved rotational structure of CO co-fragments. In particular, two distinct rings in the YY image with a probe wavelength at 291.47 nm (top-right in Fig. 4.14) show an energy spacing of ~0.028 eV.

Fig. 4.15 shows the total translational energy distribution and β parameter obtained from the YY image (top-left in Fig. 3). The comb above shows the rotational levels for the CO co-fragment in v=0 obtained using the dissociation energy D_0=25311 cm^{-1}, the excitation energy of S($^1D_2$), and the internal energy constants of CO (ω_0=2169.81 cm^{-1}, rotational constants B_0, D_0 from Ref.[103]). The peak of the A ring is assigned to $J \approx 76$ of the CO co-fragment in the ground vibrational level. The B and C rings are peaked at $J \approx 79$ and 84, respectively. The highest β parameter, (≈ 0.8), was observed in the C ring, while for the B ring the smallest value was measured, $\beta \approx 0.3$, which is the almost same as that obtained in the D ring. The A region photofragments show a slightly larger β value (≈ 0.4) than in the B ring.

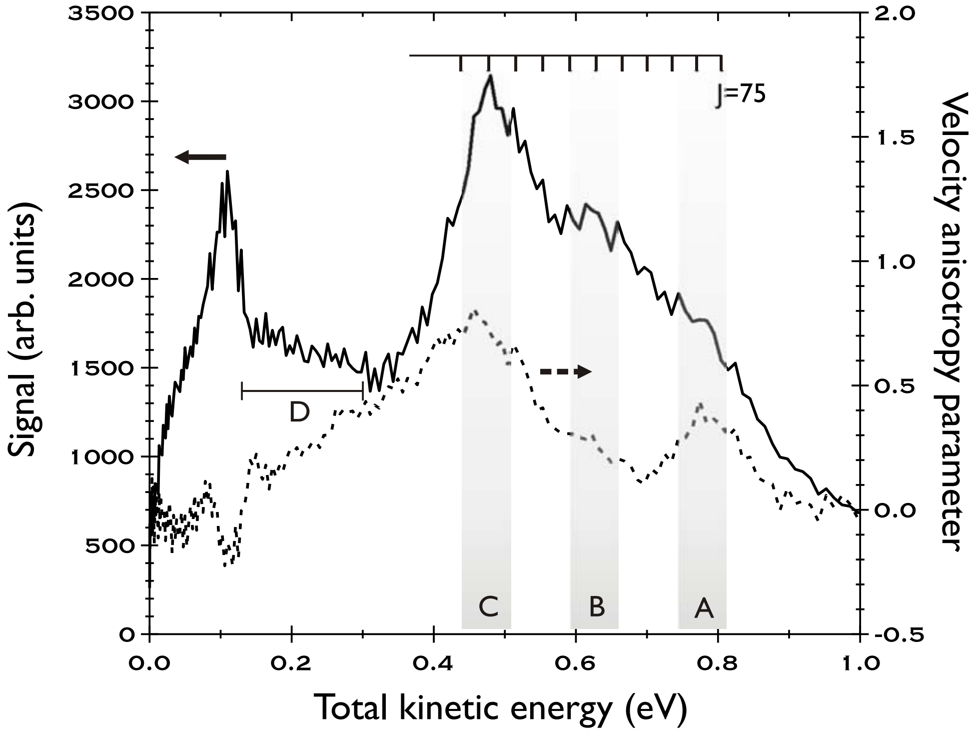

Figure 4.15: Total translational energy distribution (solid line) and corresponding recoil velocity anisotropy parameter, β (dashed line).

The rank 2 and 4 alignment anisotropy parameters are extracted by fitting the difference images to the relevant Eq. (3.20) and Eq. (3.21), including the correct normalization factor weighted by the recoil-dependent β for the sliced image. The fitting results are plotted as a function of S atom recoil speed in Fig. 4.16. The trend of s_2, α_2 alignment parameters indicates that over the whole range, an incoherent parallel transition (characterized by $s_2 \approx -\alpha_2$) is dominant but with a minor contribution from the perpendicular transition at some recoil regions. An interesting feature is the variation of the γ_2 parameter over the three rings, showing evidence that the dissociation dynamics in the C ring is distinct from that in other two rings. Comparing to the A and B rings, the fragments in the C ring have small negative γ_2

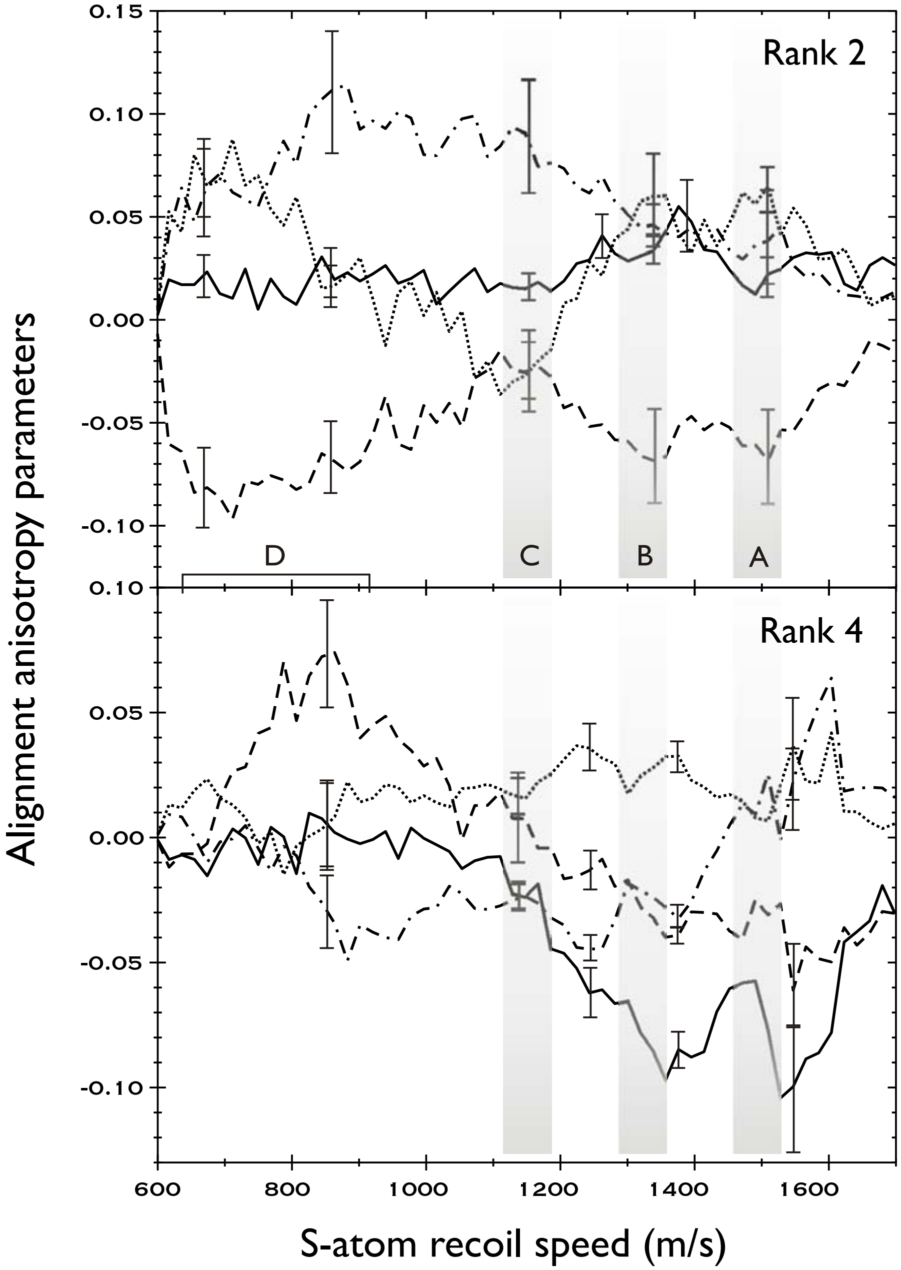

Figure 4.16: Speed-dependent alignment anisotropy parameters for O($^1D_2$) from OCS at 193 nm arising from the following mechanisms: s_K (dashed line) and α_K (dot-dashed line) which both describe incoherent excitation, γ_K (dotted line) and η_K (solid line) which are corresponding to coherent excitation (as discussed in the main text in detail). Three shadow bars denote the speed region where three distinct peaks are placed in images.

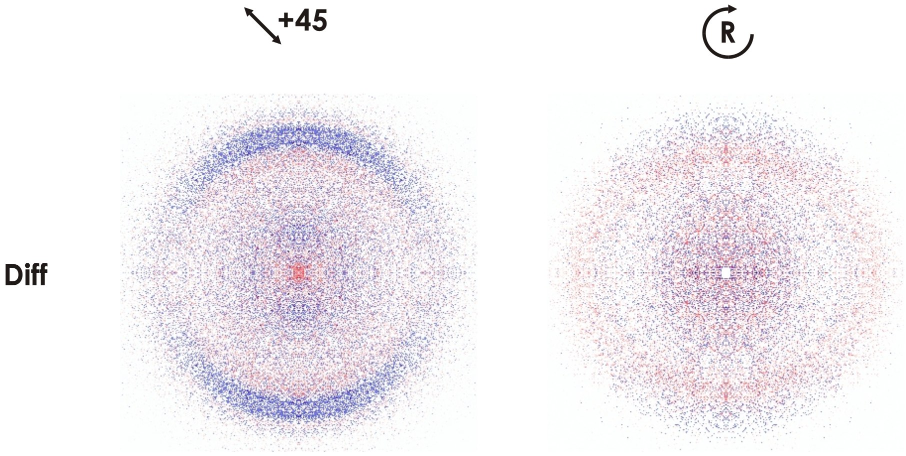

Figure 4.17: DC sliced difference images for indicated combination of photolysis-probe laser polarization measured via the ${}^1D_2 \rightarrow\rightarrow {}^1P_1$ REMPI transition. Red and blue correspond to positive and negative intensities respectively.

values representing a coherent parallel/perpendicular contribution. This strong recoil speed-dependence of γ_2 indicates that two different dynamics are likely contributing. Even though the size of the effect is small, a contribution of coherent perpendicular excitation described by η_2 exists around the B ring and especially in the outer edge of the A ring. The η_4 contribution is quite strong in the same region. That means two perpendicular transitions are involved in those regions.

In order to determine the three orientation parameters (α_K, γ_K, and γ'_K), right and left circularly-polarized probe light is used and the photolysis light is polarized either circularly or linearly at 45° with respect to the flight axis (Z-axis). The difference images are seen in Fig. 4.17 for REMPI detection via the ${}^1P_1$ intermediate, which is only sensitive to the rank 1 orientation contribution. The alternate REMPI scheme was used to determine the rank 3 parameters, which were found to be negligible within the uncertainty of the measurement. The recoil speed-dependent rank

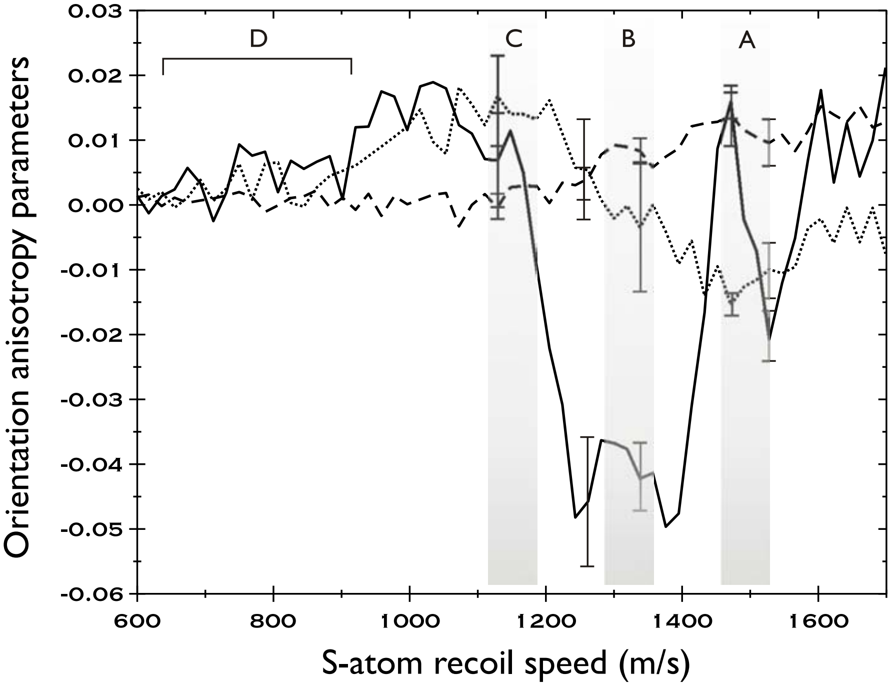

Figure 4.18: Speed-dependent orientation anisotropy parameters for O($^1D_2$) from OCS at 193 nm arising from the following mechanisms: α_1 (dashed line) representing incoherent perpendicular excitation, γ_1 (dotted line) and γ_1' (solid line) which describe coherent superposition parallel/perpendicular excitation. Three shadow bars denote the speed region where three distinct peaks are observed in the images.

1 orientation parameters are plotted in Fig. 4.18. One striking feature is the γ_1' contribution in the B ring arising from coherent parallel/perpendicular excitation. In addition to the dominant γ_1' orientation, there are small effects for γ_1 and almost zero for α_1. These are associated with transfer of the photon helicity into the photofragment. For nonlinear triatomic molecules, it has been suggested that the α_1 and γ_1 will typically be quenched in the dissociation process.[44]

4.3.4 Discussion

The previous studies of OCS photodissociation around 230 nm show bimodal translational and angular distributions related to two different dissociation dynamics: the slow channel arising from nonadiabatic transition from the $2\,^1A'$ to the ground state ($1\,^1A'$), and the fast channel resulting from a simultaneous excitation to two excited states ($2\,^1A'$ and $1\,^1A''$). As expected, the slower fragments had a large value of β due to a nearly pure parallel transition of the A' state, while the faster one showed a small or near-zero value implying the contribution from a pure perpendicular transition to the $1\,^1A''$ state. This interpretation was also supported by wave packet calculation of Suzuki and co-workers, displaying three distinct rotational distributions corresponding to different dissociation mechanisms: one from nonadiabatic crossing to the ground state from $2\,^1A'$, another from the adiabatic process along the $2\,^1A'$ state, and the third from the adiabatic process via the $1\,^1A''$ state.[100] However, the two adiabatic pathways were overlapped up in the experimental results at ~230 nm. These results from the longer wavelength photolysis can provide guidance to interpret the dissociation dynamics at 193 nm. First, the β value can give us the important clue on the symmetry of excited electronic states involved.

The large positive β in the C ring may indicate that the fragment is formed by dissociation from the A' excited state corresponding to a mostly parallel component of the transition dipole moment. On the other hand, the small β values in the B and A rings imply possibly that some perpendicular excitation is involved in those recoil speed regions, or there is greater bending in these regions. That is, the prominent lower value of β in the B ring may be ascribed to a multi-surface excitation in which the contribution of transition to A'' state (pure perpendicular) becomes significant. It should be pointed out here that although the A and B rings are attributed to the admixture of dissociation from two excited states, the contribution of the A'' state is larger in the B ring, accounting for the trend of the β parameter.

If the photolysis light is linearly polarized, the expression for the photofragments angular distribution $N(\Theta)$ can be presented in the following traditional form:[63]

$$N(\Theta) = \sqrt{2j_A + 1}\rho_{00}(\Theta) = \frac{1}{4\pi}\left[1 + \beta\, P_2(\cos\Theta)\right], \tag{4.8}$$

where Θ is the angle between the light polarization vector $\mathbf{e}$ and the recoil vector $\mathbf{k}$ and $P_2(\cos\Theta)$ is the Legandre polynomial of the second order.

If the photolysis light is circularly polarized, or unpolarized the result is

$$N(\Theta) \quad = \quad \frac{1}{4\pi}\left[1 - \frac{\beta}{2}\, P_2(\cos\Theta)\right], \tag{4.9}$$

where Θ is the angle between the direction of light propagation and the vector $\mathbf{k}$.

It has been known that the dissociation of OCS at 230 nm gives rise to non-axial recoil dynamics even though the β value of $\sim$1.8 was observed at CO ($N = 62$) fragment corresponding to the slow channel.[108] Recently, a quantum mechanical study of the non-axial recoil problem was reported for the photodissociation of a diatomic-like molecule by Kuznetsov and Vasyutinskii using the quasiclassical approximation.[13] The main result of this work is that, neglecting Coriolis mixing, the rotation of the

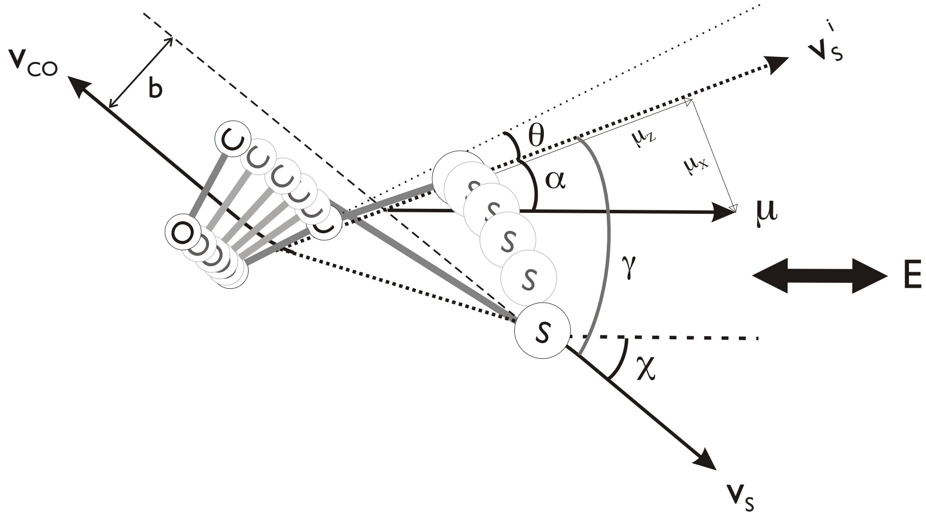

Figure 4.19: Illustration for the geometry of OCS at the initial excitation to the $2\,^1A'$ excited state and during dissociation. α is the angle between the transition dipole moment ($\boldsymbol{\mu}$) and the initial recoil velocity ($\mathbf{v}_S^i$) at Jacobi angle θ and χ can be measured from the experimental result. (see the text in detail)

molecular axis during dissociation can be described by a number of *rotation factors* which depend on the rank of the incident photon polarization matrix, on dissociation mechanism, and on the classical angle of rotation of the recoil axis γ. Also, each experimentally determined anisotropy parameter of the rank $K \geq 0$ can be presented as product of the corresponding *rotation factor* and the "axial recoil" anisotropy parameter.

However, the result of Kuznetsov and Vasyutinskii cannot be directly applied to the photodissociation of a rapidly rotating planar triatomic molecule with the transition dipole moment in the molecular plane, schematically shown in Fig. 4.19. In this figure, the angle α between the transition dipole moment $\boldsymbol{\mu}$ and the initial recoil direction is always in plane with the angle of rotation of the recoil axis γ. As mentioned in Chapter 1, the parameter β is presented as

$$\beta = 2P_2(\cos\chi), \tag{4.10}$$

In this case, $\chi = \alpha + \gamma$ is the angle between the transition dipole moment $\boldsymbol{\mu}$ and the recoil direction $\mathbf{v}_s$ in Fig. 4.19.

Eq. (4.10) derived using a quantum mechanical approach perfectly agrees with the result of classical treatment of the photodissociation of planar molecules.[12] According to the transition dipole moment calculation of Suzuki *et al.*, the angle between the transition dipole moment and the initial recoil direction is about $-20°$ (α) at a Jacobi angle (θ) of $\sim 7°$ for the single excitation to $2\,A'$ state. As mentioned previously, the transition dipole moment of the A' state does have a component in the molecular plane perpendicular to the recoil direction which could be the reason for showing a lower β than the limiting value of 2 even for pure axial recoil. The value of α might be changed during dissociation process depending on the change of the Jacobi angle. Using Eq. (4.10), the angle χ was determined from our experimental result ($\beta \approx 0.8$), giving $\chi \approx 39°$. With the values of χ and α, the angle γ of $\sim 59°$ is estimated. This suggests that the initial recoil velocity passes through $\boldsymbol{\mu}$ by great bending and rotational motion of the parent molecule and ends at the final recoil direction with a certain transverse recoil angle. The comparison with the dissociation process at 230 nm, where the angle χ of $\sim 13°$ was measured, implies that the larger deflection corresponding to the angle γ probably occurs at 193 nm than 230 nm. In other words, a strong bending motion could be involved prior to C-S stretching at

193 nm to cause a larger deflection than in the 230 nm case.

Assuming dissociation from a parent molecule in $J = 0$, the impact parameter (b) can readily be determined from the relative recoil velocity and rotational excitation in the CO fragment ($J = 84$) using the well-known classical formula, $L = \mu v b$. It is calculated to be about 1.4 Å(shown in Fig. 4.19), which is smaller than that ($b \approx 2.4$ Å) at 230 nm photolysis. The large impact parameter associated with a high β value at the longer wavelength is rather puzzling, and may reflect much lower impulsive recoil relative to bending motion than at 193 nm. However, this is difficult to reconcile with the χ values discussed above.

Given the present development of the theory, the terms containing the angle of rotation γ cannot be isolated from the expressions for the $K > 0$ anisotropy parameters for rotation of a planar molecule and therefore, the axial recoil anisotropy parameters cannot be determined. However, the general expressions in Eqs. (3.18)-(3.21) describing the experimental signals are still valid for the case of non-axial recoil of a planar molecule if the anisotropy parameters s_k, α_k, γ_k, and η_k are assumed to be a function of γ. In this case, the alignment and orientation anisotropy parameters can still give us valuable insight into dissociation dynamics. The most important feature of the B ring is the obvious γ'_1 (coherent parallel and perpendicular excitation) contribution in that ring. It supports the view that dissociation in this region also involves excitation to the A'' state. As mentioned previously, the very different feature of γ_2 in the C ring indicates that fragments in the C ring might be produced via very different dynamics than the other rings. Furthermore, the smaller value of γ_2 relative to that in the A and B rings tells us that the coherent contribution is very small in the C ring. In other words, while the A and B rings are likely related to simultaneous excitation to both $2\,^1A'$ and $1\,^1A''$ states, the C ring is most likely to arise from single-surface ($2\,^1A'$) excitation. The observation of η corresponding to a coherent perpendicular dissociation mechanism possibly suggests a coherent superposition of the pure perpendicular transition to the $1\,^1A''$ state and the possible small perpendicular component of $2\,^1A'$ transition. However, it is less plausible to explain the η_4 alignment effect above the A ring with the same reason, since it is known experimentally and theoretically that the contribution from $1\,^1A''$ is associated with higher rotational levels than from $2\,^1A'$. The potential energy surface in the bent geometry (shown in Fig. 4.13) shows that there is another possible state ($2\,^1A''$) to be considered in the dissociation at 193 nm case. Although the $2\,^1A''$ state has been ignored as out of reach ($\approx$ 6.2 eV) in earlier studies, at 193 nm (6.42 eV) it may be accessible, and the oscillator strength of this transition is almost same as for $1\,^1A''$ state. In addition, the fact that both $\eta_{2,4}$ in the C ring are nearly zero makes it more convincing that a nonadiabatic interaction following single-surface excitation is involved in the dissociation process.

For dissociation at 223 nm, the CO rotational distribution is peaked at $J =$ 55 and 67 for the faster and slower fragments, respectively.[100] Assuming that the efficiency of conversion of bending motion into CO rotation during the nonadiabatic transition is constant regardless of photolysis photon energy, one can easily expect $J = 85$ for the slower fragments in this case. This simple argument makes it reasonable that S fragments in the C ring ($J = 84$) may arise from dissociation initiated on the $2\,^1A'$ state followed by a nonadiabatic crossing to the ground state, which is also consistent with the above interpretation for observed orientation and alignment

Table 4.3: Measured alignment and orientation parameters for S($^1D_2$) from 193 nm dissociation of OCS.

Parameter	Region C	Region B[a]	Region A[a]
β	0.8	0.3	0.4
α_1	0.00	0.01	0.01
γ_1	0.02	0.00	-0.02
γ_1'	0.01	-0.04	0.02
s_2	-0.03	-0.06	-0.06
α_2	0.08	0.05	0.04
γ_2	-0.02	0.05	0.06
η_2	0.01	0.03	0.02
s_4		-0.04	-0.06
α_4		-0.03	0.03
γ_4		0.03	0.04
η_4		-0.09	-0.11

[a] Reported rank 4 anisotropy parameters are obtained at $\sim 50\ m/s$ faster velocity region.

parameters. All measured alignment and orientation parameters are summarized in Table 4.3.

As mentioned previously, wave packet calculations showed three distinct rotational distributions. Although the contributions of two adiabatic pathways via each $2\,^1A'$ or A'' state were not resolved experimentally at ~230 nm photolysis, it is perhaps not surprising that the separation in energy between two pathways is clearer in the present results, both owing to the higher resolution of DC slice imaging and the greater available energy following 193 nm dissociation. Results also suggest that the nonadiabatic transition (peak C) has a stronger contribution relative to other dissociation dynamics processes at 193 nm in contrast with previous results at the longer photolysis wavelengths. It is known that the probability of nonadiabatic crossing is larger as the photolysis energy increases owing to the greater possibility for reaching to the $1\,^1A''$ excited state which lies higher in energy than $1\,^1A'$ state. In addition, the Landau-Zener picture can also account for the larger probability of nonadiabatic transition. In this picture, the probability of nonadiabatic crossing is proportional to the recoil velocity and the difference in slopes of the two diabatic potential surfaces at the crossing point. The recoil speed of the S fragments at the nonadiabatic avoided crossing region is about 1150 m/s, which are faster than (~780 m/s) at 223 nm by Suzuki and co-workers.[100] That is, the diabatic pathway is more probable than the adiabatic pathway at the shorter wavelength, which could be reflected in the increased signal level in the C ring.

Some features in the D region show resolved rotational structure of CO as described previously. The energy spacing of well-separated rings (~0.028 eV) gives us a hint for rotational states of CO in this region. Using the rotational constant (B_0) and vibration-rotation interaction constant (α), a vibrationally dependent rotation constant was estimated to assign those rings to $J = 63 - 64$ rotational levels in $\nu = 4$ excited vibrational state. The structure in the D region thus implies that some contribution of highly vibrationally excited CO co-fragments possibly underlies the main rings of CO in the ground vibrational state. Although most results of OCS photodissociation at 223 nm and longer wavelength report that the vibrational excitation of CO is negligible,[100,109] it appears that some vibrationally-excited CO are produced at 193 nm, given much greater available energy and possible access to other excited states.

For the first time, the full molecular frame sulfur atom density matrix was constructed by using all measured anisotropy parameters. The complete density matrices

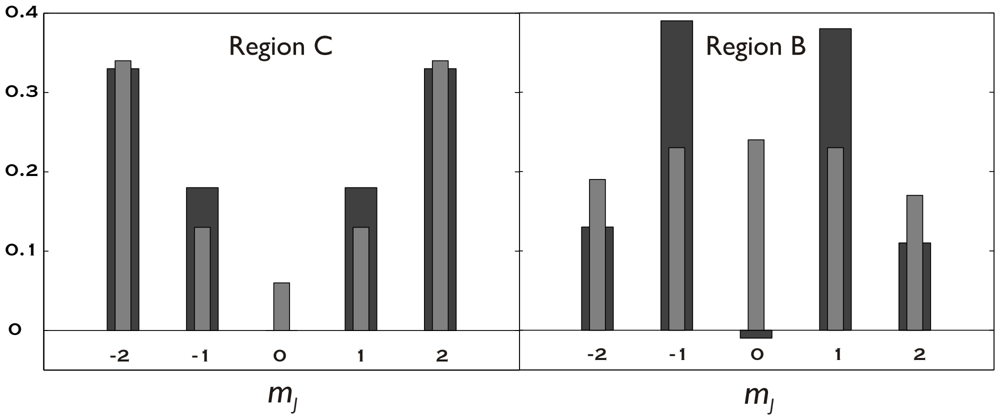

Figure 4.20: The population of each magnetic sublevel for S ($^1D_2$) atom at the recoil angle of 0° for the fragments in the region C (top) and region B (bottom). A wide darker bar corresponds to the complete density matrix, and a narrow lighter bar indicates the density matrix calculated excluding the rank 4 contributions. The uncertainty in the determination of these populations is typically less than ±0.04 based on reproducibility over several measurements.

are reported here for recoil angles of $0°, 45°$ and $90°$ in the circularly-polarized dissociation light case. Fig. 4.20 displays the diagonal elements of density matrices for the photofragments in the C and B rings recoiling along the polarization of photolysis light. In the C ring, it is apparent that **v** is parallel to **J** for either case with or without the higher order $K = 4$ contributions. On the other hand, for the density matrix in the B ring these are surprisingly different from one another. This means that the hexadecapole moment ($K = 4$) of the angular momentum distribution is particularly important in this recoil region and must be considered to obtain the complete density matrix accurately. The distribution of the $|m_J|$ population is peaked at $|m_J|$=1 with an additional small orientation toward $m_J = -1$ level. It is noted that there is a physically impossible negative element in the $m_J = 0$ sublevel, implying that the rank 4 contributions might be slightly overestimated. For the B ring, the full density matrices for recoil angles of 45° and 90° including all rank $K = 0 \sim 4$ contributions are

$$\rho^{45^\circ}_{m'm} = \begin{pmatrix} 0.10 & -0.05(-0.01) & -0.03 & 0 & 0 \\ -0.05(0.01) & 0.34 & 0.02(-0.01) & 0.07 & 0 \\ -0.03 & 0.02(0.01) & 0.15 & -0.02(-0.01) & -0.03 \\ 0 & 0.07 & -0.02(0.01) & 0.34 & 0.05(-0.01) \\ 0 & 0 & -0.03 & 0.05(0.01) & 0.08 \end{pmatrix},$$

$$\rho^{90^\circ}_{m'm} = \begin{pmatrix} 0.06 & 0.00(0.00) & -0.05 & 0 & 0 \\ 0.00(0.00) & 0.30 & 0.00(0.00) & 0.13 & 0 \\ -0.05 & 0.00(0.00) & 0.27 & 0.00(0.00) & -0.05 \\ 0 & 0.13 & 0.00(0.00) & 0.30 & 0.00(0.00) \\ 0 & 0 & -0.05 & 0.00(0.00) & 0.06 \end{pmatrix}$$

where the values in parenthesis refer to an imaginary part of the coherence which mostly comes from the γ'_1 contribution. The non-zero off-diagonal terms indicate the coherent interactions present in this system. The uncertainty in determination of these matrix elements is typically better than ±0.04 for the diagonal elements and ±0.01 for the off-diagonal terms based on reproducibility over several independent measurements.

4.3.5 Conclusions

All possible polarization of S($^1D_2$) arising from the dissociation of OCS at 193 nm have been measured using DC sliced imaging. Three peaks corresponding to specific groups of high rotational levels of CO in the vibrational ground state are shown, with the rotationally-resolved rings at the D region ascribed to weak signals associated with excited vibrational states of CO. The observed speed-dependent β parameter and coherent alignment or orientation support that there are two main dissociation processes: the simultaneous two-surface (A' and A'') excitation and the initial single-surface (A') excitation followed by the nonadiabatic crossing to ground state. At 193 nm photodissociation, the nonadiabatic dissociation process is strongly enhanced relative to longer wavelengths. This can be ascribed to the increased probability of the nonadiabatic transition by the faster-speed fragments and greater contribution of excitation to the A' state, compared to those at the lower photolysis energy. Furthermore, the dissociation happens via non-axial recoil dynamics due to the larger deflection associated with a bending motion of parent molecule during dissociation.

The complete density matrix was constructed including the higher order ($K = 3, 4$) contributions for the circularly-polarized dissociation light. It reveals the $\mathbf{v}\|\mathbf{J}$ correlation in the S atom at the C ring and the preferential population of $|m_J| = 1$ at the B ring, respectively. In particular, it was found that the density matrix in the second ring is sensitively affected by the rank 4 terms. This suggests that the higher order contributions should not be overlooked to understand deeply the underlying dissociation dynamics in this system.

Chapter 5

Photodissociation of Acetaldehyde Cation

5.1 Introduction

The photofragmentation processes of cations provide an avenue to investigate a number of important issues in photochemistry. Cations prepared from closed-shell neutrals are open-shell systems, so many low-lying electronic states exist and interactions among them may be readily explored; resonant ionization techniques may be used to prepare specific vibrational states or even particular molecular conformers for photochemical studies, and vibrationally-mediated or mode-specific dissociation may be seen; finally, quantum control experiments often probe fragmentation processes in the product ions, so understanding the neutral and ionic pathways leading to the same final ionic product may be important. Ion imaging represents a powerful means of examining photofragmentation processes in ions. Recently, the photodissociation processes of cations have been extensively explored by velocity map imaging,[110–112] slice imaging,[113,114] and reflectron multimass velocity map imaging[115,116] methods combined with REMPI. The advantage of the imaging technique in these applications is the ability to measure the translational energy and angular distributions easily and with great sensitivity. In addition, the sensitivity of the angular distribution to the symmetry and lifetime of the intermediate state may be important to understand complicated dynamical processes.

The photodissociation of acetaldehyde cations formed by either vacuum-ultraviolet (VUV) or multiphoton ionization has been studied using ionization mass spectrometry,[117,118] photoelectron-photoion coincidence spectrometry,[119,120] and the Fourier transform ion cyclotron resonance (FT-ICR) technique.[121] Bombach *et al.*[119] reported that CH_3CO^+ and HCO^+ are produced either by internal conversion to the ground electronic state ($\tilde{X}\ ^2A'$) of acetaldehyde cations (95 %) or isomerization to ground state oxirane (5 %) near the onset of the $\tilde{A}\ ^2A''$ band. The photoelectron-photoion coincidence studies of Johnson and co-workers[120] showed that CH_4^+ appears together with CH_3CO^+ and HCO^+ above an ionization energy of 13 eV, and the formation of CH_4^+ was interpreted as characteristic of dissociation through the $\tilde{A}\ ^2A''$ band. In the $\tilde{B}\ ^2A'$ band above 14.1 eV, CH_3^+ starts to emerge in addition to CH_3CO^+ and HCO^+, along with a decreasing abundance of CH_4^+. The translational energy distribution of the acetyl ion was cited as evidence that CH_3^+ is produced *via* secondary fragmentation of CH_3CO^+.[120] Fisanick *et al.*[118] and Shin *et al.*[121] proposed that the photodissociation of acetaldehyde cations prepared by multiphoton ionization takes place predominantly by excitation to the $\tilde{B}\ ^2A'$ state. An energy diagram is shown in Fig. 5.1 illustrating the relevant multiphoton ionization and dissociation processes.

In this study, parent ions were generated by 2+1 REMPI through the B $^1A'$ state corresponding to the 3s ← n Rydberg transitions in the range from 354 to 363 nm. The wealth of spectroscopic knowledge for these Rydberg states[122–126] allows identification

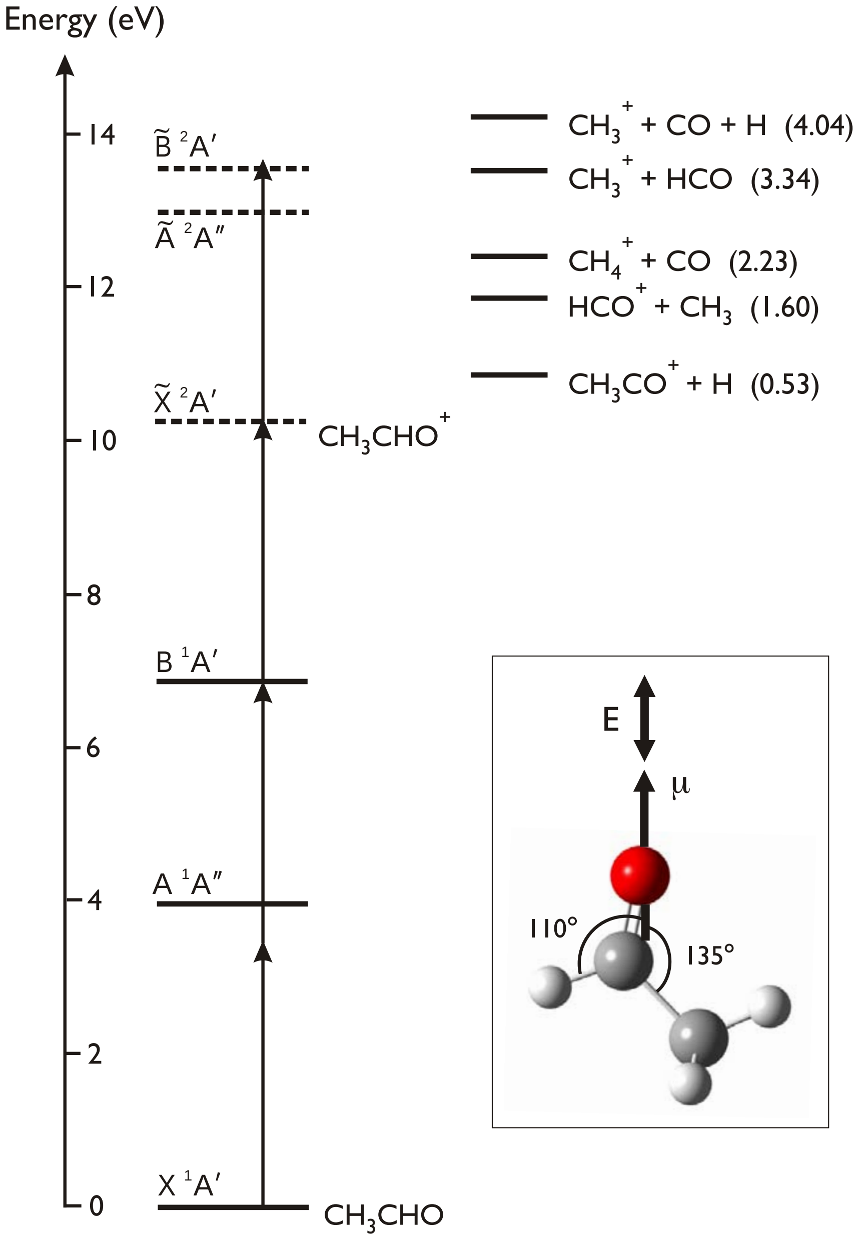

Figure 5.1: Schematic energy diagram for possible dissociation pathways of CH_3CHO^+ and 2+1 resonance-enhanced multiphoton ionization of CH_3CHO. The number in a parentheses indicates the dissociation threshold (eV) from acetaldehyde cation. The inset shows the orientation of the transition dipole moment for $\tilde{B} \leftarrow \tilde{X}$ excitation.

of the vibrational states of parent ions and thus provides a way to elucidate the effect of mode-selective vibrational excitation on cation photodissociation processes. Based on thermodynamic data taken from reference,[127] four dissociation processes, leading to CH_3CO^+, HCO^+, CH_4^+, and CH_3^+ products, are energetically possible with four photons in this wavelength range (Fig. 5.1). Shin *et al.*[121] observed only acetyl ions and formyl ions in this energy region, while Fisanick *et al.*[118] detected several product ions that can be formed with the absorption of up to five photons at the origin band of Rydberg state. A strong power dependence of fragment ion production was also reported in that case.[118]

In the following pages, I present results of an imaging study of the photodissociation of specific vibrational levels of acetaldehyde cations prepared by following $2+1$ REMPI. Particular emphasis is placed on the use of the angular distributions to gain insight into the electronic transitions responsible and to investigate the extent of spatial alignment of the parent ions produced in the REMPI excitation.

5.2 Experiment

The overall experimental apparatus employed in the DC slice imaging approach has been described in Chapter 2 in detail, so only a brief sketch will be given here. A pulsed supersonic molecular beam of acetaldehyde seeded 24% in Ar was expanded into the source chamber and collimated by a skimmer. The beam entered into a velocity mapping electrode assembly optimized for DC slice imaging, and was intersected at a right angle by a laser beam tuned to a two-photon resonant excitation of a

Rydberg state of acetaldehyde. The laser light was generated by frequency doubling the output of a dye laser (Continuum Jaguar, LDS 722 dye) pumped by the 532 nm harmonic of a second Nd:YAG laser (Quanta Ray PRO 290). The polarization of the laser beam was parallel to the detector plane, and the typical output power was $\sim$ 0.3 mJ/pulse in the wavelength range from 354 to 363 nm. The laser light was then focused into the interaction region with a 40 cm focal length lens. In this study, a repeller electrode held at 400 V was used in conjunction with three additional focusing lenses in the velocity-mapping scheme to stretch the photofragment ion cloud along the time-of-flight axis to around 400 ns. The overall flight path from the laser interaction region to the detector was 100 cm. Application of a narrow ($\sim$40 ns) time gate at the detector was then used to sample the central section of the distribution. The resulting ion image was recorded using a CCD camera (Sony XC-ST50, 768 × 494 pixels) in conjunction with the IMACQ Megapixel acquisition program[61] recently developed in our group that enabled a high-resolution real time ion counting with subpixel precision. The newly developed Megapixel analyzing program IMAN also was used to determine the translational energy and angular distributions. In addition, the photoelectron images were obtained with a similar experimental set-up, albeit with a shorter flight path and reversed potentials. For the photoelectron imaging, the main chamber and flight path were shielded with μ-metal sheet to avoid the influence of external magnetic fields.

5.3 Results

The sliced images for all photofragments of acetaldehyde cations following 2+1 REMPI *via* the origin band (55024 cm^{-1}) of the 3s Rydberg transition are presented in Fig. 5.2. As shown in the energy diagram (Fig. 5.1), four products are accessible by one-photon dissociation of the parent cation at this energy (3.41 eV), but only three ionic photofragments were observed: CH_3CO^+, HCO^+, and CH_4^+. The branching ratio of products was estimated roughly from the integrated intensity of each sliced image, which is $CH_3CO^+ : HCO^+ : CH_4^+ = 1.0 : 6.0 : 1.5$. A glance at these images shows that Fig. 5.2 (A), CH_3CO^+, is distinct in several ways: it shows an apparent "hole" in the center as well as a multilobed structure.

The translational energy distributions for the three product ions are plotted in Fig. 5.3. For HCO^+ and CH_4^+, a larger fraction of the available energy is deposited into the internal energy of the photofragments, and the distributions peak near zero. In contrast, the P(E_T) for acetyl ions has a peak at $\sim$ 0.5 eV and a lower yield of slower fragments, corresponding to the "hole" in the experimental image. The average total translational energy is 0.65, 0.17, and 0.09 eV for the CH_3CO^+, HCO^+, and CH_4^+ channels,respectively. These represent 22, 10, and 8 % of the total available energy.

More detailed information on photofragmentation dynamics can be obtained by investigating the angular distribution of the product ions. The angular anisotropy parameters are obtained by fitting the angular distrubutions from the ion images to

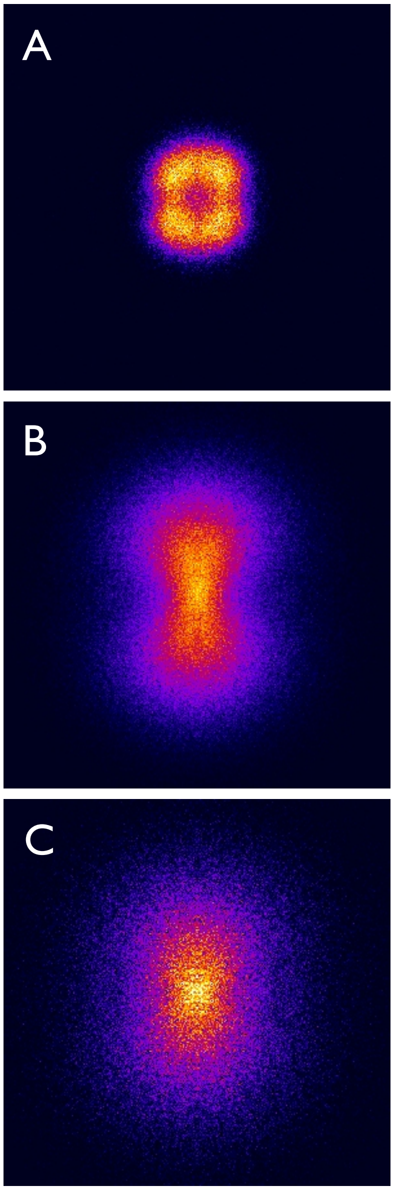

Figure 5.2: Experimental sliced images of three fragments (A: CH_3CO^+, B: HCO^+, and C: CH_4^+) in the photodissociation of acetaldehyde cation prepared by $2+1$ REMPI *via* the origin transition.

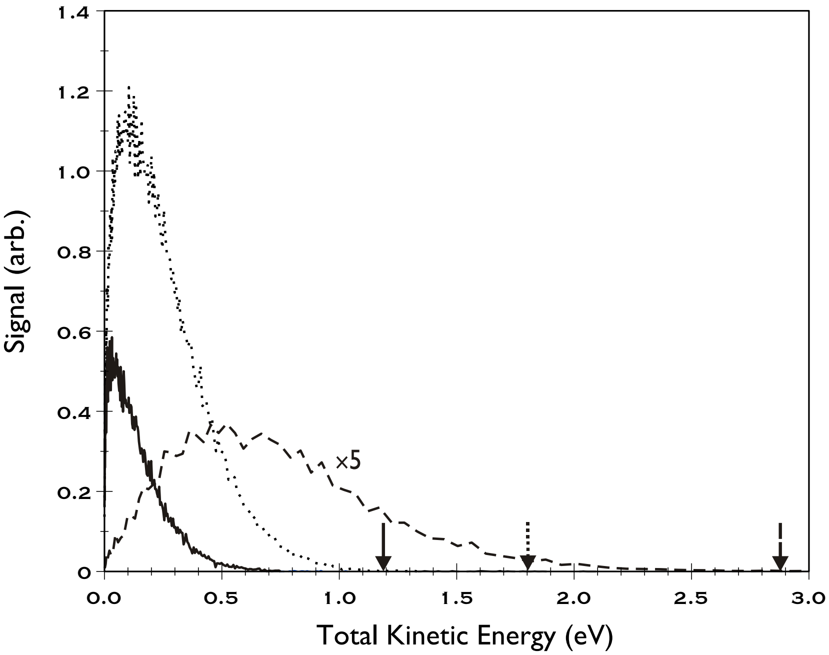

Figure 5.3: Total translational energy distributions of CH_3CO^+ (dashed line), HCO^+ (dotted line) and CH_4^+ (solid line) ions. The arrows show the available energy for each product ion, and the area under each curve relates to the branching fraction of each product.

an even Legendre polynomial expansion including high order terms as follows:

$$I(\theta) \;\propto\; 1 + \beta_2 \cdot P_2(\cos\theta) + \beta_4 \cdot P_4(\cos\theta) + \beta_6 \cdot P_6(\cos\theta) \tag{5.1}$$

where θ is the angle between the laser polarization vector and the recoil velocity vector. The measured anisotropies are listed in Table 5.1 for all fragments. Although the Legendre polynomial terms up to the 8th order may be required for a thorough description of the angular distribution for this four photon process, the 8th order term is ignored because it is likely to make a negligible contribution. Neglecting any angular modulation by multiphoton ionization processes, the angular distribution for one-photon dissociation should be fitted well including only the second order

Table 5.1: Recoil anisotropy parameters for all fragments from the photodissociation of acetaldehyde cation.

Ion	band	β_2	β_4	β_6
CH_3CO^+	origin	0.43	-0.37	0.08
	10^1_0	0.08	-0.30	0.08
	$6^1_0, 7^1_0$	-0.20	0.01	-0.08
HCO^+	origin	0.85	-0.03	-0.02
CH_4^+	origin	0.52	-0.06	0.01

* The uncertainties of reported recoil anisotropy parameters are $\beta_2 \pm 0.1$, $\beta_4 \pm 0.07$, and $\beta_6 \pm 0.01$.

Legendre polynomial term. However, as seen in Fig. 5.4, the angular distribution of acetyl ion required higher order Legendre polynomial terms to get an adequate fit. This striking feature is apparent directly in the experimental image showing the four lobes. It implies that more than one photon process is responsible for the angular distribution.

In order to explore the vibrationally mediated photodissociation dynamics, the parent cation also were prepared by using REMPI via the 10^1_0 (55360 cm^{-1}) and $6^1_0, 7^1_0$ (56195 cm^{-1}) transitions. Three product ions (CH_3CO^+, HCO^+ and CH_4^+) were seen at those wavelengths. It is notable that the angular distribution of the acetyl ion becomes isotropic and tends to be perpendicular as the photon energy increases, as shown in Table 5.1. The photoelectron image and spectrum at the 10^1_0 transition (Fig. 5.5(A)) indicates that parent ions are formed predominantly in the $\nu^+_{10} = 1$ state, which is in good agreement with the result of Kim and Anderson.[126] Fig. 5.5(B) displays the photoelectron image and spectrum obtained by REMPI *via* the $6^1_0, 7^1_0$ transition, where there are many rings assigned to several different vibrational states. That is, the parent ions are not well state-selected at this wavelength.

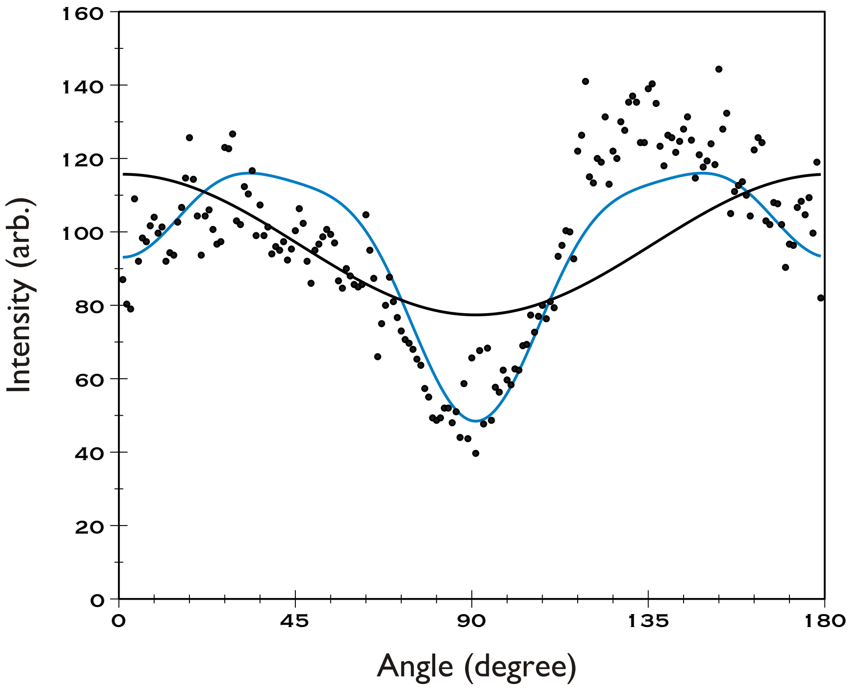

Figure 5.4: Angular distribution of acetyl ion: solid lines correspond to the best fit without (black) and with (blue) higher order Legendre polynomial terms.

5.4 Discussion

Acetaldehyde cations can access two excited states ($\tilde{\mathrm{A}}$, $\tilde{\mathrm{B}}$) by one-photon absorption in this energy range, and the question of which excited state is predominantly involved in dissociation can be answered by examining the angular distributions of photofragments. As mentioned previously, the interesting angular anisotropy of CH_3CO^+ strongly suggests the presence of multiphoton processes. There have been a few studies of the angular distribution in multiphoton processes recently.[110,128–130] Chichinin and co-workers[131] presented the photofragment angular distribution in the dissociative multiphoton ionization of HCl. Li *et al.*[113] studied the angular distribution of CO cation multiphoton dissociation. In general, these multiphoton angular

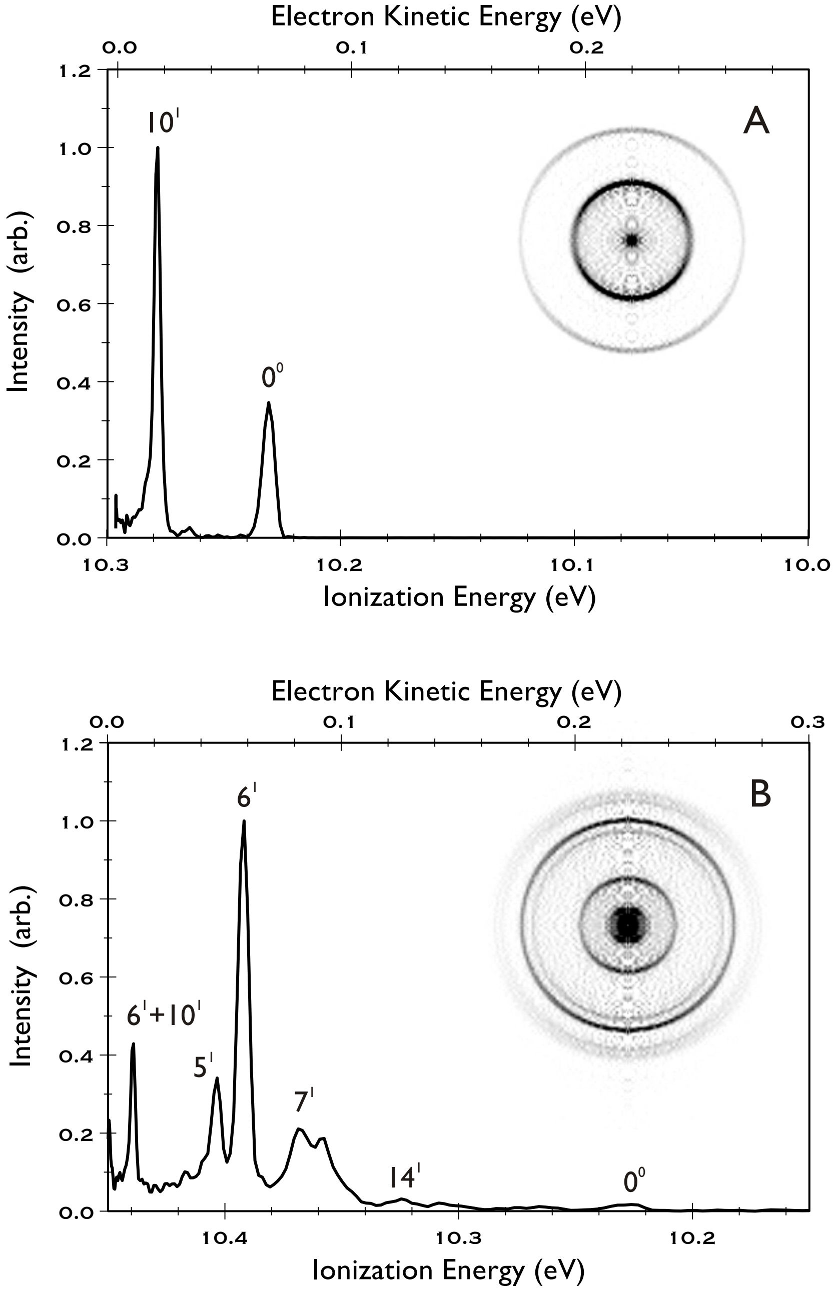

Figure 5.5: Photoelectron spectra and Abel-inverted images for the photodissociation of acetaldehyde cation produced by $2 + 1$ REMPI through the 10^1_0 (A) and $6^1_0, 7^1_0$ (B) bands.

distributions could reflect either neutral multiphoton dissociation with subsequent ionization, or parent ionization followed by dissociation. However, neutral multiphoton dissociation is not likely in this case, which can be confirmed by measuring the photoelectron image. The kinetic energy release of electrons generated by the two processes is quite different: at the origin band, only 3 meV kinetic energy goes to electrons for the resonant ionization/ion dissociation case, while the neutral process with subsequent ionization would be associated with substantial electron kinetic energy. The photoelectron image taken with REMPI through the origin (not shown) displays a strong signal close to zero kinetic energy corresponding to the formation of vibrationless parent ions, consistent with the photoelectron spectroscopy results of Kim *et al.*.[126] This suggests that the product ions result mainly from the dissociation of acetaldehyde cations. The higher order Legendre moments for the acetyl ion image thus must reflect alignment of the ion in the (2+1) ionization step.

Although it is not straightforward to quantitatively measure the molecular alignment induced by multiphoton ionization in this complex polyatomic system, in contrast to the diatomic case,[131] a qualitative interpretation may be achieved for the alignment of acetaldehyde cations by analyzing the angular anisotropy parameters. The β_2 value of HCO^+ showing a parallel recoil anisotropy implies that parent ions are spatially aligned with the C-C bond axis almost parallel to the direction of light polarization (**E**), given that all fragments are formed from the same aligned parent ions. The fact that acetaldehyde cations are pre-aligned suggests that the probability of initial excitation to $\tilde{\mathrm{A}}\ ^2A''$ (pure perpendicular, out of the CCO plane) is not significant due to the orientation of aligned cations with respect to **E**. In other words, it can be speculated that all product ions arise from the initial excitation to the $\tilde{\mathrm{B}}\ ^2A'$ state.

The distinct angular distribution of the acetyl ion not only provides reliable evidence of generating aligned parent ions by multiphoton ionization, but it also indicates that both parallel and perpendicular recoil anisotropies are involved in the H elimination channel. Some of the parallel recoil anisotropy would come from the spatially aligned parent ions, as discussed above. This means that a perpendicular anisotropy might be induced during a dissociation process. According to the discussion of Shin *et al.*,[121] the formation of acetyl and formyl ions is correlated with the dominant initial excitation to the single potential energy surface, the $^2A'$ state. For that case, the angular anisotropy of the acetyl ion would not be much different from that of the formyl ion. To clarify the origin of the two different recoil anisotropies, an *ab initio* TD-DFT calculation was performed by using the B3LYP/6-31+G(d,p) basis set. The transition dipole moment ($\boldsymbol{\mu}$) to $^2A'$ state was found to lie in the CCO molecular plane, and the recoil anisotropy was determined by the angle (α) between the direction of $\boldsymbol{\mu}$ and the recoil direction of a fragment, as described by the well-known $\beta = 2\,P_2(\cos\alpha)$ expression. Assuming a fast dissociation process (ignoring the non-axial recoil dynamics), the angle α can be estimated by considering the asymptotic recoil direction of interest as the corresponding internuclear axis (see the inset in Fig. 1). The estimated values of α formed by the C-H bond in a formyl group and the C-C bond are about 110° ($\beta_{cal.} \approx -0.65$) and 136° ($\beta_{cal.} \approx 0.55$), respectively. This implies that the angular anisotropy of the acetyl ion in dissociation is more perpendicular relative to that of the formyl ion even though both the H elimination and the C-C cleavage happen through the same initial excitation. The reason for having a lower estimated value than the experimental β for HCO^+ (0.85) could be that the angular modulation by spatially aligned parent ions was not considered. The angular distribution for CH_4^+, with the relatively lower β_2 value, cannot be easily rationalized with a simple picture owing to either the H intramolecular rearrangement (hydrogen scrambling) or the possible partial contribution from a roaming mechanism.

The angular distribution of the acetyl ions varies with a well-characterized excitation in a specific vibrational mode as indicated in Table 1. At the 10_0^1 transition, its vibrational motions (CH_3 rocking and CCO bending) could interfere with the appearance of the alignment of the acetaldehyde cation. However, the aligned parent ions are still seen, as evidenced by the large value of β_4. In contrast, the angular distribution at the $6_0^1, 7_0^1$ band has a small perpendicular anisotropy with a β_4 parameter near zero. Vibrational motions in several modes probably wash out the molecular alignment effect, resulting in the formation of parent ions with an angular distribution that is nearly isotropic. Therefore, the overall angular distribution may be mainly attributed to the one-photon dissociation of parent cations, in agreement with the above explanation of a perpendicular component for the H elimination channel.

The results of the translational energy distribution measurements are consistent with those reported by Johnson and co-workers[120] at lower resolution. These features of the translational energy distributions for HCO^+ and CH_4^+ (Fig. 3) are often interpreted as a signature of barrierless statistical dissociation from the ground state.[132] The small partitioning (8∼10 %) into product translational energy is not consistent with the direct dissociation along a repulsive excited state or predissociating state.

Therefore, it can be proposed that these products arise from the ground electronic state following internal conversion as argued by Johnson *et al.*. For the formation of CH_4^+, one might suspect the dissociation to occur over a barrier. The observed $P(E_T)$ of CH_4^+ implies that the barrier must be very small, unlike the photodissociation of neutral acetaldehyde. An alternative explanation to account for the low translational energy and high internal energy in this channel is the possibility of a "roaming" mechanism[133] involving methyl radicals, co-fragments of formyl ions. In this picture, methyl radicals are nearly lost via barrierless dissociation but return to effect intramolecular proton abstraction forming highly excited CH_4^+. In an analogous recent study of acetaldehyde photodissociation, the role of a roaming mechanism in the CH_3 + HCO channel was proposed to form the final products, CH_4 and CO.[134]

The peak of $P(E_T)$ for CH_3CO^+ is away from zero energy. This could be due to a secondary dissociation pathway involving the fragmentation of highly excited CH_3CO^+. However, this explanation can be ruled out because there is no evidence of opening of the secondary channel (i.e., no CH_3^+). Another possibility is the presence of an exit barrier for the H elimination channel. To date, the measured appearance energy (AE) of the acetyl ions ranges from 10.67 to 10.90 eV,[135–137] which represents either a nearly zero or very small barrier. Some theoretical studies[138,139] reported that a small exit barrier (∼0.1 eV) exists for this channel. Johnson and co-workers[120] found that the translational energy partitioning of the total available energy, $\langle E_{trans} \rangle / \langle E_{avail} \rangle$ is ∼22 and 11 % for the acetyl and formyl ions, respectively, which is consistent with results reported in this work. They found those values were in accord with statistical predictions and concluded that those product ions occurs *via* internal conversion followed by dissociation on the ground state. The larger translational energy release for the H atom loss channel is largely owing to the absence of rotational degrees of freedom for that fragment.

5.5 Conclusion

The translational energy and angular distributions of fragments in the photodissociation of acetaldehyde cations are presented here. The peculiar angular distribution of acetyl ions having a large value of β_4 anisotropy parameter supports the suggestion that parent ions produced by REMPI *via* the origin band are predominantly aligned parallel to the polarization direction of light in the multiphoton ionization process. The spatially-aligned parent cation is mostly excited to the $\tilde{\mathrm{B}}$ state and dissociates. However, the spatial alignment effect is diminished when dissociation occurs through parent ions populated in many vibrational excited states.

References

[1] H. Okabe, *Photochemistry of Small Molecules*, Wiley, New York, 1978.

[2] J. P. Simons, *J. Phys. Chem.*, 1987, **91**, 5378.

[3] R. J. Van Brunt and R. N. Zare, *J. Chem. Phys.*, 1968, **48**, 4304.

[4] R. N. Zare and D. R. Herschbach, *Proc. IEEE*, 1963, **51**, 173.

[5] J. Solomon, *J. Chem. Phys.*, 1967, **47**, 889.

[6] R. N. Zare, *Mol. Photochem.*, 1972, **4**, 1.

[7] L. D. A. Siebbeles, M. Glass-Maujean, O. S. Vasyutinskii, J. A. Beswick, and O. Roncero, *J. Chem.Phys.*, 1994, **100**, 3610.

[8] C. Jonah, *J. Phys. Chem.*, 1971, **55**, 1915.

[9] S. Yang and R. Bersohn, *J. Phys. Chem.*, 1974, **61**, 4400.

[10] P. L. Houston, *J. Phys. Chem.*, 1987, **91**, 5388.

[11] R. J. Gordon and G. E. Hall, *Adv. Chem. Phys.*, 1996, **96**, 1.

[12] A. V. Demyanenko, V. Dribinski, H. Reisler, H. Meyer, and C. X. W. Qian, *J. Chem. Phys.*, 1999, **111**, 7383.

[13] V. V. Kuznetsov and O. S. Vasyutinskii, *J. Chem. Phys.*, 2005, **123**, 34307.

[14] E. R. Wouters, M. Ahmed, D. S. Peterka, A. S. Bracker, A. G. Suits, and O. S. Vasyutinskii in *Imaging in Chemical Dynamics*, ed. R. E. Continetti and A. G. Suits; American Chemical Society, Washington, 2000; p. 238.

[15] Y. Mo, H. Katayanagi, M. C. Heaven, and T. Suzuki, *Phys. Rev. Lett.*, 1996, **77**, 830.

[16] A. T. J. B. Eppink, D. H. Parker, M. H. M. Janssen, B. Buijsse, and W. J. van der Zande, *J. Chem. Phys.*, 1998, **108**, 1305.

[17] A. S. Bracker, E. R. Wouters, A. G. Suits, and O. S. Vasyutinskii, *J. Chem. Phys.*, 1999, **110**, 6749.

[18] Y. Wang, H. P. Loock, J. Cao, and C. X. W. Qian, *J. Chem. Phys.*, 1995, **102**, 808.

[19] T. P. Rakitzis, S. A. Kandel, and R. N. Zare, *J. Chem. Phys.*, 1998, **108**, 8291.

[20] S. W. North, X. S. Zheng, R. Fei, and G. E. Hall, *J. Chem. Phys.*, 1996, **104**, 2129.

[21] M. L. Costen, S. W. North, and G. E. Hall, *J. Chem. Phys.*, 1999, **111**, 6735.

[22] A. S. Bracker, *An investigation of polarized atomic photofragments using the ion imaging technique*, Ph D thesis, University of California, Berkeley, 1997.

[23] R. N. Dixon, *J. Chem. Phys.*, 1986, **85**, 1866.

[24] G. E. Hall, N. Sivakumar, D. Chawla, P. L. Houston, and I. Burak, *J. Chem. Phys.*, 1988, **88**, 3682.

[25] B. V. Picheyev, A. G. Smolin, and O. S. Vasyutinskii, *J. Phys. Chem.*, 1997, **101**, 7614.

[26] M. Brouard, P. O'Keeffe, D. M. Joseph, and D. Minayev, *Phys. Rev. Lett.*, 2001, **86**, 2249.

[27] T. P. Rakitzis, S. A. Kandel, A. J. Alexander, Z. H. Kim, and R. N. Zare, *Science*, 1998, **281**, 1346.

[28] A. G. Suits, R. L. Miller, L. S. Bontuyan, and P. L. Houston, *J. Chem. Soc., Faraday Trans. 2*, 1993, **89**, 1443.

[29] T. Suzuki, H. Katayanagi, Y. Mo, and K. Tonokura, *Chem. Phys. Lett.*, 1996, **256**, 90.

[30] V. K. Nestorov and J. I. Cline, *J. Chem. Phys.*, 1999, **111**, 5287.

[31] M. Ahmed, D. S. Peterka, A. S. Bracker, O. S. Vasyutinskii, and A. G. Suits, *J. Chem. Phys.*, 1999, **110**, 4115.

[32] M. Ahmed, E. R. Wouters, D. S. Peterka, O. S. Vasyutinskii, and A. G. Suits, *Faraday Discuss.*, 1999, **113**, 425.

[33] T. P. Rakitzis, P. C. Samartzis, and T. N. Kitsopoulos, *J. Chem. Phys.*, 1999, **111**, 10415.

[34] T. M. Teule, G. C. Groenenboom, D. W. Neyer, D. W. Chandler, and M. H. M. Janssen, *Chem. Phys. Lett.*, 2000, **320**, 177.

[35] T. P. Rakitzis, R. L. Toomes, L. Tsigaridas, M. Coriou, D. Chestakov, A. T. J. B. Eppink, D. H. Parker, and T. N. Kitsopoulos, *Chem. Phys. Lett.*, 2002, **364**, 115.

[36] T. P. Rakitzis and T. N. Kitsopoulos, *J. Chem. Phys.*, 2002, **116**, 9228.

[37] E. R. Wouters, M. Beckert, L. J. Russell, K. N. Rosser, A. J. Orr-Ewing, M. N. R. Ashfold, and O. S. Vasyutinskii, *J. Chem. Phys.*, 2002, **117**, 2087.

[38] T. P. Rakitzis, P. C. Samartzis, R. L. Toomes, T. N. Kitsopoulos, A. Brown, G. G. Balint-Kurti, O. S. Vasyntinskii, and J. A. Beswick, *Science*, 2003, **300**, 1936.

[39] M. Brouard, A. P. Clark, C. Vallance, and O. S. Vasyutinskii, *J. Chem. Phys.*, 2003, **119**, 771.

[40] M. J. Bass, M. Brouard, A. P. Clark, C. Vallance, and B. Martinez-Haya, *Phys. Chem. Chem. Phys.*, 2003, **5**, 856.

[41] T. P. Rakitzis, P. C. Samartzis, R. L. Toomes, and T. N. Kitsopoulos, *J. Chem. Phys.*, 2004, **121**, 7222.

[42] M. Brouard, R. Cireasa, A. P. Clark, T. J. Preston, C. Vallance, G. C. Groenenboom, and O. S. Vasyutinskii, *J. Phys. Chem. A*, 2004, **108**, 7965.

[43] D. Townsend, S. K. Lee, and A. G. Suits, *Chem. Phys.*, 2004, **301**, 197.

[44] S. K. Lee, D. Townsend, O. S. Vasyutinskii, and A. G. Suits, *Phys. Chem. Chem. Phys.*, 2005, **7**, 1650.

[45] A. J. van den Brom, T. P. Rakitzis, and M. H. M. Janssen, *J. Chem. Phys.*, 2005, **123**, 164313–1.

[46] A. G. Smolin, O. S. Vasyutinskii, O. P. J. Vieuxmaire, M. N. R. Ashfold, G. G. Balint-Kurti, and O.-E. A. J., *J. Chem. Phys.*, 2006, **124**, 094305.

[47] C. R. Gebhardt, T. P. Rakitzis, P. C. Samartzis, V. Ladopoulos, and T. N. Kitsopoulos, *Rev. Sci. Instr.*, 2001, **72**, 3848.

[48] D. Townsend, M. P. Minitti, and A. G. Suits, *Rev. Sci. Instrum.*, 2003, **74**, 2530.

[49] J. J. Lin, J. Zhou, W. Shiu, and K. Liu, *Rev. Sci. Instr.*, 2003, **74**, 2495.

[50] S. M. Dylewski, J. D. Geiser, and P. L. Houston, *J. Chem. Phys.*, 2001, **115**, 7460.

[51] T. P. Rakitzis, P. C. Samartzis, and T. N. Kitsopoulos, *Phys. Rev. Lettt.*, 2001, **87**, 123001–1.

[52] A. J. Alexander and R. N. Zare, *Acc. Chem. Res.*, 2000, **33**, 199.

[53] Z. H. Kim, A. J. Alexander, and R. N. Zare, *J. Phys. Chem. A*, 1999, **103**, 10144.

[54] D. Townsend, W. Li, S. K. Lee, R. L. Gross, and A. G. Suits, *J. Phys. Chem. A*, 2005, **109**, 8661.

[55] A. G. Smolin, O. S. Vasyutinskii, E. R. Wouters, and A. G. Suits, *J. Chem. Phys.*, 2004, **121**, 6759.

[56] D. W. Chandler and P. L. Houston, *J. Chem. Phys.*, 1987, **87**(2), 1445–1447.

[57] A. T. J. B. Eppink and D. H. Parker, *Rev. Sci. Instrum.*, 1997, **68**(9), 3477–3484.

[58] L. McDonnell and A. J. R. Heck, *J. Mass. Spectrom.*, 1998, **33**, 415.

[59] A. S. Bracker, E. R. Wouters, A. G. Suits, Y. T. Lee, and O. S. Vasyutinskii, *Phys. Rev. Lett.*, 1998, **80**, 1626.

[60] K. Tonokura and K. Suzuki, *Chem. Phys. Lett*, 1994, **224**(1-2), 1–6.

[61] W. Li, S. D. Chambreau, S. A. Lahankar, and A. G. Suits, *Rev. Sci. instrum.*, 2005, **76**, 063106.

[62] A. V. Komissarov, M. P. Minitti, A. G. Suits, and G. E. Hall, *J. Chem. Phys.*, 2006, **124**, 014303.

[63] R. N. Zare, *Angular Momentum*, Wiley, New York, 1988.

[64] G. G. Balint-Kurti, A. J. Orr-Ewing, J. A. Beswick, A. Brown, and O. S. Vasyutinskii, *Phys. Chem. Chem. Phys.*, 2002, **116**, 10760.

[65] K. Blum, *Density Matrix Theory and Application*, Plenum, New York, 1996.

[66] A. G. Suits and O. S. Vasyutinskii, *Chem. Rev.*, In preparation.

[67] A. C. Kummel, G. O. Sitz, and R. N. Zare, *J. Chem. Phys.*, 1986, **85**, 6874.

[68] A. C. Kummel, G. O. Sitz, and R. N. Zare, *J. Chem. Phys.*, 1987, **88**, 6707.

[69] Y. Mo and T. Suzuki, *J. Chem. Phys.*, 1998, **109**, 4691.

[70] P. Felder, A. J. Wannenmacher, I. Wiedmer, and J. R. Huber, *J. Phys. Chem.*, 1992, **96**, 4470.

[71] H. L. Kim, S. Satyapal, P. Brewer, and R. Bersohn, *J. Chem. Phys.*, 1989, **91**, 1047.

[72] F. Qi, O. Sorkhabi, and A. G. Suits, *J. Chem. Phys.*, 2000, **112**, 10707.

[73] F. Qi, O. Sorkhabi, A. G. Suits, S.-H. Chien, and W.-K. Li, *J. Am. Chem. Soc.*, 2001, **123**, 148.

[74] I. Tokue, A. Hiraya, and K. Shobatake, *J. Chem. Phys.*, 1989, **91**, 2808.

[75] W. H. Press, S. A. Teukolsky, W. T. Vetterling, and B. P. Flannery, *Numerical Recipes in Fortran*, Cambridge University Press, Cambridge, 1992.

[76] M. Carnell and S. D. Peyerimhoff, *Chem. Phys. Lett.*, 1993, **212**, 654.

[77] L. B. Clark and W. T. Simpson, *J. Chem. Phys.*, 1965, **43**, 3666.

[78] D. Babikov, B. K. Kendrick, R. B. Walker, R. Schinke, and R. T. Pack, *Chem. Phys. Lett.*, 2003, **372**, 686.

[79] Y. Q. Gao and R. A. Marcus, *Science*, 2001, **293**, 259.

[80] L. T. Molina and M. J. Molina, *J. Geophys. Res.*, 1986, **91**, 14501.

[81] J. Malicet, D. Daumont, J. Charbonnier, C. Parisse, A. Chakir, and J. Brion, *J. Atmos. Chem.*, 1995, **21**, 263.

[82] J. D. Geiser, S. M. Dylewski, J. A. Mueller, R. J. Wilson, R. Toumi, and P. L. Houston, *J. Chem. Phys.*, 2000, **112**, 1279.

[83] M. A. Thelen, T. Gejo, J. A. Harrison, and J. R. Huber, *J. Chem. Phys.*, 1995, **103**, 7946.

[84] C. E. Fairchild, E. J. Stone, and G. M. Lawrence, *J. Chem. Phys.*, 1978, **69**, 3632.

[85] R. K. Sparks, L. R. Carlson, K. Shobatake, M. L. Kowalczyk, and Y. T. Lee, *J. Chem. Phys.*, 1980, **72**, 1401.

[86] J. J. Valentini, D. P. Gerrity, J.-C. N. Phillips, and K. D. Tabor, *J. Chem. Phys.*, 1987, **86**, 6745.

[87] Z.-W. Qu, H. Zhu, and R. Schinke, *Chem. Phys. Lett.*, 2003, **377**, 359.

[88] R. J. Wilson, J. A. Mueller, and P. L. Houston, *J. Phys. Chem. A*, 1997, **101**, 7593.

[89] N. Taniguchi, K. Takahashi, Y. Matsumi, S. M. Dylewski, J. D. Geiser, and P. L. Houston, *J. Chem. Phys.*, 1999, **111**, 6350.

[90] G. Hancock, P. J. Pearson, G. A. D. Ritchie, and D. F. Tibbetts, *Phys. Chem. Chem. Phys.*, 2003, **5**, 5386.

[91] G. Hancock, P. J. Pearson, G. A. D. Ritchie, and D. F. Tibbetts, *Chem. Phys. Lett.*, 2004, **393**, 425.

[92] K. O. Korovin, B. V. Picheyev, O. S. Vasyutinskii, H. Valipour, and D. Zimmermann, *J. Chem. Phys.*, 2000, **112**, 2059.

[93] H. Naramura, *Nonadiabatic Transitions: Beyond Born-Oppenheimer, Dynamics of Molecules and Chemical Reactions*, Marcel Dekker, New York, 1996.

[94] E. Baloïtcha and G. G. Balint-Kurti, *J. Chem. Phys.*, 2005, **123**, 014306.

[95] W. Denzer, S. J. Horrocks, P. J. Pearson, and G. A. D. Ritchie, *Phys. Chem. Chem. Phys.*, 2006, **8**, 1954.

[96] S. J. Horrocks, P. J. Pearson, and G. A. D. Ritchie, *J. Phys. Chem.*, 2006, **125**, 133313.

[97] M. Brouard, R. Cireasa, A. P. Clark, G. C. Groenenboom, G. Hancock, S. J. Horrocks, F. Quadrini, G. A. D. Ritchie, and C. Vallance, *J. Chem. Phys.*, 2006, **125**, 133308.

[98] J. C. Polanyi and P. A. Young, *J. Chem. Phys.*, 1990, **93**, 3673.

[99] W. Kedzierski, J. Borbely, and J. W. McConkey, *J. Phys. B: At. mol. Opt. Phys.*, 2001, **34**, 4027.

[100] T. Suzuki, H. Katayanagi, S. Nanbu, and M. Aoyagi, *J. Chem. Phys.*, 1998, **109**, 5778.

[101] H. Katayanagi and T. Suzuki, *Chem. Phys. Lett.*, 2002, **360**, 104.

[102] A. Sugita, M. Mashino, M. Kawasaki, Y. Matsumi, R. Bersohn, G. Trott-Kriegeskorte, and K. H. Gericke, *J. Chem. Phys.*, 2000, **112**, 7095.

[103] A. M. Rijs, E. H. G. Backus, C. A. de Lange, M. H. M. Janssen, N. P. C. Westwood, K. Wang, and V. McKoy, *J. Chem. Phys.*, 2002, **116**, 2776.

[104] A. J. van den Brom, T. P. Rakitzis, J. van Heyst, T. N. Kitsopoulos, and M. H. M. Janssen, *J. Chem. Phys.*, 2002, **117**, 4255.

[105] C. E. Strauss, G. C. McBane, P. L. Houston, I. Burak, and J. W. Hepburn, *J. Chem. Phys.*, 1989, **90**, 5364.

[106] S. M. Wu, X. Yang, and D. H. Parker, *Mol. Phys.*, 2005, **103**, 1797.

[107] M. H. Kim, W. Li, S. K. Lee, and A. G. Suits, *Can. J. Chem.*, 2004, **82**, 880.

[108] T. P. Rakitzis, A. J. van den Brom, and M. H. M. Janssen, *Science*, 2004, **303**, 1852.

[109] N. Sivakumar, G. E. Hall, P. L. Houston, J. W. Hepburn, and I. Burak, *J. Chem. Phys.*, 1988, **88**, 3692.

[110] O. P. J. Vieuxmaire, N. H. Nahler, J. R. Jones, R. N. Dixon, and M. N. R. Ashfold, *Mol. Phys.*, 2005, **103**, 2437.

[111] M. Beckert, S. J. Greaves, and M. N. R. Ashfold, *Phys. Chem. Chem. Phys.*, 2003, **5**, 308.

[112] F. Aguirre and S. T. Pratt, *J. Chem. Phys.*, 2003, **118**, 6318.

[113] W. Li, S. A. Lahankar, C. Huang, P. S. Shternin, O. S. Vasyutinskii, and A. G. Suits, *Phys. Chem. Chem. Phys.*, 2006, **8**, 2950.

[114] C. Chang, C. Y. Luo, and K. Liu, *J. Phys. Chem. A*, 2005, **109**, 1022.

[115] M. H. Kim, B. D. Leskiw, and A. G. Suits, *J. Phys. Chem. A*, 2005, **109**, 7839.

[116] M. H. Kim, L. Shen, and A. G. Suits, *Phys. Chem. Chem. Phys.*, 2006, **8**, 2933.

[117] H. W. Jochims, W. Lohr, and H. Baumgärtel, *J. Chem. Phys.*, 2003, **118**, 6318.

[118] G. J. Fisanick, T. S. Eichelberger, B. A. Heath, and M. B. Robin, *Chem. Phys. Lett.*, 1978, **54**, 594.

[119] R. Bombach, J. P. Stadelmann, and J. Vogt, *Chem. Phys.*, 1981, **60**, 293.

[120] K. Johnson, I. Powis, and C. J. Danby, *Chem. Phys.*, 1982, **70**, 329.

[121] S. K. Shin, B. Kim, J. G. Haldeman, and S. J. Han, *J. Chem. Phys.*, 1996, **100**, 8280.

[122] M. A. Buntine, G. F. Metha, D. C. McGilvery, and R. J. S. Morrison, *J. Mol. Spectrosc.*, 1994, **165**, 12.

[123] N. C. Shand, C. N. Ning, and J. Pfab, *Chem. Phys. Lett.*, 1995, **247**, 32.

[124] H. Meyer, *Chem. Phys. Lett.*, 1996, **262**, 603.

[125] Y. Kim, J. Fleniken, and J. Meyer, *Chem. Phys.*, 1998, **109**, 3401.

[126] H. T. Kim and S. L. Anderson, *J. Chem. Phys.*, 2001, **114**, 3018.

[127] NIST standard reference database `http://webbook.nist.gov/chemistry/`.

[128] B. R. Cosofret, H. M. Lambert, and P. L. Houston, *J. Chem. Phys.*, 2002, **117**, 8787.

[129] S. Manzhos, C. Romanescu, H.-P. Loock, and J. G. Underwood, *J. Chem. Phys.*, 2004, **121**, 11802.

[130] R. N. Dixon, *J. Chem. Phys.*, 2005, **122**, 194302.

[131] A. I. Chichinin, P. S. Shternin, N. Gödecke, S. Kauczok, C. Maul, O. S. Vasyutinskii, and K. H. Gericke, *J. Chem. Phys.*, 2006, **125**, 034310.

[132] D. A. Blank, S. W. North, D. Stranges, and A. G. Suits, *J. Chem. Phys.*, 1997, **106**, 539.

[133] D. Townsend, S. A. Lahankar, S. K. Lee, S. D. Chambreau, A. G. Suits, X. Zhang, J. Rheinecker, L. B. Harding, and J. M. Bowman, *Science*, 2004, **306**, 1158.

[134] P. L. Houston and S. H. Kable, *Proc. Natl. Acad. Sci*, 2006, **103**, 16079.

[135] R. Krässig, D. Reinke, H. Baumgärtel, and B. Bunsenges, *Phys. Chem.*, 1974, **78**, 425.

[136] R. H. Staley, R. D. Wieting, and H. Beauchamp, *J. Am. Chem. Soc.*, 1977, **99**, 5964.

[137] J. C. Traeger, R. G. McLoughlin, and A. J. C. Nicholson, *J. Am. Chem. Soc.*, 1982, **104**, 5318.

[138] S. B. J. and L. Radom, *Int. J. Mass Spectrom. Ion Processes*, 1990, **101**, 209.

[139] W. Bertrand and G. Bouchoux, *Rapid Commun. Mass Spectrom.*, 1998, **12**, 1697.